

Numerical modelling of atmospheric flows over complex sites with special regard to the forest canopy

Dissertation

der Mathematisch-Naturwissenschaftlichen Fakultät
der Eberhard Karls Universität Tübingen
zur Erlangung des Grades eines
Doktors der Naturwissenschaften
(Dr. rer. nat.)

vorgelegt von
Asmae El Bahlouli-Öztürk
aus Rabat Marokko

Tübingen
2021

Gedruckt mit Genehmigung der Mathematisch-Naturwissenschaftlichen Fakultät
der Eberhard Karls Universität Tübingen.

Tag der mündlichen Qualifikation: 30.05.2022

Dekan: Prof. Dr. Thilo Stehle

1. Berichterstatter: Prof. Dr. Jens Bange

2. Berichterstatter: Prof. Dr.-Ing. Frank Rückert

Abstract

The present thesis describes the work carried out using the OpenFOAM solver with a Reynolds-Averaged Navier Stokes (RANS) approach to investigate the wind flow at complex sites for wind-energy exploitation. Toward this objective, several physical effects such as buoyancy, forest canopies, Coriolis forces, stratification as well as humidity have been implemented in the model to improve wind-field predictions.

First, the wind flow in an urban environment and, more precisely, a university campus is investigated. A stationary logarithmic profile for the wind velocity at the inlet is prescribed. Despite the assumption of a flat terrain, which is a drastic simplification of the real ground, the study shows how a simple canopy model improves the prediction of the flow at the site. The simulation is validated with long term measurements from a network of six stations.

Secondly, results from a rural case in the Swabian Alb in Southern Germany, characterized by a forested escarpment, are presented. The model is adapted to atmospheric boundary layer (ABL) flows and a computational domain with a ground conforming to the site orography is built. To get more realistic boundary conditions and to avoid the assumption of logarithmic profiles, the solver is coupled with a numerical weather prediction (NWP) model. The coupling is performed using a one-way approach, i.e. the coarse weather model provides input to the OpenFOAM solver through the lateral boundary conditions of the computational domain. Simulations with and without forest are compared. The results with a canopy model clearly show at the lower levels a flow deceleration and an increase in turbulence intensities by a factor of four, when compared to results without forest. The study reveals again the important impact of the forest on the wind-field, especially at turbine-relevant heights.

Finally, the transient approach (unsteady RANS) is tested by using time-dependent boundary conditions. The accuracy of the coupling is evaluated by validating the simulation results against measurements from a tall meteorological tower as well as an unmanned aircraft system. Adopting a transient approach leads to an excellent agreement of the model. The thesis shows that an unsteady RANS based solver, which accounts for first-order relevant physics, can be valuable for a wind resource assessment at low computational cost compared to detached-eddy (DES) or large-eddy (LES) simulations.

Zusammenfassung

Die vorliegende Arbeit beschäftigt sich mit der Untersuchung der Windverhältnisse mit dem OpenFOAM-Löser mit dem Ziel der Gewinnung von Windenergie an komplexen Standorten. Es wurden dafür verschiedene physikalische Einflussgrößen wie Auftriebseffekte, Wald, Corioliskraft, Stabilität sowie Luftfeuchtigkeit im Modell implementiert, um die Windfeldvorhersagen zu verbessern.

Zuerst wurde die Windströmung an einem urbanen Standort (Campus der Universität Tübingen) untersucht. Eine stationäre Simulation mit einem logarithmischen Windprofil am Einlass wurde durchgeführt. Die realen Bodenverhältnisse wurden durch ein flaches Bodenmodell abgebildet, trotzdem zeigt die Studie dank eines Waldmodells eine Verbesserung der Vorhersagen der Windgeschwindigkeiten. Die Simulationen wurden mit Langzeitmessungen aus einem Netzwerk von sechs Stationen validiert.

Anschließend werden die Ergebnisse von einer ländlichen Fallstudie an der Schwäbischen Alb in Süddeutschland vorgestellt, die durch eine bewaldete Geländekante charakterisiert ist. Das Modell ist an Strömungen der atmosphärischen Grenzschicht angepasst und es wird eine Berechnungsdomäne mit einem digitalen Geländemodell erstellt, die der Orographie des Standorts entspricht. Um eine realistischere Randbedingung zu erhalten und die Verwendung eines logarithmischen Profils zu vermeiden, wird der Löser mit einem Wettervorhersagemodell gekoppelt. Die Kopplung zwischen dem makroskaligen Wettermodell und dem mikroskaligen Modell wurde entlang der Ränder durchgeführt. Simulationen mit und ohne Wald wurden verglichen. Die Ergebnisse mit einem Waldmodell zeigen auf niedrigen Höhen eine Reduzierung der Strömung und eine gleichzeitige vierfache Erhöhung der turbulenten kinetischen Energie im Vergleich zu den Ergebnissen ohne Wald. Auch diese Studie zeigt den wichtigen Einfluss des Waldes auf das Windfeld, insbesondere auf turbinenrelevanten Höhen.

Schließlich wurde der transiente Ansatz unter Verwendung zeitabhängiger Randbedingungen getestet. Die Genauigkeit der Kopplung wurde überprüft, indem unsere Simulationsergebnisse anhand von Messungen eines meteorologischen Messturms sowie eines unbemannten Flugzeugsystems validiert wurden. Dieser transiente Ansatz führte zu einer hervorragenden Übereinstimmung des Modells mit den Messungen. Die Arbeit zeigt, dass ein URANS-basierter Solver, welcher die Physik erster Ordnung berücksichtigt, für die Bewertung der Windressourcen bei geringem Rechenaufwand im Vergleich zu Detached-Eddy Simulation (DES) oder Large-Eddy Simulation (LES) Methoden wertvoll sein kann.

Acknowledgments

Several people played a role in this work and I am very grateful for their help and support along the way.

First and foremost, I'm extremely grateful to my two supervisors, Prof. Hermann Knaus and Prof. Jens Bange, for their continuous support and the opportunity to take on this challenge. Thank you again to Jens Bange for suggesting me and supporting me over the two positions in the first place, and to Hermann Knaus for believing in me and making it happen. I thank you not only for the professional environment but also the enjoyable time outside of work. My sincere thanks goes to Frank Rückert, who has contributed to the review of this thesis. The completion of my thesis would not have been possible without your technical and scientific guidance but also your encouragement and patience.

I would also like to extend my sincere thanks to my colleagues from the Hochschule Esslingen and the Umphy-team from the University of Tübingen: Alexander R., Andreas R., Andreas P., Dave, Francesca, John, Hossein, Martin, Moritz, Norman, Torsten and Uwe. I enjoyed your professional help as well as the good times we had during my stay. I would like to recognize the effort and collaboration of Daniel from the Karlsruhe Institute of Technology (KIT) within the WINSENT project. Extensive measurements performed during the IQF project would not have been possible without the support of Jürgen Bunzel from the Technical Building Management (TBA) of the University of Tübingen. I would also like to thank the students that have been involved in my research in the last years: Moritz, Patrick and Saskia. A big thanks to everyone who indirectly worked with me in the last years: Ashvinkumar, Alexander S. and Marie.

This research work was supported by the WINSENT project financed by the Federal Ministry for Economic Affairs and Energy of Baden Württemberg and the IQF project financed by the Ministry of Science, Research and the Arts of Baden Württemberg. I also acknowledge the state of Baden Württemberg for providing computational resources through bwHPC.

Et comme on dit, le meilleur pour la fin, je souhaite remercier ma famille qui m'a toujours soutenue et crue en mes projets pas vraiment projetés... Un gros Big up à vous.

Contents

Nomenclature

Abbreviations

ABL	Atmospheric Boundary Layer
AGL	above ground level
CFD	Computational Fluid Dynamics
COSMO	COntortium for Small-scale MOdelling
DES	Detached Eddy Simulation
DWD	Deutscher Wetterdienst
LAI	Leaf Area Index
LAD	Leaf Area Density
LES	Large Eddy Simulation
MASC	Multipurpose Airborne Sensor Carrier
(U) RANS	(Unsteady) Reynolds-Averaged Navier-Stokes equation
UAS	Unmanned Aircraft System
WRA	Wind Resource Assessment
WRF	Weather Research and Forecasting model
WT	Wind Turbine

Symbols

Ri_B	Bulk Richardson number	$[-]$
x, y, z	Cartesian coordinates	m
ρ	Density	kg/m^3
D	Diffusion coefficient	m^2/s
C_d	Drag coefficient	$[-]$
H	Forest height	m
g	Gravitation acceleration	m/s^2
α	Inclination angle	$^\circ$
θ	Potential temperature	K
p	Pressure	Pa
T	Temperature	K
t	Time	s
ε	Turbulence dissipation rate	m^2/s^3
k	Turbulent kinetic energy	m^2/s^2
TI	Turbulence Intensity	%
σ_h	Turbulent Prandtl number	$[-]$
u_i	Velocity component in the x, y, z directions	m/s
U	Wind speed	m/s

List of Publications

This thesis is presented as an integrated accumulation of three publications. All three manuscripts have been published in peer-reviewed journals.

1.1 Peer-reviewed publications, first author

- El Bahlouli, A., Leukauf D., Platis, A., zum Berge, K., Bange, J. and Knaus, H. (2020). Validating CFD Predictions of Flow over an Escarpment Using Ground-Based and Airborne Measurement Devices. *Energies*. 13(18), 4688.
- El Bahlouli, A., Rautenberg, A., Schön, M., zum Berge, K., Bange, J. and Knaus, H. (2019). Comparison of CFD Simulation to UAS Measurements for Wind Flows in Complex Terrain: Application to the WINSENT Test Site. *Energies*. 12(10), 1992.
- El Bahlouli, A. and Bange, J. (2018). Experimental and Numerical Wind-Resource Assessment of an University Campus Site. *Green Energy and Technology, Springer*.

1.2 Peer-reviewed publications, co-author

- zum Berge, K., Schön, M., Mauz, M., Platis, P., van Kesteren., B., Bange, J., Leukauf, D., El Bahlouli, A., Knaus, H. and Letzgus P. (2021). A two-day case study-comparison of turbulence data from a UAS with a model chain for complex terrain. *Boundary Layer Meteorol.*
- Letzgus, P., El Bahlouli, A., Leukauf, D., Hofsäß, M., Letzgus, T. and Krämer, E. (2020). Microscale CFD Simulations of a Wind Energy Test Site in the Swabian Alps with Mesoscale Based Inflow Data. *J. Phys.: Conf. Ser.*. 1618, 062021.
- Leukauf, D., El Bahlouli, A., zum Berge, K., Schön, M., Knaus, H. and Bange, J. (2019). The impact of a forest parametrization on coupled WRF-CFD simulations during the passage of a cold front over the WINSENT test-site. *Wind Energ. Sci. Discuss.*

1.3 Conference contributions, oral presentations

- El Bahlouli, A., Knaus H., Leukauf D. and zum Berge K. Coupling mesoscale-microscale models for characterising the wind flow in complex terrain. *Wind Energy Science Conference*, Cork, Ireland. 2019.
- El Bahlouli, A. and Bange, J. An experimental and numerical study of the air-flow around university buildings in Tübingen. *European Geosciences Union Conference*, Vienna, Austria. 2015.
- El Bahlouli, A. and Bange, J. Wind resource assessment of the campus of Tübingen. *COST Action TU 1304 Workshops*. Belgrade, Serbia. 2015.
- El Bahlouli, A. and Bange, J. An experimental and numerical study of the airflow around university buildings in Tübingen. *WINERCOST Strategic Workshop: Trends and Challenges for Wind Energy Harvesting*. Coimbra, Portugal, 30-31 March 2015.

Introduction

2.1 Wind energy contribution in climate change

Extreme and very costly weather events, such as floods, storms or bush fires are becoming more evident year by year (Podlaha et al., 2021). Scientists agree that a large portion of those changes are caused by human activities (Cook et al., 2016). As a response, the number of climate protest movements is exploding, with the request to turn to 100 % renewable energy as soon as possible. The awareness of the seriousness of the climate crisis is even taken into account in companies. Lots of companies are sustainably investing with goals to reduce their carbon footprint or even becoming carbon neutral by the next decades.

The intense deployment of mature renewable technologies has lead to a cost decline. In 2019, an important milestone was reached, when 56 % of added renewable capacity (primarily from solar, wind and hydropower) was less expensive than the cheapest coal plants (Taylor et al., 2020). Among the cheaper clean energy sources, wind energy (onshore and offshore) is quickly penetrating the marketplace due to its competitive costs, driven by falls in turbine prices and more efficient technologies. Over the last 10 years, i.e between 2010 and 2019, the cumulative installed capacity increased worldwide by 233 % and 812 % for onshore and offshore wind, respectively (Taylor et al., 2020). However, onshore remains more attractive than offshore as regards the levelized cost of energy (LCOE). Optimal or attractive locations for onshore turbines, such as flat terrains, are mainly already occupied or populated. Therefore, alternatives locations should be considered in more complex terrains. The last one is defined by the International Standard IEC 61400 (International Electrotechnical Commission, 2017) as a ‘terrain surrounding the test site that features significant variations in topography and terrain obstacles that may cause flow distortion’. Hilly, mountainous locations or even the built environment are examples. Built-environment wind turbines are in trend and become a good option for localized power generation, which can be easily integrated within the urban environment and satisfy the in-situ demand (Baniotopoulos and Rebelo, 2015).

Assessing how much energy a wind power plant will deliver over the lifetime of a turbine is called wind resource assessment (WRA). The quality of a WRA has a significant impact on the output of a single turbine or wind park. The WRA should also be accurate because the available energy is susceptible to even small differences in wind speeds, due to the cubic relationship between wind velocity and power density. An error of 1 m s^{-1} for an observed wind of 10 m s^{-1} results in a wind power error of 33 % (Cheng et al., 2013). The awareness of the importance of uncertainties obtained during a WRA has led experts from industry and academia to complement the standard IEC

61400. The coming guideline IEC 61400-15 (Filippelli, 2019) will ‘prescribe standard reporting elements and considerations during the analysis process, and recommend practices to reduce uncertainty for all elements of the assessment and the campaign’.

One classical and reliable approach to provide a detailed site characterization consists of wind measurements at the potential site for a long time period. However, such experiments provide information for some specific locations within an area. Models can overcome this issue and can be used to estimate the wind resource in a wider area. Approaches combining measurements and simulations are the best way to identify optimal turbine locations and to provide better predictions.

2.2 Atmospheric flow

One of the ‘grand challenge’ identified in wind energy research is the need for improved understanding of the atmosphere at the future locations (Veers et al., 2019). Wind turbines extract energy from the winds occurring in the lowest levels of the atmospheric boundary layer (ABL). The ABL, defined as the part of the troposphere which is directly influenced by the Earth’s surface at a timescale of about an hour or less (Stull, 1988), is experiencing a daily cycle. The ABL thickness can vary between few hundred of meters up to a few kilometres. Under fair weather conditions, three major states can be identified: the convective boundary layer (CBL), the residual layer (RL) and the stable boundary layer (SBL), as illustrated in Figure 2.1. The CBL appears during the course of the day, as the surface is heating up and causes strong shallow updrafts and mixing through the ABL. As the sunset approaches, the surface is cooling due to the emission of longwave radiation causing the detachment of the convectively mixed layer and creating the RL. Near the ground, a SBL forms and stays capped by the RL until the next sunrise. All those atmospheric stability states are associated with different wind speed, direction, temperature or turbulent characteristics. Prior studies have shown that the atmospheric stability directly affects the wind turbines output, their load and lifespan. For example, Wharton and Lundquist (2012) found by analysing one year data from a wind farm in Western North America, that the turbines over-performed during stable conditions, while the strongly convective states led to under-performance. Santos et al. (2015) made the same observation by analysing power output from a small wind turbine installed in a suburban area in Brazil. This is related to the fact that a SBL is generally associated with a weaker atmospheric turbulence in comparison to a CBL.

Characterizing the ABL is also a challenging task because of the different spatial and temporal scales involved. Figure 2.2 shows the characteristic scales involved in wind turbine projects. Wind energy is supplied at a macro scale with motions in the order 1000 km and several days in the time scale and dissipated at a microscale with turbulent scales in the spatial and temporal order of 1 mm and 1 ms, respectively.

As already mentioned, future onshore turbines will mainly be located in complex terrains. In this context, the ABL is not only regulated by the diurnal cycle but also by its interactions with the surface, resulting in a more complex flow. Obstructions like buildings, forests contribute to turbulence production and new thermal/mechanical phenomena such as the sweep–ejection, gravity waves, flow separation or wind gust can appear.

2.3. Atmospheric measurements

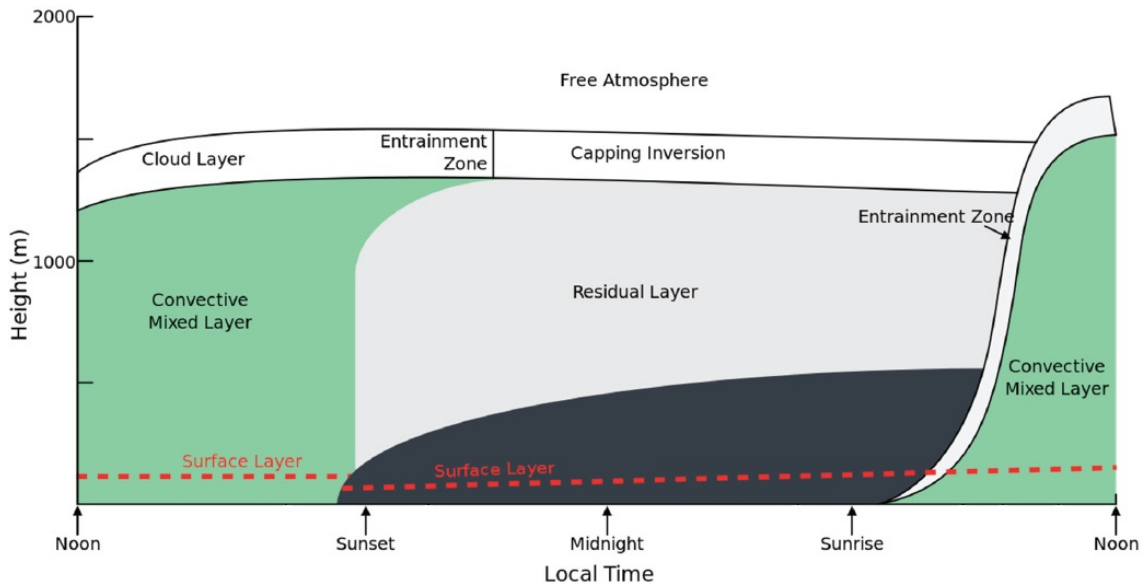


Figure 2.1: *Typical diurnal cycle of the ABL from Stull (1988)*

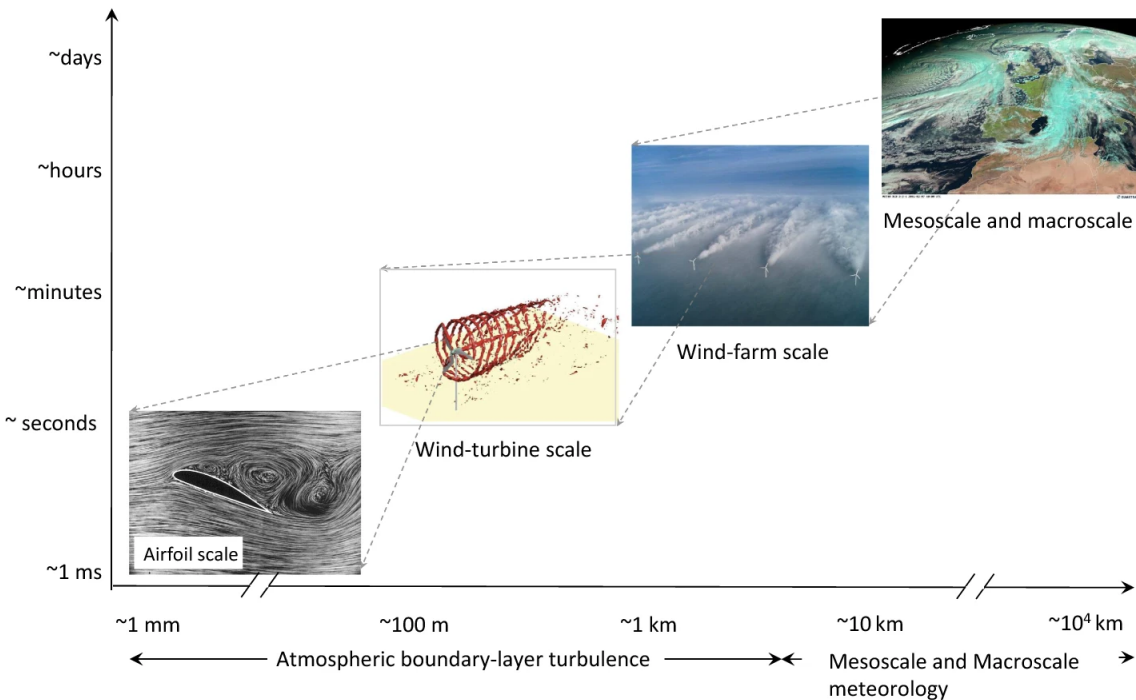


Figure 2.2: *The cascade of scales relevant to wind energy from Porté-Agel et al. (2020)*

2.3 Atmospheric measurements

Today, most investors and directives request in situ measurements to reduce the uncertainty on the estimated wind resources. By increasing the quality and quantity (over time and space) of measurements, the estimated annual energy production is getting more accurate (Bailey et al., 1997; Deutsche Institut für Normung, DIN, 2019).

Meteorological instruments mounted on tall towers are the traditional equipment for resource assessment. The vertical information is provided by instruments installed at several discrete levels and can deliver wind or temperature profiles, for instance. Each of these instruments provides continuous recording of the investigated variables over

long time periods. In order to get an estimation of the turbine power curve and avoid to extrapolate speed measurements, the height of those towers should ideally exceed the total height of the turbine. Erecting a meteorological tower become very costly and sometimes technically difficult if the new tower follows the growing size of wind turbines, which are nowadays getting higher than 100 m.

Remote sensing techniques become an alternative to towers. In recent years, the acceptance of remote sensing technologies is growing. Among them, lidars are the dominating technology. They are often mobile, easy to install, regardless of terrain, and can measure up to several hundred meters. Lidars have undergone several validation processes and are now appearing in a new standard, allowing them to be used as an alternative measurement technique to towers (International Electrotechnical Commission, 2017). Lidar technology has shown its ability to measure accurately the wind speed and direction, contrary to turbulence measurements (see Sathe and Mann, 2013 for a complete review). The main reason is due to the large volume at which the lidars are probing and averaging. To retrieve the wind speed and its variability, lidars perform conical scanning and average over several scanned circles. This means that only turbulence with a length scale bigger than the diameter of the scanning circle is resolved (Sathe et al., 2011; Bauweraerts and Meyers, 2021). Therefore the contributions from small eddies are filtered out.

Most profiling lidars assume horizontal homogeneity of the wind-field over the scanned volume. This assumption is violated in complex environments, where the spatial heterogeneity and transient features introduced by terrain are present. Interpreting the line of sight wind speed and reconstructing the wind-field becomes difficult and errors in the horizontal wind of the order of 10 % (Menke et al., 2020) are measured. Communities, like the International Energy Agency Wind Task 32 aim to tackle open questions regarding the use of wind lidars in complex flow (Clifton et al., 2018). The simultaneous deployment of two or more lidars to reconstruct the flow field is one of the encouraging approach found for studies in complex terrain. Limitations of this method are mainly the high costs and the uncertainties (Pauscher et al., 2016).

Other new emerging techniques for wind-energy applications are flying platforms. Small unmanned aircraft systems (UAS) are not entirely new for ABL research. The first prototype developed to measure pressure, altitude, temperature, relative humidity, airspeed and vertical velocity goes back to 1970 (Hill et al., 1970). Since then, improvements has been made and platforms able to sample, at very high temporal and spatial resolution, emerged (van den Kroonenberg et al., 2008). Through time, UAS extended their range of applications and have contributed to a better understanding in atmospheric turbulence parameters (Hemingway et al., 2020; Balsley et al., 2018), in aerosol formations (Altstädter et al., 2015; Platis et al., 2016), storm developments (Cione et al., 2016) and the monitoring and prevention of forest wildfires (Merino et al., 2011). An increasing interest in UAS technology is also shown for wind energy purposes as they have the advantage to be versatile, even in highly complex terrain. In comparison to towers and active remote sensing techniques, the required infrastructure is small. These systems can provide direct measurements in the close vicinity of a wind turbine, even at very low altitudes where the main vertical and horizontal inhomogeneities are occurring. UAS have for instance been used for the measurements of blade-tip vortices (Mauz et al., 2019) or wind speed deficits (Båserud et al., 2014) in the wake of a wind turbine.

For a global overview of the instrumentation available for wind energy application, including their technology readiness level, the reader is referred to the report from Lundquist et al. (2019).

2.4 Atmospheric modelling

In flat areas, the wind data from a tower can be used to extrapolate the information to another location using measure-correlate-predict (MCP) methods (Carta et al., 2013). For topographically complex locations, a single meteorological tower (or lidar) is not able to capture the temporal and spatial variability of the flow. Therefore several towers or lidars are necessary to represent the wind climate in those locations. There is no general agreement on the duration of the measurement campaigns. Some countries like Brazil set up a minimum length for short-term datasets to 36 whole months (Miguel et al., 2019). However, several authors (Rogers et al., 2005; Miguel et al., 2019) agree that the longer the measurements are running, the more accurate the predictions are. Carrying out measurements with several towers or lidars over such long period become very costly. The use of a wind flow model, able to extrapolate the measurements to potential wind turbine location, is an alternative.

In complex sites, modelling appropriately the overlaying atmosphere is challenging due to the different length scales, ranging from the integral down to the Kolmogorov length scales (Porté-Agel et al., 2020). Orography (elevated terrain such as mountains or hills) is known to affect the local weather and induces dynamical processes at a wide range of spatial and temporal scales. Effects such as wind increase or reduction, heavy rain, fog or lee waves are appearing. One example of the poorly resolved and modelled process are the orographically-generated gravity waves occurring in stable stratification. They are known to modify the turbulent transport of momentum, heat and moisture between the ABL and the surface (Vosper et al., 2018). Elements such as buildings or trees also impact the turbulent structures in the surface layer. Plant canopies change the flow by creating an internal boundary layer above the canopy and an inflection point in the velocity profile creates just above the trees. The formation of three dimensional vortices with a horseshoe shape (Rogers and Moser, 1992) can appear. These structures give rises to ‘sweeps’ which are the dominant transport mechanism. Wang et al. (1992) found for an 8 m tall almond orchard that the length scales in the longitudinal direction are bigger than those in the lateral direction. For a detailed analysis on the processes involved in forest canopies at complex terrains, the reader is referred to the review of Belcher et al. (2012).

Although resolution for the orography or topography can today be provided in the order of a few meters, getting all the process generated by the surface remains challenging for the models. The wide range of models used for wind energy studies shown in Figure 2.3 and reported in Sanz Rodrigo et al. (2017), illustrates well the typical models and their approximate spatial and temporal resolution. For site suitability studies, two categories are used: the mesoscale and microscale models. They both are numerically solved in different ways: the majority of the mesoscale models use finite difference discretization while the microscale one are based on a finite volume method.

2.4. Atmospheric modelling

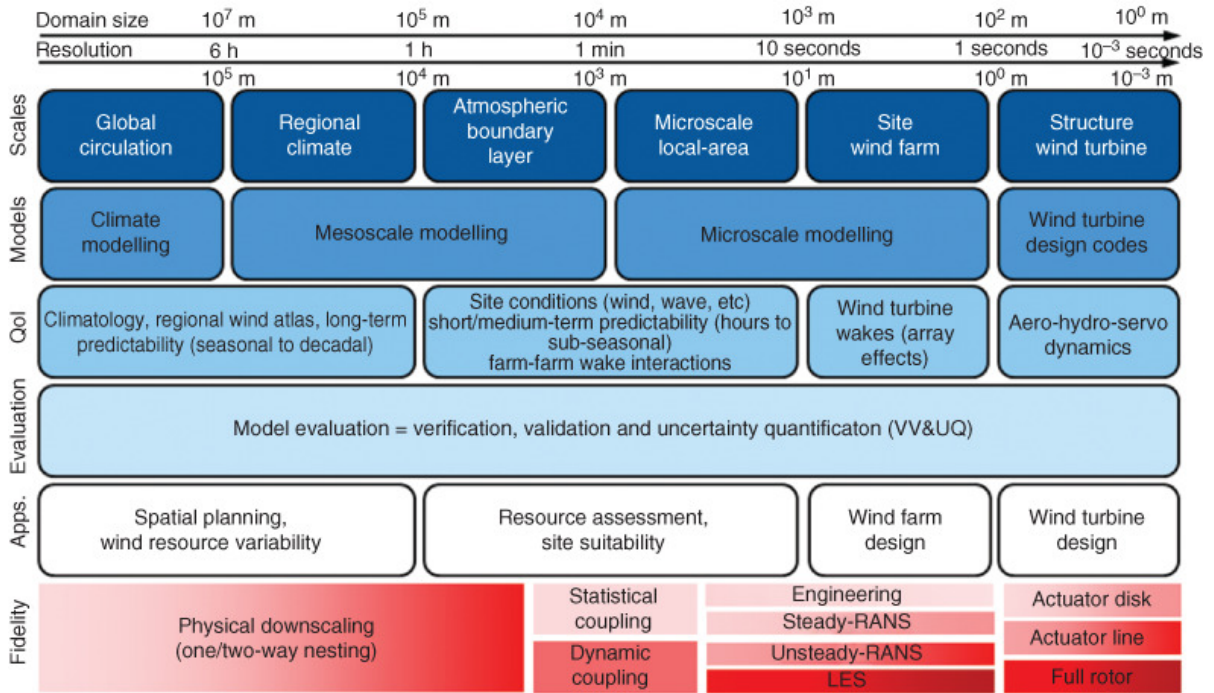


Figure 2.3: Overview of the models used for wind resource studies and their associated time and horizontal scales (Sanz Rodrigo et al., 2017). The red shading intensity indicates the computational costs.

The first category is used by meteorologists to primarily characterize the weather over several hours to several days. Those models are commonly based on fully compressible dynamic equations and include parametrizations for the small-scale physical processes (smaller than the grid scale of the model), such as the cloud, solar and thermal radiation, boundary-layer turbulence, land surface, and so forth. A popular code used in wind industry is the WRF model (Weather-Research-Forecast, Skamarock et al., 2008) developed by the National Center for Atmospheric Research. Supported by the advances in computational capabilities, mesoscale models are more and more operated at finer grid (few hundred meters) and can be therefore used for wind resource assessment or power production assessment by parametrizing the turbine (Fitch et al., 2012). Most of the existing studies have been however performed for offshore studies or relative gentle onshore sites. When applied to complex terrains, those models need a higher resolution to follow the terrains which present moderate and steep slopes. This approach is not satisfactory as numerical errors or noise are appearing (Zängl et al., 2004; Flores-Maradiaga et al., 2019).

The second category consists of microscale models, commonly named computational fluid dynamics (CFD) models. They are enable to solve the flow at finer temporal and spatial resolution. If fine enough, even the interaction of the ABL with wind turbine blades can be modelled. While many models exist, two approaches are dominating the wind energy industry and research: the Reynolds Averaged Navier Stokes (RANS) and Large Eddy Simulation (LES) models. The governing equations are the continuity and the momentum equations, also called Navier-Stokes equations. The instantaneous three dimensional Navier-Stokes equations, when applied to a portion of compressible Newtonian fluid, in a Cartesian coordinate system read:

$$\frac{\partial}{\partial t}\rho + \frac{\partial}{\partial x_i}(\rho u_i) = 0 \quad (2.1)$$

$$\frac{\partial}{\partial t}(\rho u_i) + \frac{\partial}{\partial x_j}(\rho u_i u_j) = -\frac{\partial p}{\partial x_i} + \frac{\partial}{\partial x_j} \left[\mu \left(\frac{\partial u_i}{\partial x_j} + \frac{\partial u_j}{\partial x_i} - \frac{\partial u_k}{\partial x_k} \delta_{ij} \right) \right] + \rho F_i \quad (2.2)$$

where $u_i (i = 1, 2, 3)$ are the velocity components in a Cartesian framework (x, y, z) , ρ and μ are the fluid density and dynamic viscosity, p is the fluid pressure, t represents time and F_i are the external forces. These can include Coriolis effect, forest drag, etc. When the temperature is considered, the convection-diffusion equation for the temperature is:

$$\frac{\partial}{\partial t}(\rho T) + \frac{\partial}{\partial x_j}(\rho u_j T) = \frac{\partial}{\partial x_j} \left[\frac{\lambda}{c_p} \left(\frac{\partial T}{\partial x_j} \right) \right] + \rho F_T \quad (2.3)$$

T is the temperature, c_p the specific heat capacity, λ the thermal conductivity and F_T the heat source-terms. These can be produced by solar radiation or from ground heat fluxes for example.

RANS models are based on an ensemble-averaged equations where the flow is separated into an instantaneous flow u and a mean flow U . The mean flow is solved while all other scales are modelled, that is approximated. In the LES approach, a spatial filtering approach is used. A low-pass filter Δ is applied and only eddies, smaller than Δ , also called subgrid-scales SGS (Smagorinski, 1963), are modelled. The large eddies, determined by low-pass filter size Δ , are directly resolved. It means that only processes which have a length scale bigger than filter size Δ are resolved. Ideally, the grid resolution should be much smaller than the turbulent length scale to have most of the turbulent energy cascade. This is however not possible near the ground as the eddies are getting very small and thus a huge amount of cells is needed in these regions. LES models are known to be generally more accurate than the RANS models as they resolves the large scale dynamics and provide more turbulence information. On the other hand, LES models are not a tool for daily activities in wind industry due to the higher computational resources. The accuracy obtained by a RANS model, when used following the guidelines, is sufficient for several research and engineering problems (Blocken, 2018). A detailed overview of the different approaches for modelling can be found in the books of Versteeg and Malalasekera (2007) and Pope (2000).

For WRA studies, the microscale models are usually used by prescribing a stationary profile at the inlet. Additionally, to consider the different wind conditions occurring at the potential site, the simulations are repeated by setting several inlets (boundary conditions) for each wind direction. This method has been intensively practised in the wind industry but shows limitations in locations with steep terrains and where important mesoscale flow patterns are presents. Dynamic processes of the atmosphere like atmospheric stability, low-level jets, land-sea breeze can not be described by these ide-

alized profiles and need information from mesoscale models. Only weather models can reproduce real local atmospheric conditions and provide the diurnal information.

Using those information from a weather model to feed a microscale model is referred in the literature as meso-microscale coupling (Castro et al., 2015; Duran et al., 2020; Montelpare et al., 2019). Coupling both models through the lateral boundary conditions is the most common approach. In this method, the variables from the mesoscale model are interpolated onto the lateral boundaries of the nested microscale model. Meso-microscale coupling has been found to improve results, in comparison to use of microscale models alone, for urban flow and pollutant dispersion studies (Tewari et al., 2010; Kwak et al., 2015), wind power forecasting (Duraismy et al., 2014), and more. However, grey zones appears when applying the meso-microscale downscaling. One of the problem encountered with this method is the horizontal grid resolution at which the transition from mesoscale to microscale modeling is operated. In mesoscale models, the grid length is larger than the turbulent eddies L as illustrated in Figure 2.4 a from Chow et al. (2019). The turbulent eddies are filtered out and parametrized by the models. In the microscale modelling, the grid resolution Δ is smaller than the dominant length scales and most of the turbulence, in the LES case for example, are resolved (see Figure 2.4 b). At some point, the meso-microscale transition fails under the range of scales where the ratio of the energy-containing eddies L are comparable to the spatial filter size Δ , as illustrated in Figure 2.4 c. In this situation, traditional assumptions made in the mesoscale and microscale modelling are violated. Neither a mesoscale model nor a microscale model is designed to model within this range, also called *terra incognita* (Wyngaard, 2004). The *terra incognita* depends on the atmospheric conditions and thus subject to a diurnal and spatial variation. The understanding of the scales involved in this range is important for the wind industry as it can reaches scales that drive wind turbines, specially in a SBL. To better simulate in the *terra incognita*, research on the development of new turbulence closure (Wyngaard, 2004; Kitamura, 2016) or a new formulation for the parametrization of the convection (Chow et al., 2019) is ongoing. An alternative way to avoid the challenges created by this transition is to skip over the *terra incognita* by using high nesting ratio (Chow et al., 2019).

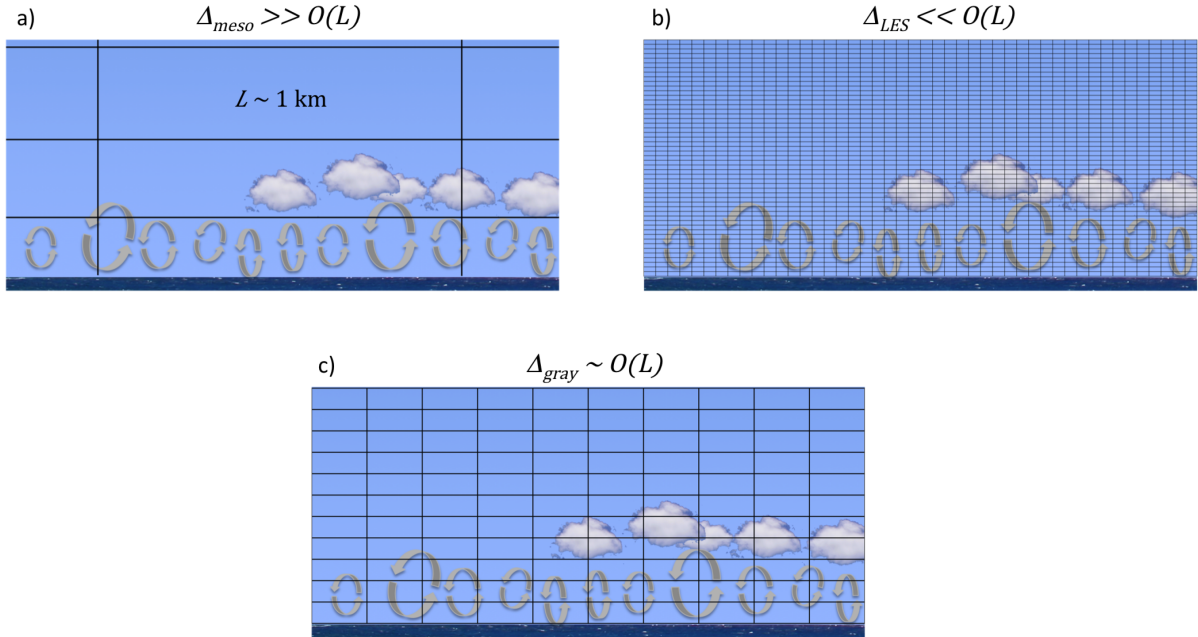


Figure 2.4: *Eddies of 1 km and the associated grid resolution for a mesoscale model (a), a LES-based microscale model (b) and in the terra incognita (c). Figure from Chow et al. (2019)*

Regardless of the chosen modelling approach, the simulation outcome can be very sensitive to a broad range of parameters, mainly chosen by the user. Each model is based on formulations which include a lot of assumptions to simplify the problem. Identifying first-order physics, i.e the most significant ones, can help considerably to improve the model outcomes. For wind energy applications, CFD models did not usually include thermal effect as the weather models. This aspect is progressively more integrated even in the commercial code as the atmospheric stability have been recognized of importance in the wind industry. When considering big turbines, other processes such as Coriolis forces can interact with the turbines. The humidity has also been recognized to impact the performance of a wind turbine, mainly in offshore sites. Another important parameter for numerical studies in complex terrain is the ground representation. Ideally, a high-resolved terrain and its land cover representation should be used for the computational domain generation. Lange et al. (2017) found that using a sharper edge of the escarpment of the Bolund peninsula leads to an increase of the turbulence level by a factor of five and a reduction of the annual energy production by 50 %.

Computer models, whatever the chosen approach, and on-site measurements each have their benefits and limitations. One of the main constraints for model development is the lack of on-site measurements for the model validation. Awareness of this issue has led countries and institutions to fund several field projects over the last years. Examples are the Wind Forecast Improvement Project (WFIP2) in the U.S (Shaw et al., 2019), the Perdigao field experiment in Portugal (Fernando et al., 2019), the Alaiz Experiment in Spain (Santos et al., 2020) or the WINSSENT (zum Berge et al., 2021; El Bahlouli et al., 2019) and Kassel (Klaas et al., 2015) experiments in Germany. All the numerical work presented in this thesis uses on-site measurements to measure the accuracy of the model.

2.5 Objectives and outline of this work

The major aim of this thesis is to study the flow over complex sites and identify physical parameters and methods that can improve the wind flow prediction for wind assessment studies. Motivated by using a modelling framework which delivers quick results and is able to catch the interaction between the boundary layer and the ground thanks to a vertical mesh refinement, all the modelling work in this thesis is assessed using RANS models in combination with a $k - \varepsilon$ model (Launder and Spalding, 1974). This can hardly be done with a LES due to the huge amount of cells needed near the surface. Not motivated by resolving the high temporal resolution of the eddies, the RANS approach is hence the suitable model. The surface roughness (forest, urban, farmland, etc.), the terrain (flat, hilly, etc.), the Coriolis force, the flow stratification and the humidity are aspects that have been implemented in this thesis in order to simulate the wind flow in complex terrains.

The work presented in this thesis is mainly based on three journal publications and the main outcomes are presented in chapter 3 as follow:

- The first publication presents the wind flow in an urban environment. The site includes a forested region and to mimic the wind flow behaviour at such areas, canopy models are applied and assessed using conventional wind sensors, that are sonic anemometers.
- The second and third publications present a wind flow study in a complex terrain in the Swabian Alb in Southern Germany. As for the first study, canopy models are used. To adapt the model for ABL flows, the thermal stratification, the Coriolis and humidity effect are included and the standard $k - \varepsilon$ model has been modified to account the turbulence generation and destruction due to buoyancy. Improved predictions of the flow at the site are also done by coupling our model with numerical weather predictions models. The coupling is performed through the lateral boundary conditions using a one-way approach, in which the flow information of the microscale model is provided by the coarse model (weather model). Since we deal with non-stationary flows, the time-derivative in equations 2.1, 2.2 and 2.3 are retained and the unsteady RANS (referred to URANS) approach is kept. The work includes validation with tower and UAS measurements.

In the last chapter, the conclusion of this work, along with open questions and perspectives are presented.

Results

The results presented in this chapter are based on the outcomes from the articles attached to this thesis (see appendices A.1 to A.3).

3.1 Publication 1: The wind flow in an urban environment

Harvesting wind energy from urban areas is more challenging than in rural areas as the wind speed is generally weaker, the wind direction gets rapidly deflected by buildings and the turbulence is higher. An urban wind study should ideally combine experimental (on-site) and numerical methods. Direct measurements of wind speed over a long period of time are not common and expensive as it would require too many stations with high resolution data. That is why most of the studies are conducted using analytical methods (Drew et al., 2013; Millward-Hopkins et al., 2013; Popovac, 2012), wind tunnels (Al-Quraan et al., 2016; Tominaga et al., 2004) or/and only CFD models (Ricci et al., 2017; Toja-Silva et al., 2018). In the present study, the wind flow over an university campus site is investigated using long term measurements (2 years) combined with a CFD model. The chosen site, called Morgenstelle, offers the highest wind speed among the university buildings as it is located on the top of a hill. The majority of the buildings have a rectangular shape orientated against the prevailing wind in the area, which is 240°. Three of the buildings are approximately 50 m height.

The experimental set up consists of six stations installed at different locations on the campus as shown in Figure 3.1. Most of the stations are located on the top of the buildings, except for two stations. The station 5 ‘garden’ is located on the leeward side of the highest building and the station 3 ‘balcony’ is mounted on a horizontal boom mast at a building corner. Effects such as acceleration, separation, channel or dead zone, in case of a south-west wind, should be recorded by these two stations. The stations consist of ultrasonic anemometers with data acquisition systems recording the velocity components and temperature at 20 Hz. A large amount of data, around 300 MB per day, is generated and a database management system based in SQL language was necessary to access and retrieve required data.

The simulations are performed with the open source code C++ OpenFOAM (Weller et al., 1998) using a RANS approach. The computational domain is build according to the COST 732 Action recommendations (Franke et al., 2011). Considering these guidelines, the computational domain size in the vertical, lateral and flow directions is 350 x 750 x 1250 m³. A volume mesh containing approximately 8 million cells with a



Figure 3.1: *The Morgenstelle site and the station network shown with the red dots.*

resolution of 1.5 m near the area of interest is generated using SnappyHexMesh, the native OpenFOAM mesh generator. The ground is assumed to be flat as no terrain data was available at that time. The simpleFoam solver, a steady state incompressible solver, is used with a $k - \epsilon$ model for the turbulence closure. A Dirichlet condition is applied at the inlet for the velocity and turbulent quantities k and ϵ . The log-law profile from the OpenFOAM libraries (Richards and Hoxey, 1993) with a reference wind speed of 5 m s^{-1} at 10 m height is used. The standard OpenFOAM wall function with an homogeneous roughness length of 0.03 m is applied to the ground. A slip boundary condition is used at the sides and top of the domain.

The inflow region, west to the campus, has a gentle valley covered with forest. To reproduce the effect of the forest on the flow, a canopy model based on the work of Shaw and Schumann (1992) is used. In their approach, the forest is considered as a porous media added to the momentum equation:

$$F_h = -C_d \text{LAD}(z) |U| u_i \quad (3.1)$$

where C_d is the drag coefficient, $|U|$ the velocity magnitude, u_i the velocity component in i direction and LAD is the local leaf area density. The foliage structure of the trees is often discretized in horizontal layers and by integrating vertically the LAD over the total tree height H , the leaf area index LAI is obtained as follow:

$$\text{LAI} = \int_0^H \text{LAD}(z) dz \quad (3.2)$$

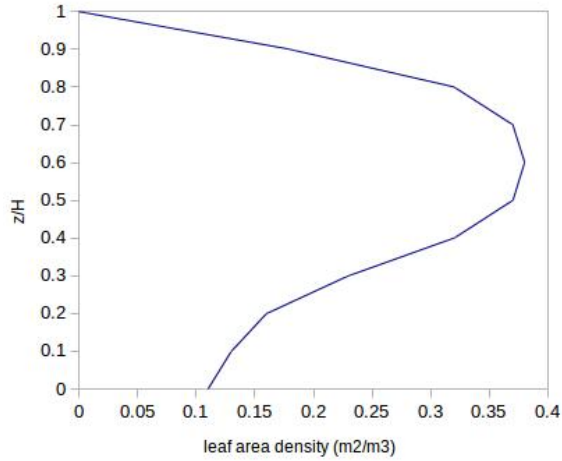


Figure 3.2: *Vertical distribution of the leaf area density*

In our study, the site is mainly covered by a mixed forest with coniferous and mixed trees. A drag coefficient C_d of 0.15 (Cescatti and Marcolla, 2004) is used and the forest is considered with a uniform height of 22 m and a LAI of 5 as shown in Figure 3.2. The simulations are conducted by setting only a roughness length in a first step. Secondly, the canopy model described by equations 3.1 and 3.2 is applied to the forested areas. Figure 3.3 shows the simulation results in terms of wind speed at 2 and 50 m height. The inclusion of a canopy model decreases strongly the wind speed at pedestrian-level. Before reaching the buildings, the wind speeds near the ground are lower than 1 m s^{-1} with the use of a canopy model, while the case without forest leads to values around 3 m s^{-1} . The canopy model reduces the wind speed between the buildings but also deviates the wind direction in some areas. This can be seen at the front at the highest building (station 4), where the size of the vortex is bigger compared to the case without canopy. The forest effect decreases with increasing altitude but still some differences on the building wakes are visible at 50 m.

The station 4 mounted on building ‘A’ is considered as reference point for our model comparison. Station 4 is not affected by other buildings in case of south-west wind. The simulation results, obtained with the log-law profile at the inlet, give at station 4 a velocity of 5.4 m s^{-1} with a wind direction of 240° . For the model verification, we pick out in our SQL database the 30-min means which agree with our simulation results at position 4 and thus fulfilling both conditions:

- The wind speed is $5.4 \pm 0.1 \text{ m s}^{-1}$
- The wind direction is $240 \pm 10^\circ$

28 data sets were found, which fulfill both conditions at station 4. The measured and simulated wind speed at the other stations are shown in the scatter plots in Figure 3.4. The scatter plot using only a roughness length on the ground (Figure 3.4a) shows a clear overestimation of the simulated wind speed over the experimental measurements. A consistent spread of approximately 2 m s^{-1} across the experimental values is observed. An interesting outcome are the values from station 5 (‘garden’) and station 3 (‘balcony’). They both show a better fit in comparison to the other stations. This can be easily explained by their locations on the campus. Station 5 is located behind a building,

3.1. Publication 1: The wind flow in an urban environment

while station 3 is right at the corner of a building and thus those stations are rather affected by the buildings regardless of the incoming wind-field. The simulation results using a canopy model are presented in Figure 3.4b. For all locations a reduction on the simulated velocities is observed. The station 1 ('heating plant') is still showing an overestimated velocity. This station is located only 30 m away from the forested valley and thus very sensitive to the canopy model. A good agreement is generally achieved between the simulated and measured wind speed by using a simple canopy model. Further improvement may have been achieved by considering the real local tree height of the forest in combination with the real leaf density.

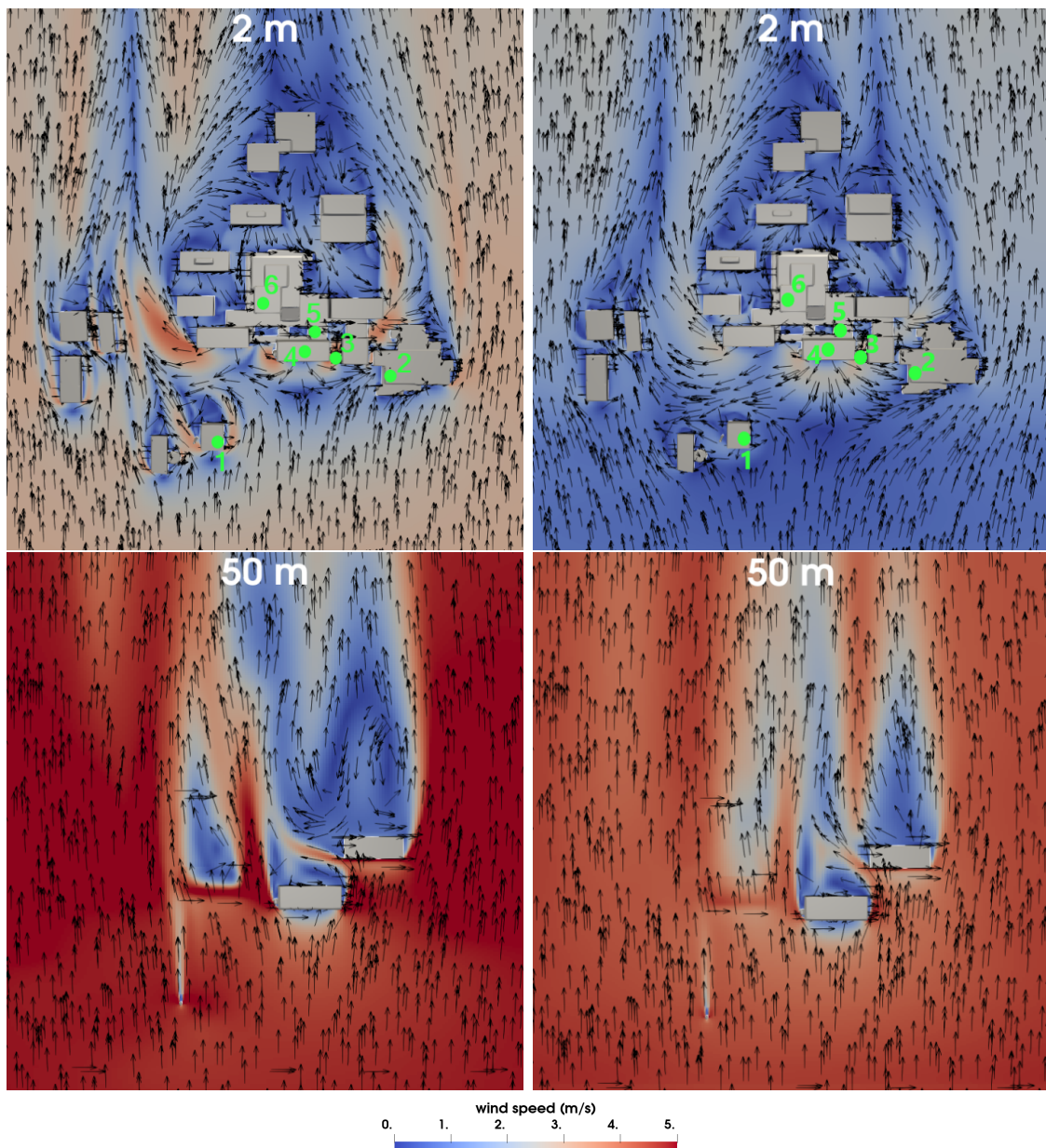


Figure 3.3: Contour of simulated wind speed at 2 and 50 m without (left) and with (right) a canopy model. The green dots denote station locations.

3.2. Publications 2 & 3: The wind flow in a rural area of complex topography

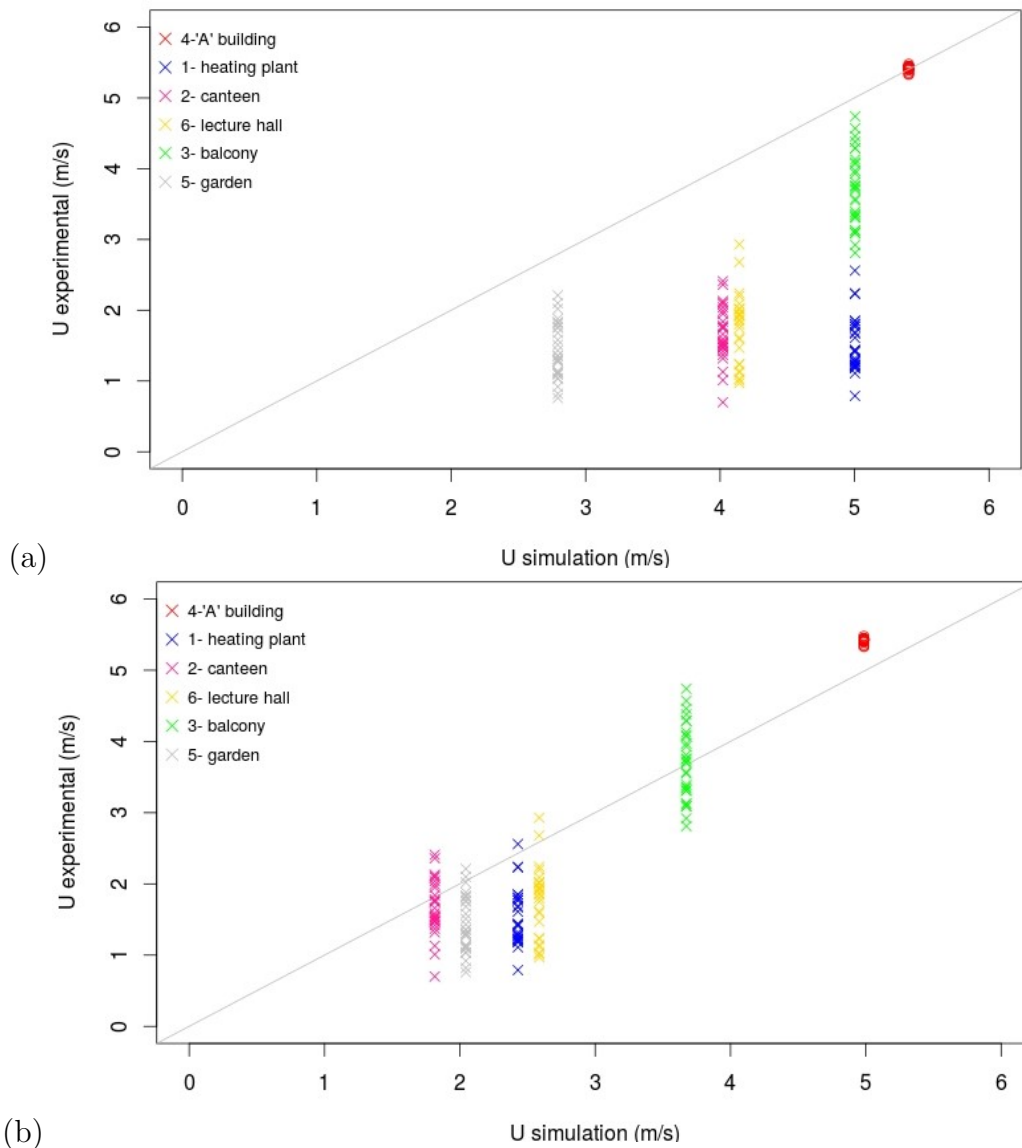


Figure 3.4: Scatter plot of measured wind speed against simulated wind speed without (a) and with (b) canopy model.

3.2 Publications 2 & 3: The wind flow in a rural area of complex topography

In the present section, the wind flow over a complex terrain in the Swabian Alb in Southern Germany is investigated. The chosen site at the Stöttener Jura near Geislingen an der Steige is characterized by a sloping escarpment up to 200 m of around 30° from the Northwest and a more gradual slope of 15° further West (see Figure 3.5). With winds blowing predominantly from the west, a speed-up at, or downstream, of the escarpment is expected and thus ideal for the placement of wind turbines. Within the framework of the WINSSENT (Wind Science and Engineering Test Site in Complex Terrain) project, two wind turbines of around 750 kW nominal output are to be set next to the escarpment. The first phase of the WINSSENT project aims at characterizing the local wind flow without any wind turbine. To achieve this objective, a numerical model together with the multi-purpose airborne sensor carrier (MASC) operated by the Environmental Physics group at the University of Tübingen, Germany (Wildmann et al., 2017; Rautenberg et al., 2019; Mauz et al., 2019) and tower measurements are used. The results presented in this section are part of a larger research effort from the WINSSENT project.

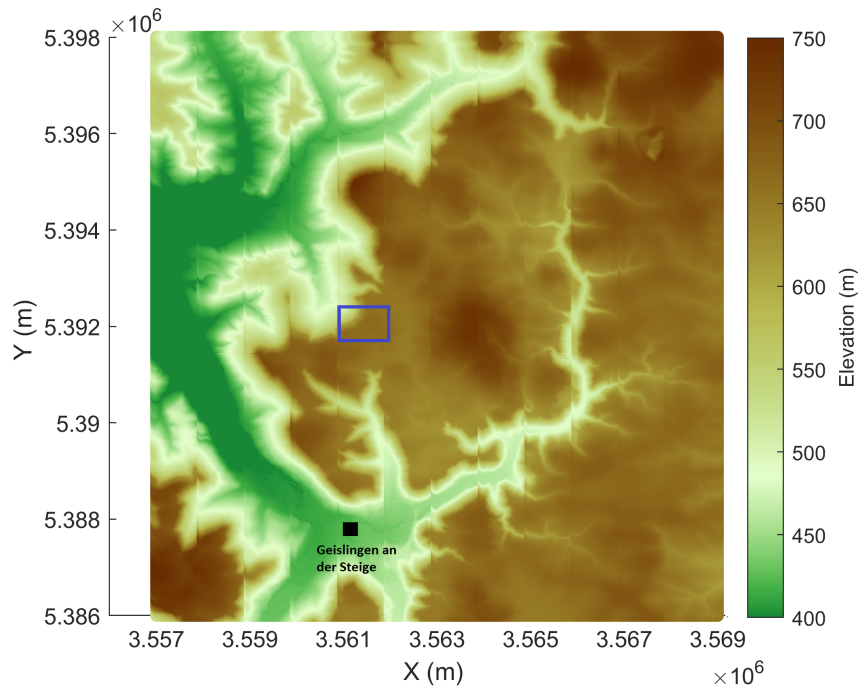


Figure 3.5: Orography with the blue box marking the test-site (Gauß-Krüger coordinates).

3.2.1 Model set up

To simulate the ABL flow in this complex terrain, the OpenFOAM solver is used as for the urban site. The model equations, written relative to a hydrostatic state, are

modified and extended to adapt to atmospheric conditions. The model should be able to provide results for all the encountered atmospheric stability states. That is why, a transport equation for potential temperature is added (El Bahlouli et al., 2019, 2020). To account for buoyancy, the Boussinesq approximation, which assumes the variations in density are only in the gravitational acceleration term, is considered. The governing equations for mass, momentum and potential temperature in a Cartesian coordinate system are written as:

$$\frac{\partial}{\partial t}\rho_h + \frac{\partial}{\partial x_j}(\rho_h u_j) = 0 \quad (3.3)$$

$$\begin{aligned} \frac{\partial}{\partial t}(\rho_h u_i) + \frac{\partial}{\partial x_j}(\rho_h u_i u_j) = & -\frac{\partial p^*}{\partial x_i} + \frac{\partial}{\partial x_j} \left[(\mu + \mu_t) \left(\frac{\partial u_i}{\partial x_j} + \frac{\partial u_j}{\partial x_i} \right) - \frac{2}{3} k \rho_h \delta_{ij} \right] \\ & - \rho_h g_i \frac{\theta - \theta_h}{\theta_h} + F_{Ci} + F_{Di} \end{aligned} \quad (3.4)$$

$$\frac{\partial}{\partial t}(\rho_h \theta) + \frac{\partial}{\partial x_i}(\rho_h u_i \theta) = \frac{\partial}{\partial x_i} \left[\left(\mu + \frac{\mu_t}{\sigma_h} \right) \left(\frac{\partial \theta}{\partial x_i} \right) \right] \quad (3.5)$$

here, $u_i (i = 1, 2, 3)$ are the velocity components in a Cartesian framework (x,y,z, where z is aligned with gravity), p^* and θ are the pressure perturbation from the hydrostatic reference state and potential temperature, μ and μ_t are the dynamic molecular and turbulent eddy viscosities, g_i is the gravitational acceleration term, and σ_h is the turbulent Prandtl number. F_{Ci} is the Coriolis force. The importance of the forest has been in the previous section illustrated. Here again, vegetation effects are included in the drag force F_{Di} . The hydrostatic fluid density ρ_h is defined in a hydrostatic reference state (subscript 0) as a function of the hydrostatic pressure p_h and the temperature T_h as:

$$\rho_h = \frac{p_h}{R_d T_h} \quad (3.6)$$

$$T_h = T_0 \sqrt{1 - \frac{2Agz}{R_d T_0^2}} \quad (3.7)$$

$$p_h = p_0 \exp \left(\frac{-T_0}{A} \left(1 - \sqrt{1 - \frac{2Agz}{R_d T_0^2}} \right) \right) \quad (3.8)$$

where p_0 is the constant reference pressure set to 1000 hPa, T_0 is the reference temperature equal to 288.5 K, $A = 42$ K and $R_d = 287.05$ J kg⁻¹ K⁻¹ (Doms and Baldauf, 2018; Dudhia, 1993).

A turbulence closure using the $k - \varepsilon$ model is chosen. The model has been adapted to ABL by implementing the mixing length model following the approach of Apsley and Castro (1997). This model includes also a source/sink term to account for the production/destruction of turbulence by buoyancy forces:

$$\frac{\partial}{\partial t}(\rho_h k) + \frac{\partial}{\partial x_i}(\rho_h u_i k) = \frac{\partial}{\partial x_i} \left[\left(\mu + \frac{\mu_t}{\sigma_k} \right) \left(\frac{\partial k}{\partial x_i} \right) \right] + P + G + F_{Dki} - \rho_h \varepsilon \quad (3.9)$$

$$\frac{\partial}{\partial t}(\rho_h \varepsilon) + \frac{\partial}{\partial x_i}(\rho_h u_i \varepsilon) = \frac{\partial}{\partial x_i} \left[\left(\mu + \frac{\mu_t}{\sigma_\varepsilon} \right) \left(\frac{\partial \varepsilon}{\partial x_i} \right) \right] + C_{\varepsilon 1}^*(P + G) + F_{D\varepsilon i} - C_{\varepsilon 2} \frac{\varepsilon^2}{k} \quad (3.10)$$

where P is the production rate of turbulent kinetic energy due to shear and G the production/destruction of turbulence by buoyancy forces defined as:

$$P = \mu_t \left(\frac{\partial u_i}{\partial x_j} + \frac{\partial u_j}{\partial x_i} \right) \frac{\partial u_i}{\partial x_j} - \frac{2}{3} \rho_h \frac{\partial u_k}{\partial x_k} \delta_{ij} \quad (3.11)$$

$$G = \frac{-g}{T} \frac{\mu_t}{\sigma_h} \frac{\partial \theta}{\partial x_i} \quad (3.12)$$

F_{Dki} and $F_{D\varepsilon i}$ are the forest-related source terms. The standard $k - \varepsilon$ model coefficients $\sigma_k, \sigma_\varepsilon, C_{\varepsilon 1}^*, C_{\varepsilon 2}$ have been modified to adapt atmospheric flows as proposed by Detering and Etling (1985). The time derivative $\frac{\partial}{\partial t}$ is maintained in all equations to capture time-dependant structure of the atmosphere. Before solving the equations, an initial or boundary conditions need to be prescribed. The required variables are provided by a mesoscale model and feed into our model through the lateral boundaries using a one-way approach (mesoscale to microscale only).

3.2.2 Coupling with a low resolution weather model

In a first step, the coupling is done using data from the COSMO-DE (COntortium for Small-scale MOdelling) weather model developed by a consortium lead by the German Weather Service (Doms and Baldauf, 2018). The model data has a horizontal grid spacing of 2.8 km and uses 20 vertical levels in the lower 3 km. An hourly output from the COSMO model is provided by the DWD. The wind components, pressure, air and surface temperature are selected as boundary conditions for the CFD model. For the coupling, data from 27 March 2015 15:00 UTC are selected to match the experimental measurements. A two nesting step is used: the COSMO-DE data are used at the lateral boundaries for our first domain of 20 x 20 x 20 km³, which has a coarse horizontal and vertical resolution of 25 m and 2.6 m near the ground, respectively. Results from the first domain are then used to provide the boundary data to a nested domain of 5 x 5 x 5 km³ centred on the test site with a finer resolution of around 7 m horizontally and 1.6 m vertically for the bottom cell (see Figure 3.6). The digitized landscape model from the Baden-Württemberg Authorities for Spatial Information is used to prescribe the land cover on the surface. In our study, three types of land cover are defined: ground, urban and forest. An aerodynamic roughness length of 0.50 m and 0.02 m is assigned to the urban and the ground classes, respectively. Additionally, a design of

experiment DoE (El Bahlouli et al., 2019) and a sensitivity study to the LAI and the forest height is done, see Table 3.1 for sensitivity values.

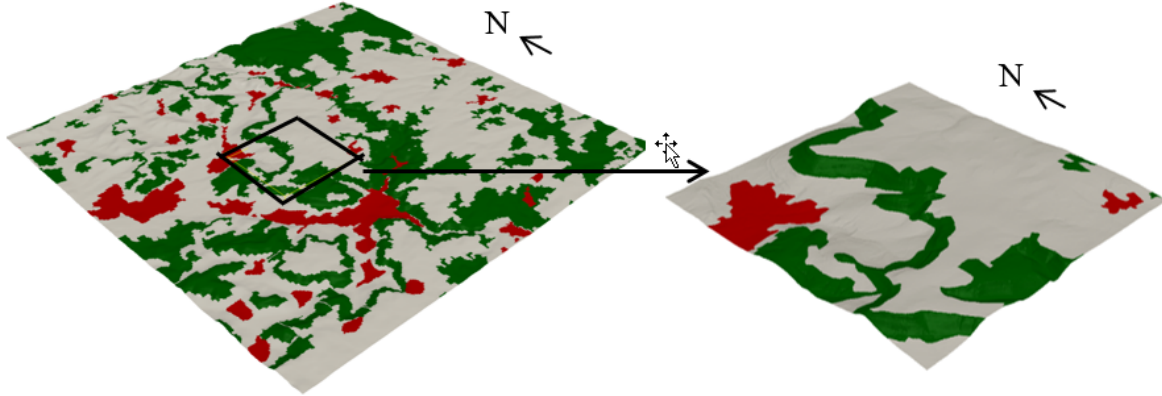


Figure 3.6: *Modeling domains: parent (left) and nested (right). The color indicates the different land uses applied in the simulation: red for urban, grey for ground and green for forest.*

Table 3.1: *Parameter values for the sensitivity analysis*

Run	LAI	Forest height H (m)
Run 1 (no canopy)	0	0
Run 2	2	20
Run 3	2	25
Run 4	5	20
Run 5	5	25

UAS data from the MASC are used for the model validation. A measurement campaign was carried out on 27 March 2015 between 13:00 and 16:00 UTC. The MASC is measuring the temperature and velocity fluctuations over the escarpment by following a vertical grid of racetracks with legs of approximately 1 km going back and forth, in and against the flow direction (see Figure 3.7). Flight measurements start at the height of 75 m above the ground level (AGL) up to 200 m. For the data processing, the UAS measurements are averaged over subsections of 20 m in length along each leg.

For a better understanding of the flow structure over the escarpment, results from the nested domain at different altitudes are shown in Figure 3.8. The case with a leaf area index of 2 and a forest height of 20 m is selected (run 2 from Table 3.1). The black line corresponds to the position of the leg performed by the MASC at the same altitude. Strong velocity gradients are visible, with a high speed-up zone appearing over the escarpment, where the flight is conducted. This is very noticeable on the lower levels, with stripe patterns appearing at the escarpment and extending far downstream.

3.2. Publications 2 & 3: The wind flow in a rural area of complex topography

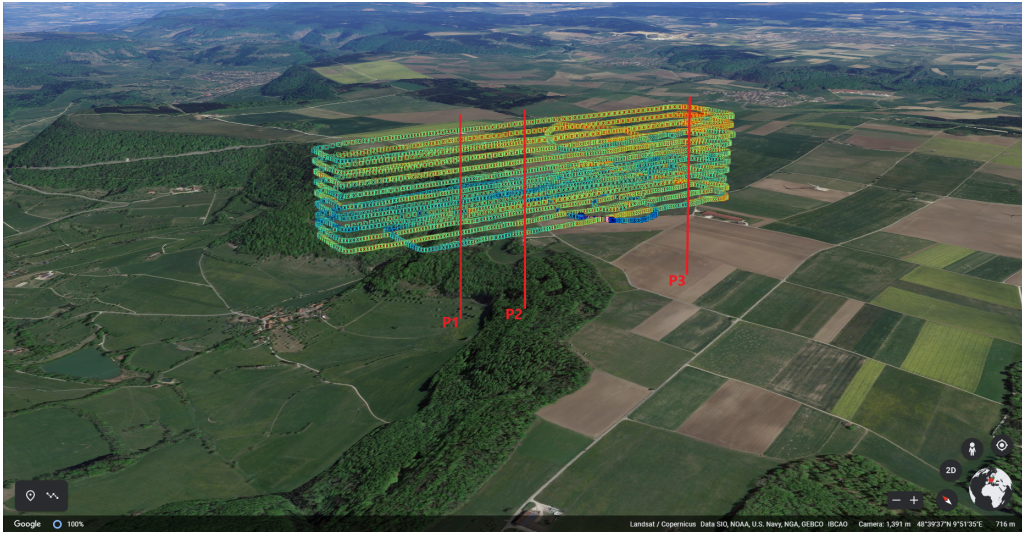


Figure 3.7: The flight patterns performed on 27 March 2015. The colours along the legs indicate the measured horizontal wind speed. The vertical lines marks the positions for the evaluation related to Figures 3.11 and 3.12.

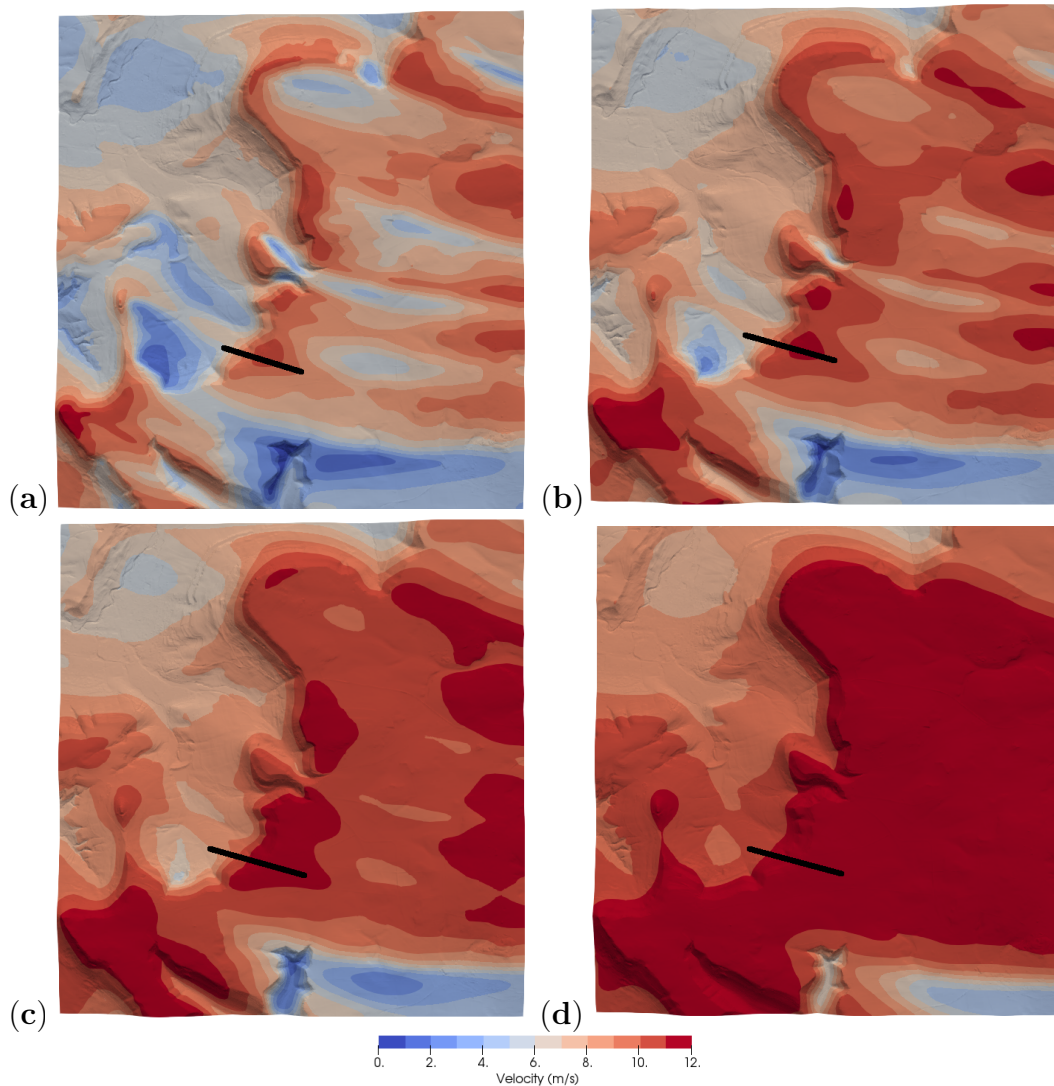


Figure 3.8: Velocity contour plots at 75 m (a), 125 m (b), 175 m (c) and 275 m (d) AGL on 27 March 2015. The black lines denote to the UAS flight path.

3.2. Publications 2 & 3: The wind flow in a rural area of complex topography

Results from the simulated and measured horizontal wind speed along the performed flight path for different altitudes are presented in Figure 3.9. The wind speed results show a horizontal profile getting flat with increasing altitude. This can be explained by a flow becoming more homogeneous with increasing altitude as the terrain effects are getting smaller, confirmed by the contour plots from Figure 3.8. At 75 m, a maximum is recorded by the MASC at a distance of 500 m, as the simulation does. The wind speed increases from 9 m s^{-1} to about 10.5 m s^{-1} , that being an increase of 17 %. The position of this maximum is shifted to the east with increasing altitude, most likely resulting from the stripe patterns. At higher levels, the model overpredicts the measured wind speed by about 2 m s^{-1} .

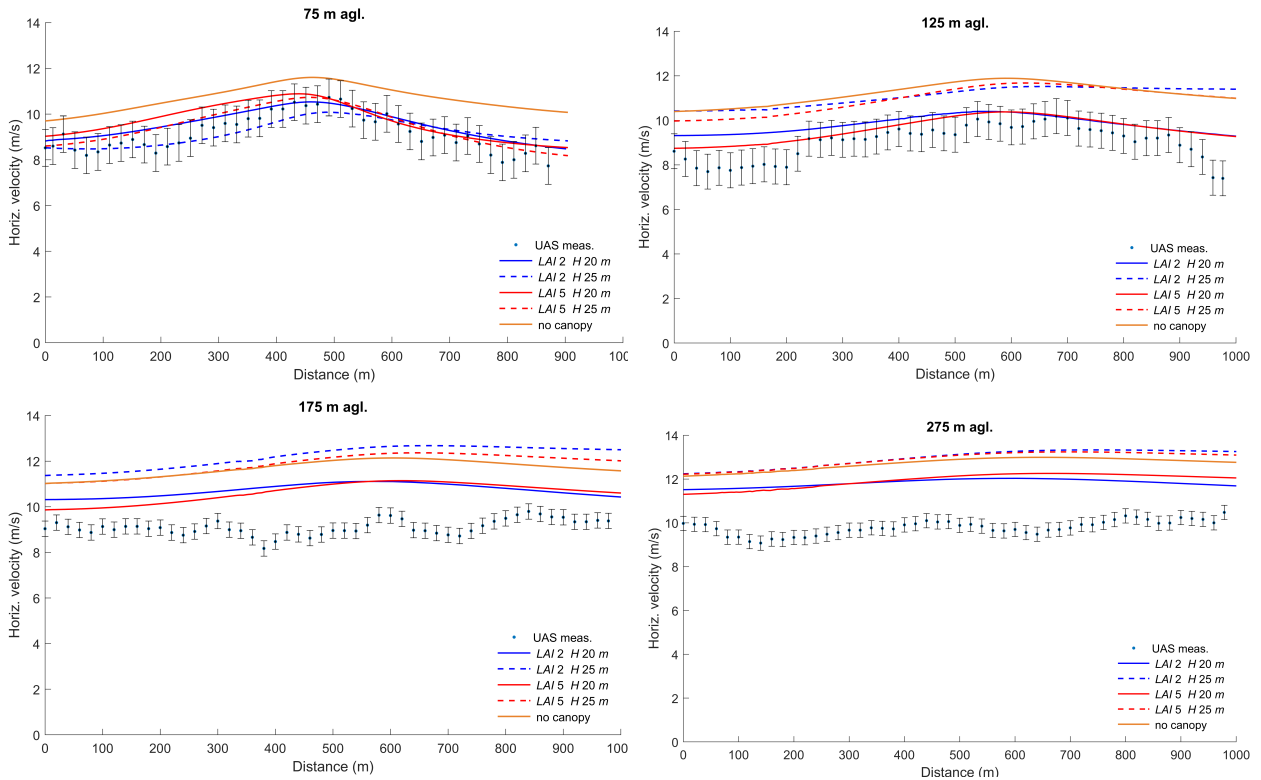


Figure 3.9: *Horizontal velocity at 75, 125, 175 and 275 m AGL. The dots are the UAS measurements with the error bars, corresponding to one standard deviation. The lines correspond to the simulation results and the colours represent the different values of LAI and forest height used.*

Although wind speed is the dominant characteristic for wind resource studies, other variables such as inclination angles (of the flow) need to be well characterised. Inclination angles are important for turbine siting as they have to be certified by the standards (IEC 61400-1 for example), where inflow angles are required to be within $\pm 8^\circ$ to ensure that the turbines will withstand the loads over their lifetime. The modelled and measured inclination angles shown in Figure 3.10 are in good agreement. The inclination angles are getting smaller with altitudes as the wind is less deflected by the orography. At 275 m, values near zero can be seen, indicating a flow that is horizontal. Positive inclination angles are visible in the first two-thirds of the flight path, with values reaching 10° at 75 m. This is due to the escarpment slope which creates updrafts in this area.

3.2. Publications 2 & 3: The wind flow in a rural area of complex topography

Results with different forest heights and foliage density LAI, as described in Table 3.1, are also included in Figure 3.9 and 3.10. It shows that the foliage density (blue vs. red line) has a minimal impact on the horizontal wind speed and inclination angle. Only the forest height (straight vs. dashed line) plays a role. This is reflected in the wind speed plots, where a forest height of 25 m always results in a positive velocity bias, except at 75 m.

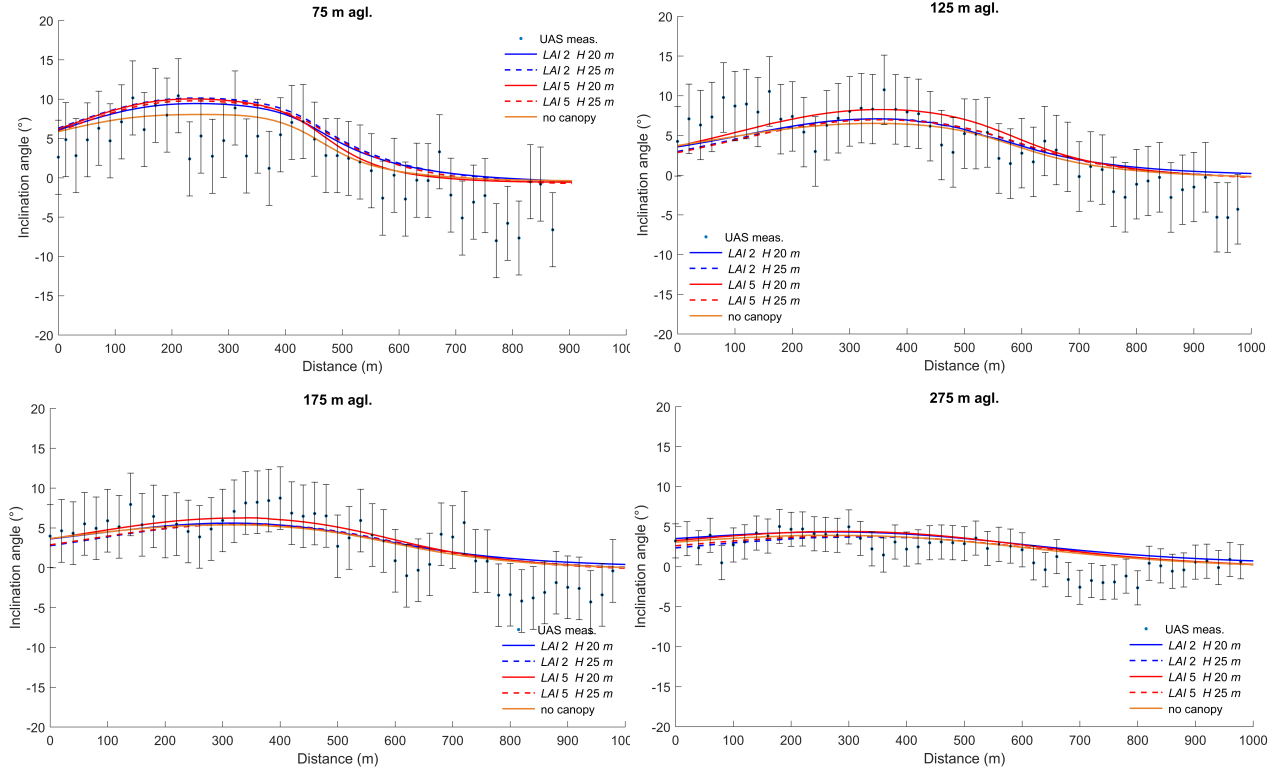


Figure 3.10: *Inclination angles at 75, 125, 175 and 275 m AGL. See also Figure 3.9.*

In Figure 3.11 and 3.12, simulated and measured horizontal wind speed and turbulent kinetic energy at three positions along the flight path are displayed. The first position P1 is located a few meters upstream the forest, the second one in the forested escarpment and the last position is located about 300 m downstream the escarpment (see Figure 3.7). As previously noted, the model overpredicts the wind speed at high altitudes. Figure 3.11 shows that the flow is decelerated before reaching the forest. A few meters further, at position 2, the profiles shows an inflexion point in the first meters above the ground due to the explicit modelling of the forest. This trend is not visible for the case without forest (orange line). Observed profiles further downstream of the escarpment, at position 3, indicate that the wind flow is still affected by the forested escarpment up to 300 m. The strong wind speed shear observed in the profiles indicates a high level of turbulence.

The turbulent kinetic energy profiles shown in Figure 3.12, reveals high values in the regions of strong vertical wind shear. At position 2, the maximum simulated value occurs between 20 and 25 m AGL, depending on the forest height. This corresponds to the top of the forest where a large portion of the turbulence is produced due to high shear stress. Downstream of the escarpment, at position 3, the maximum of the turbulent kinetic energy is carried to upper heights at around 50 m AGL. The position of this

3.2. Publications 2 & 3: The wind flow in a rural area of complex topography

maximum may be critical for the future wind turbines as it is located near the bottom of the rotor plane. The explicit modelling of the forest impacts also the turbulent kinetic energy values. At position 3, the values are increased by a factor of four by considering a LAI of 5. The MASC records a high turbulent kinetic energy of $2.4\text{m}^2\text{s}^{-2}$ at 75 m and shows a turbulence which decreases with increasing altitude, such as the model. The position of the maximum value measured by the MASC can not be determined due to lack of measurements under 75 m.

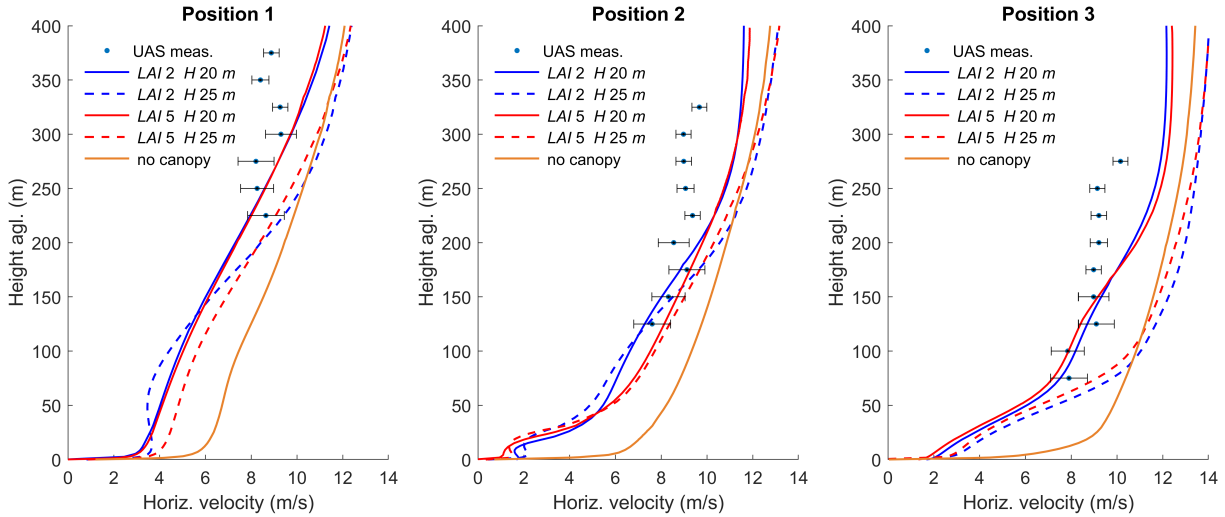


Figure 3.11: Vertical profiles of the horizontal wind speed at position 1, 2 and 3. See Figure 3.7 for the positioning.

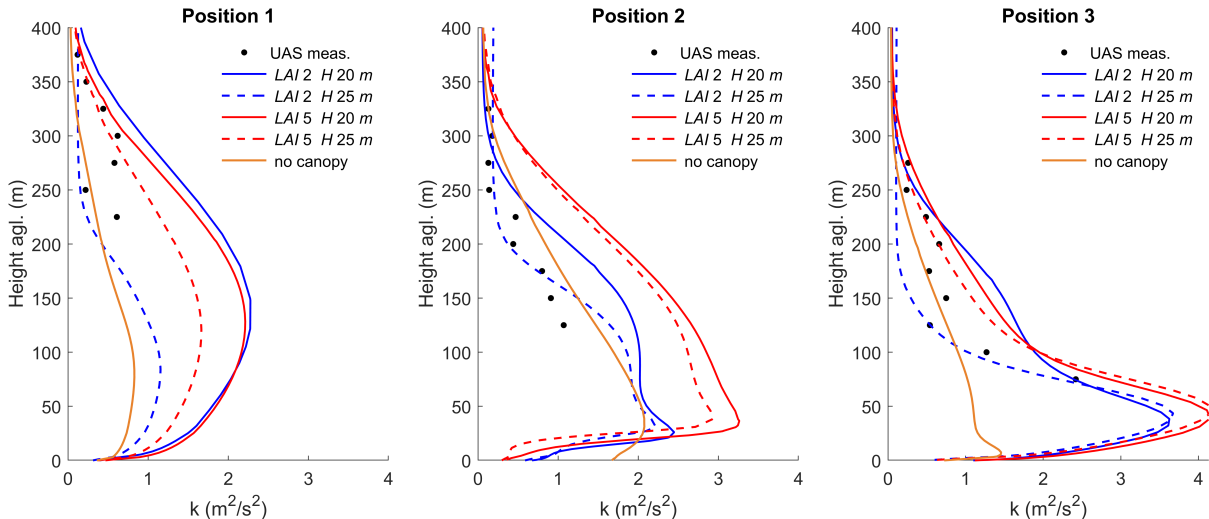


Figure 3.12: Vertical profiles of the turbulent kinetic energy at position 1, 2 and 3. See also Figure 3.11.

3.2.3 Coupling with a high resolution weather model

When considering diurnal variation of the ABL, the previous approach can not be applied. Transient simulations should be used to represent the time-varying vertical structure of the ABL. Transient data from a weather model WRF, with a high resolution, are used for this purpose. The mesoscale flow is simulated by the WINSSENT project partner KIT using five nested domains with increasingly resolution (Leukauf et al., 2019). The innermost nest, which delivers data to our model, has a horizontal grid resolution of 150 m and a first vertical grid point at 15 m. Velocity components, temperature and the ground heat fluxes are provided at 1 minute intervals. A computational domain of $10 \times 10 \times 2.5 \text{ km}^3$, centred at the test site is built for the CFD simulations. The bottom cells are 1.8 m high with a horizontal grid spacing of 10 m. No further nested domain is built as the resolution is considered fine enough. In this study, the forest is assumed to be 20 m height for the canopy model. Model validation is done by comparing the simulated fields with measurements from a meteorological tower and the MASC. A meteorological tower equipped with cup anemometers, hygrothermographs, barometers and wind vanes sampling at 20 Hz has been installed about 60 m west to the escarpment. An eddy-covariance (EC) station installed about 50 m west to the tower is providing near ground information. Two measurement campaigns with the MASC took place on 21 and 22 September 2018. Here again, the experimental flight configuration consisted of a vertical grid of racetracks with legs going back and forth (see Figure 3.13). The flights were conducted between 10:55 and 12:30 UTC and between 12:55 and 14:17 UTC for the first and second day, respectively. The lowest and highest flight levels were at 20 m and 200 m, respectively. This new flight experiment suits the need to measure at lower altitudes, near the ground, especially where strong vertical wind shears are to be expected.

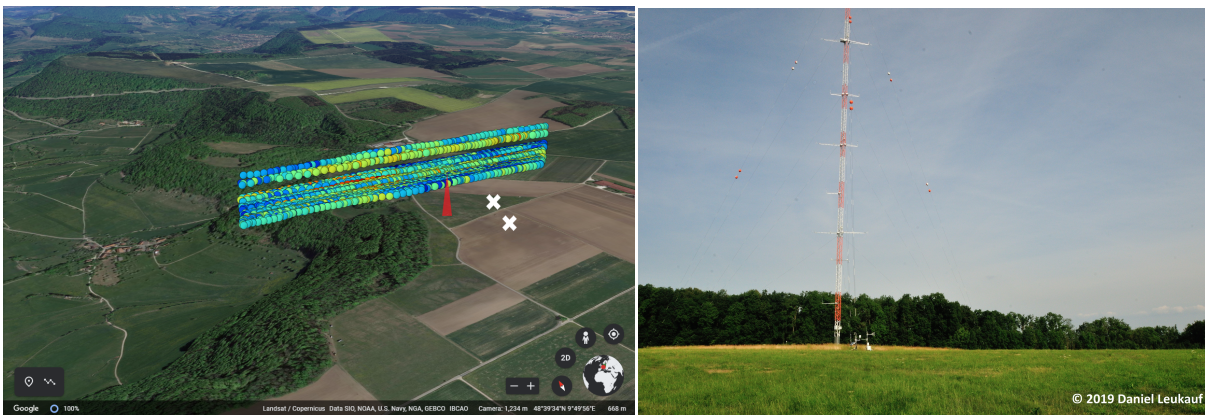


Figure 3.13: (a) The flight patterns performed over the two days in September 2018. The colors along the legs indicate the measured horizontal wind speed. The red triangle marks the position of the tower and the white dots the future wind turbines. (b) View of the tower taken from east-southeast. To the west the tower is a dense canopy. This picture shows that the lowest anemometer (10 m) is directly downslope of the forest.

3.2.3.1 Comparison with the Tower and EC Measurements

The measured and simulated 10-minutes averaged horizontal wind speed and wind direction at the tower are shown in Figures 3.14 and 3.15. Results for the first day (21 September 2018) are shown in the left panel, while the right one presents results for the second day (22 September 2018). A grey box corresponding to the times of the MASC flights is added to the figures. The measured wind speed on 21 September ranges from 7 m s^{-1} to 11 m s^{-1} at 86 m. The second day is dominated by calmer wind conditions, with wind speed values between 4 m s^{-1} to 7 m s^{-1} . A good agreement is achieved between the simulated and measured wind speed, except at 86 m for some specific times such as 11:25 and 12:20 UTC on 21 September 2018. The wind direction at 86 m shows a flow remaining consistent with winds blowing from the west. Wind directions recorded at the EC station are however showing high variability on the second day and may indicate a turbulent region with intermittent structures. Even the model shows, at the EC position, a fluctuating wind direction. The flow near the ground is more southerly orientated and suggest a directional veer.

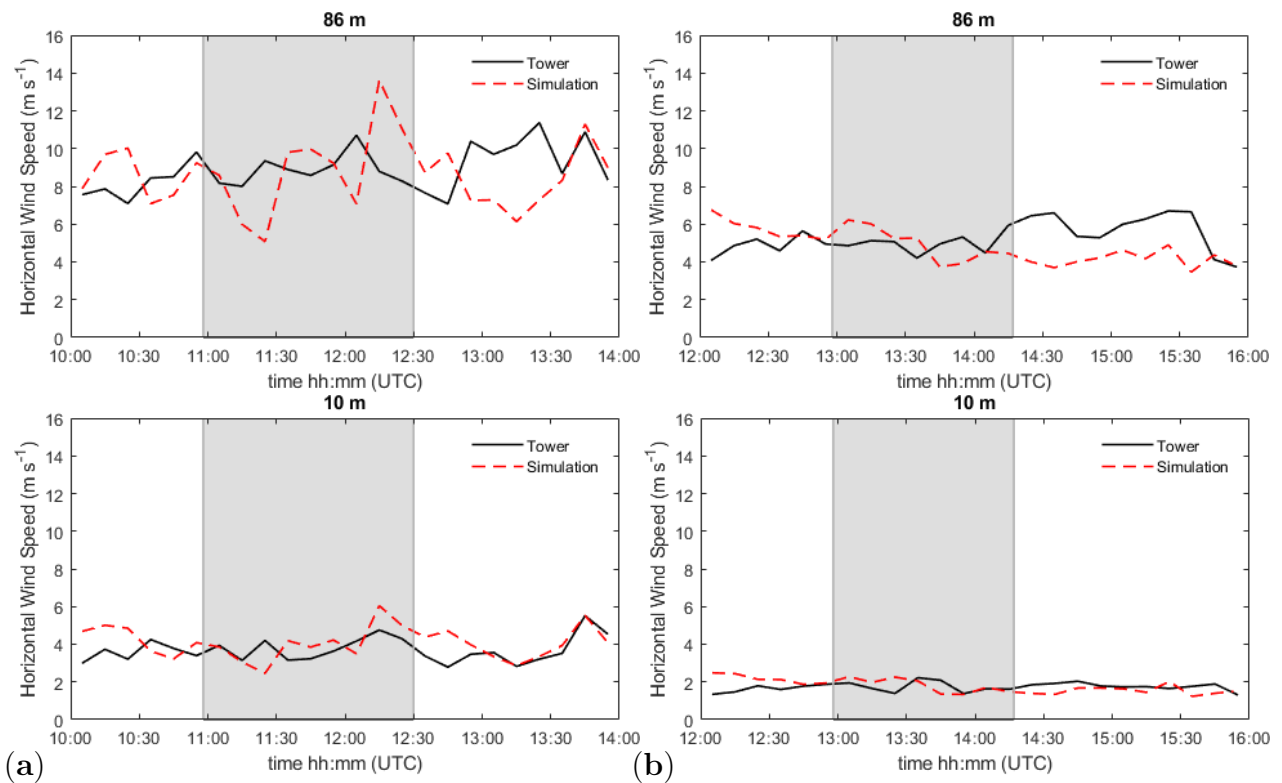


Figure 3.14: Time series of 10-min averages of horizontal wind speed at 86 m and 10 m AGL on 21 (a) and 22 (b) September. The time series for the simulation (red) and the tower observations (black) are shown. The grey box marks the time flight period.

3.2. Publications 2 & 3: The wind flow in a rural area of complex topography

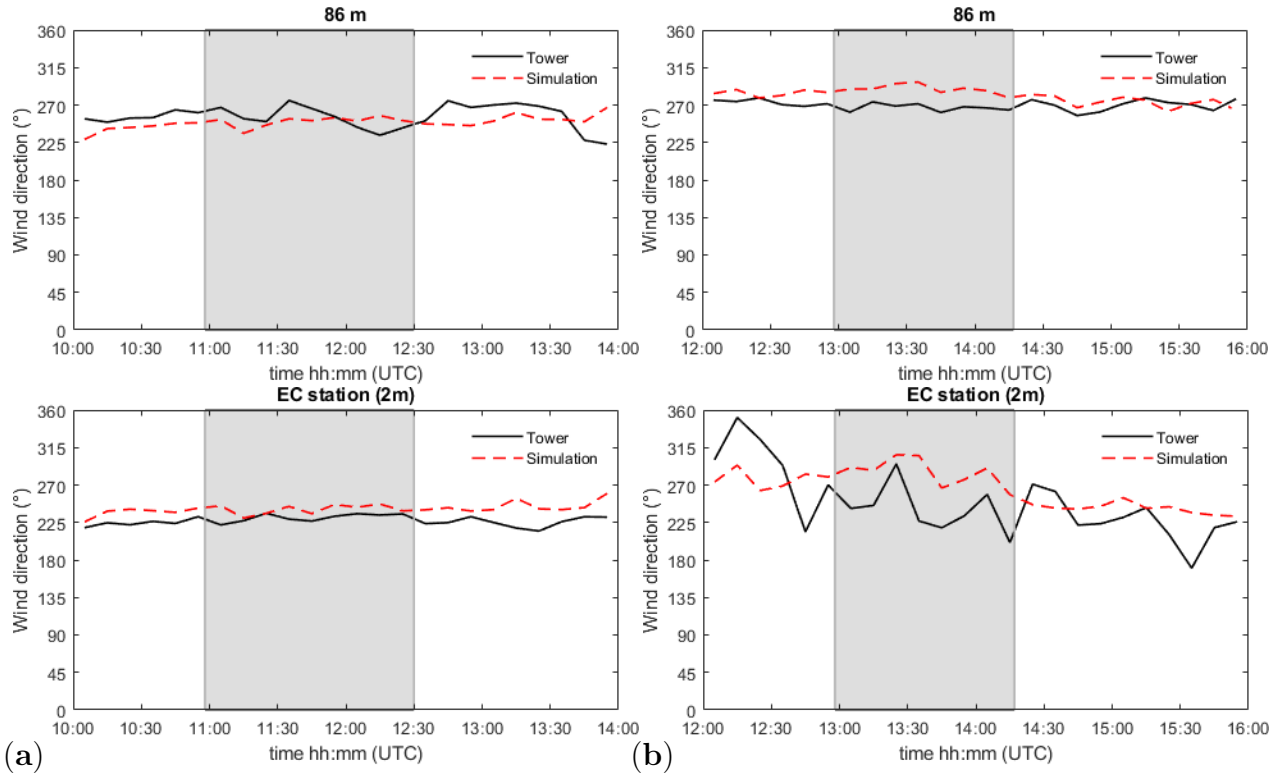


Figure 3.15: Time series of 10-min averages of wind direction at 86 m and 2 m AGL on 21 (a) and 22 (b) September. See also Figure 3.14.

The horizontal turbulence intensity (TI), defined as the ratio of standard deviation of horizontal wind speed to the mean wind speed, is shown in Figure 3.16. For both days, the 10 min-averaged TI values at 10 m remain above 40 %. The sensor at 86 m records values twice as small as the one at 10 m. This can be easily explained by the position of the tower which is located about 60 m west to the escarpment. For a westerly flow, as in the present study, the 10 m sensor is situated in the forest wake. A good agreement between the simulated and measured TI is achieved at 86 m. However, too small values for the TI are predicted at 10 m. The $k-\varepsilon$ model is known to produce low turbulence levels, specially close to the canopy region (Segalini et al., 2016), and thus could be responsible for the underestimation.

3.2.3.2 Comparison with the UAS Measurements

For the validation of the model with the airborne observations, a real time strategy is adopted. Probes are placed in the model at the same geographic coordinates where the MASC is flying. For a direct comparison of the simulation results and the UAS measurements, the probes are then selected in order to fit the flight time.

Figure 3.17 shows the measured and simulated horizontal wind speed along the performed flight legs. The geometry of the ground (grey) and the position of the modelled forest (green) have been added for visual purposes. For 21 September, results at 20, 50, 80 and 200 m AGL are shown, while altitudes of 20, 50, 70, 130 and 190 m AGL were chosen for the second day. The scale for the velocity is purposely different for both days in order to avoid flat profiles for 22 September. On both days, a similar flow structure is visible: right after the escarpment, velocities increase due to the updrafts generated by the orography. Figure 3.17 shows that the simulated wind speeds agree very well

3.2. Publications 2 & 3: The wind flow in a rural area of complex topography

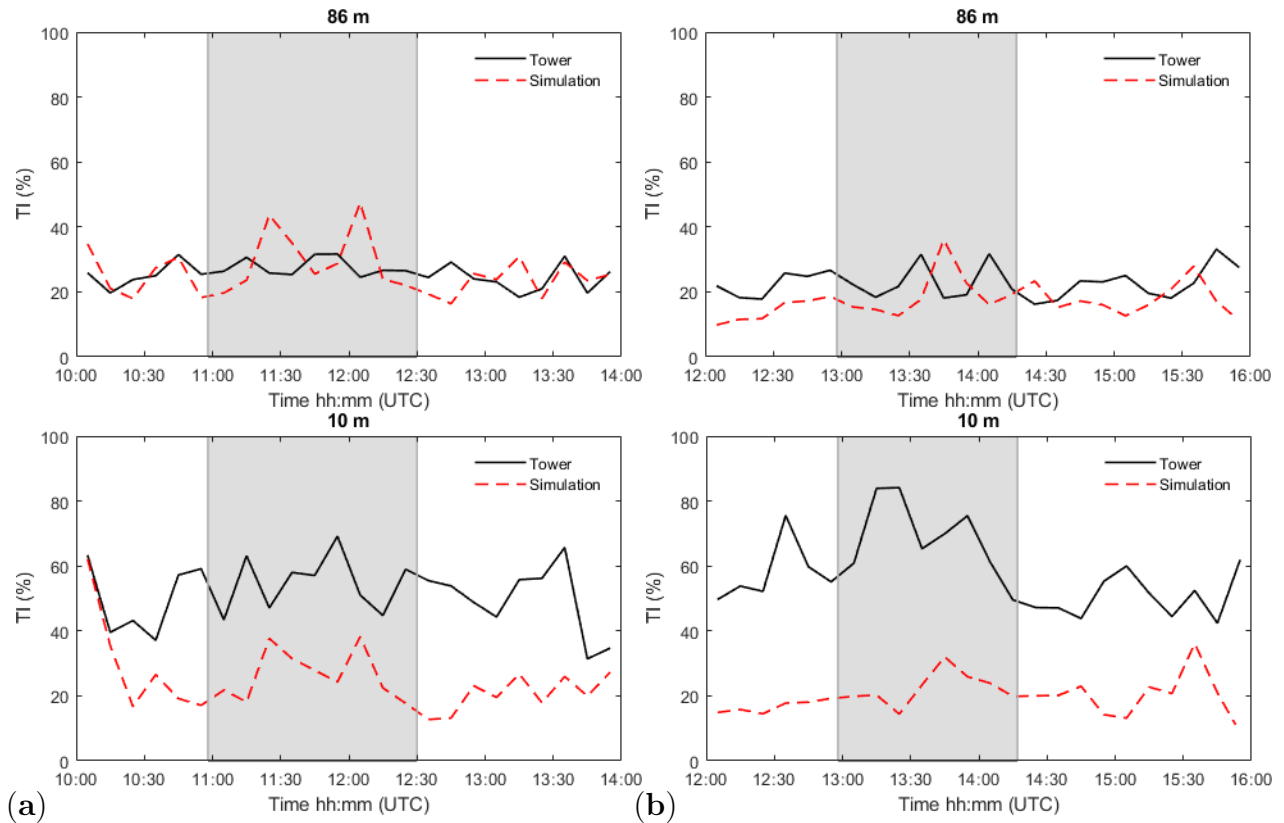


Figure 3.16: Time series of 10-min averages of horizontal turbulence intensity at 86 m and 10 m AGL on 21 (a) and 22 (b) September. See also Figure 3.14.

with the observed values except at 200 m on 21 September, where an overprediction is visible.

Inclination angles from the model and the airborne measurements are shown in Figure 3.18. Positive angles up to 15° , numerically, and 20° , experimentally, are observed above and behind the escarpment. The flow is dominated by upward movements even at upper levels. Inclination angles at 200 and 190 m are becoming for both days small but still differs from 0° . It indicates that the forested escarpment influences the flow even at the highest altitudes. On 21 September, negative modelled and measured inclination angles are visible at the bottom of the escarpment, revealing a descending motion. It means that the wind flow, before reaching the escarpment is already disturbed. Before reaching the test site, a wind blowing from the west will pass over a small hill located 1.5 km west to the escarpment (see Figure 3.5) and a recirculation and thus negative inclination angles can appear. This hypothesis is checked by plotting the simulated vertical wind speeds in a cross-section. The values are averaged over the entire flight periods for both days, i.e., 95 and 82 minutes. A large recirculation zone in the lee of the hill is visible in Figure 3.19 and corroborates the hypothesis.

3.2. Publications 2 & 3: The wind flow in a rural area of complex topography

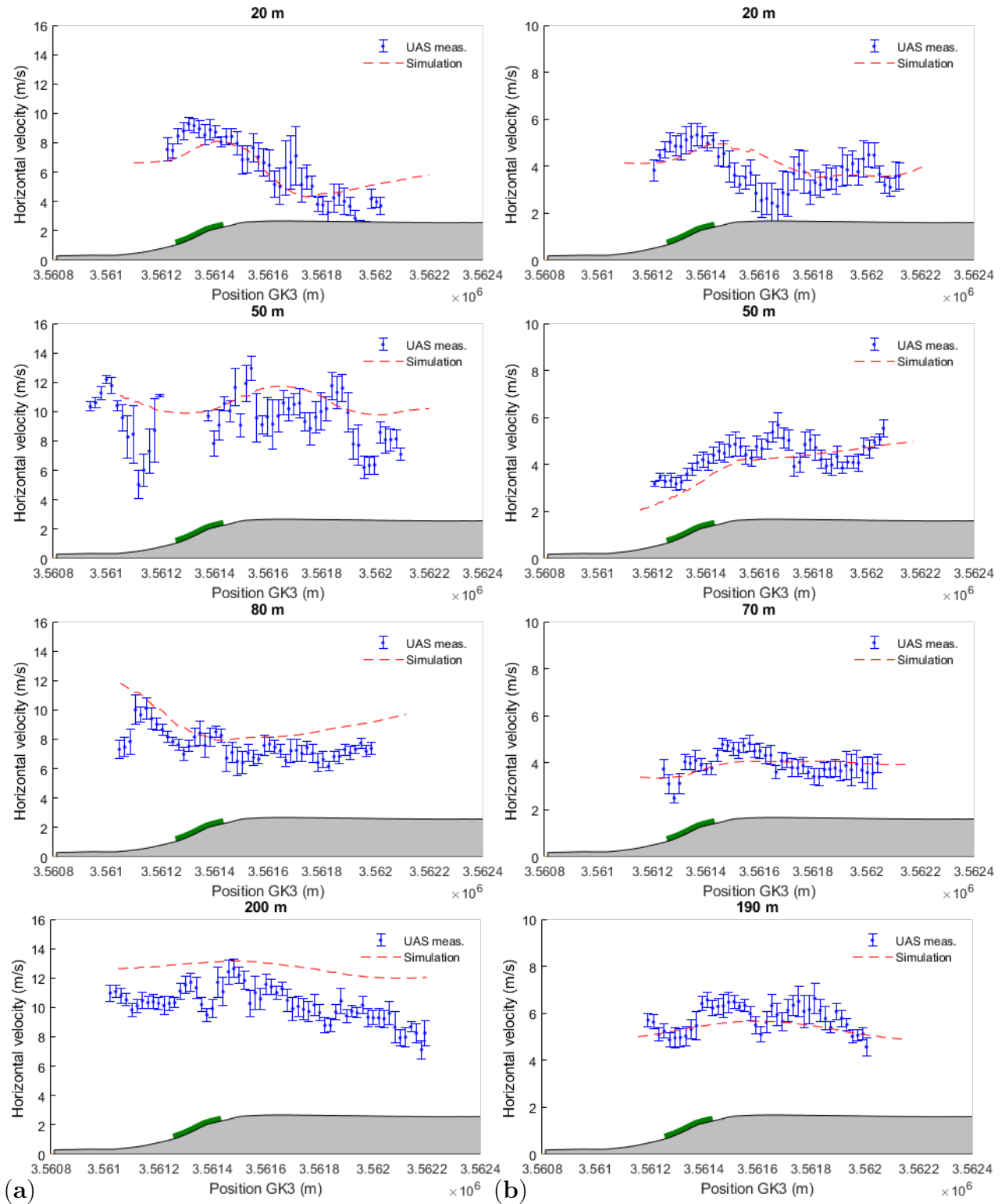


Figure 3.17: Horizontal velocity on 21 (a) and 22 (b) September at different altitudes along the UAS's flight path. The blue dots are the UAS measurements and the red dashed lines are the simulation results. Error bars, corresponding to one standard deviation, are inserted for the MASC measurements. The green block represents the modelled forest.

3.2. Publications 2 & 3: The wind flow in a rural area of complex topography

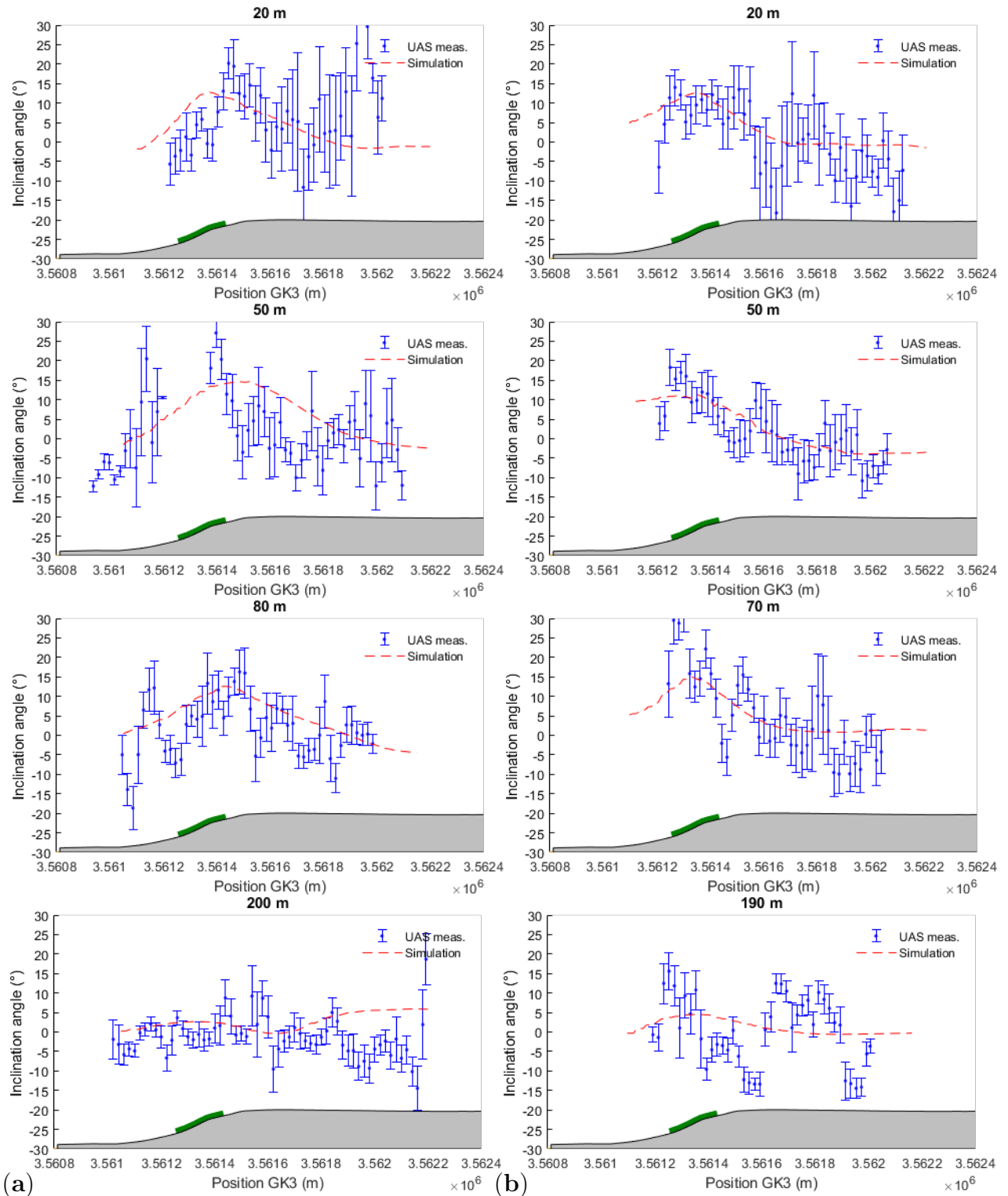


Figure 3.18: Inclination angles on 21 (a) and 22 (b) September at different altitudes along the UAS' flight path. See also Figure 3.17.

3.2. Publications 2 & 3: The wind flow in a rural area of complex topography

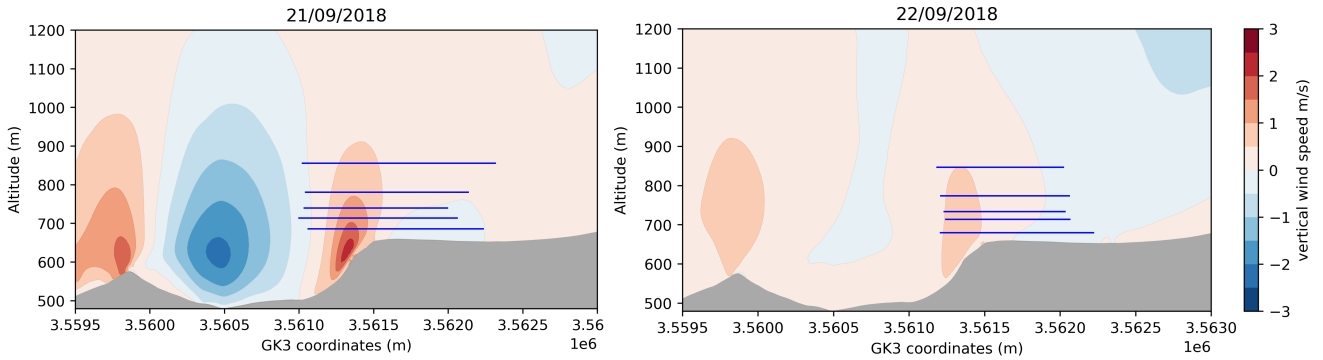


Figure 3.19: *Cross-section of simulated vertical wind speed averaged over the whole flight duration on 21 (a) and 22 (b) September. The blue lines correspond to the legs plotted in Figures 3.17 and 3.18 performed by the MASC.*

Additionally the wind direction over the legs is shown in Figure 3.20. It shows simulated wind direction values increasing with decreasing height, in agreement with the observed values. On 21 September, a wind rotation up to 50° between 20 and 200 m is visible, indicating a directional backing. The same behaviour is observed on the second day, with a wind turning by 20° between 20 and 50 m. Error bars, corresponding to one standard deviation, were inserted for the airborne observations in the Figures 3.17, 3.19 and 3.20. The standard deviation of the horizontal wind speed is a measure of its variability and thus reflect the turbulence intensity. The plots shows that the largest deviations occurs at heights near to the ground, specially right after the escarpment. This can be explained by an increased turbulence near the ground and in the forest wake, as already observed at the tower (Figure 3.16).

3.2. Publications 2 & 3: The wind flow in a rural area of complex topography

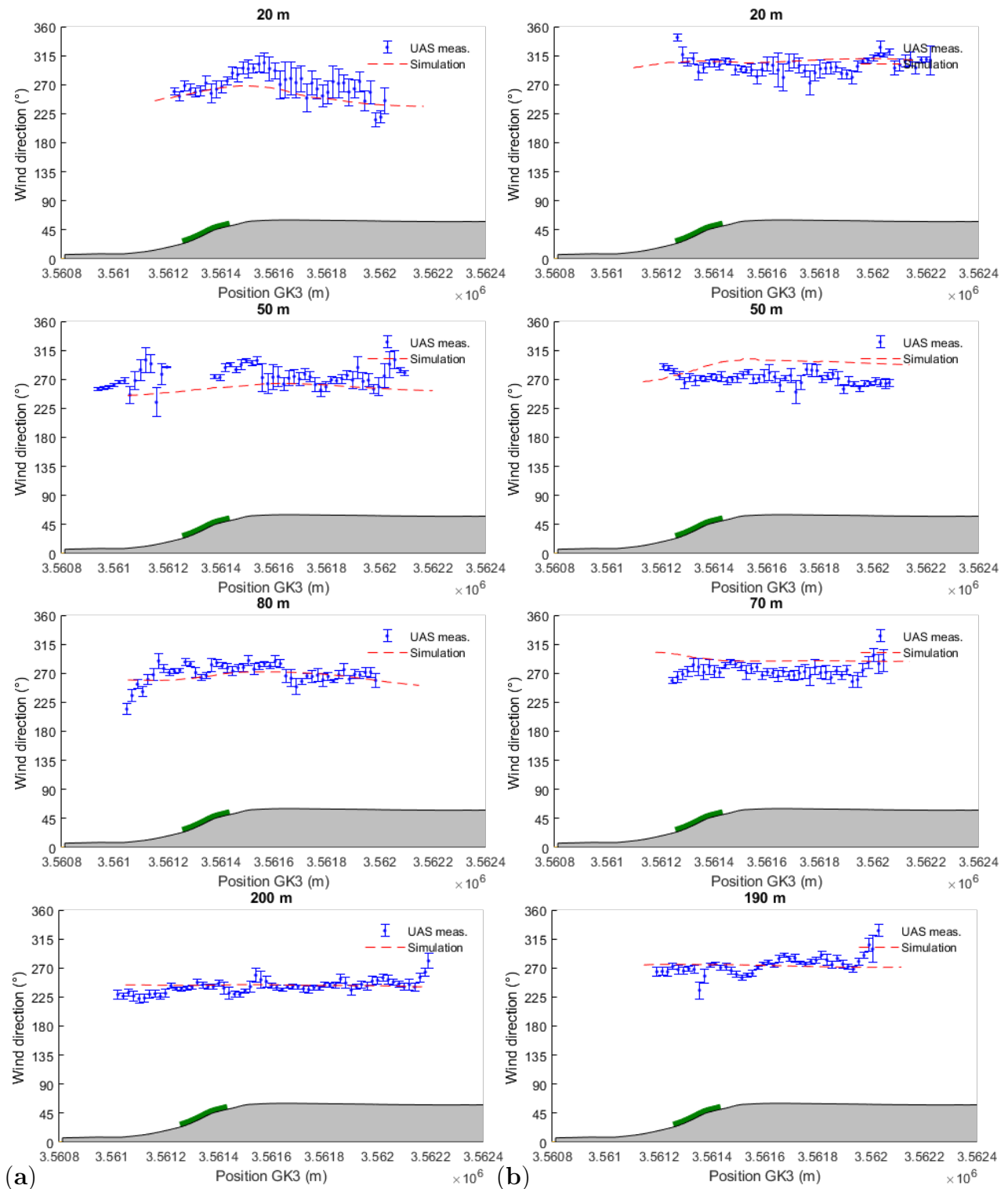


Figure 3.20: Wind direction on 21 (a) and 22 (b) September at different altitudes along the UAS' flight path. See also Figure 3.17.

3.2.3.3 Stability considerations

The potential temperature evolution over the entire two days computed from the tower is presented in Figure 3.21. The flight time periods are indicated by a grey area. On 21 September, the tower recorded small vertical potential temperature gradients (also known as potential temperature lapse rate $\Delta\theta/\Delta z$) during the flight campaign, corresponding to near-neutral conditions. During the second measurement campaign, a negative lapse rate (calculated from 2 and 96 m) of -1.8 K/100 m is measured and indicates the occurrence of an unstable atmosphere. The potential temperature at 16:00 UTC on 21 September drops by about 10 K due to a passing cold front.

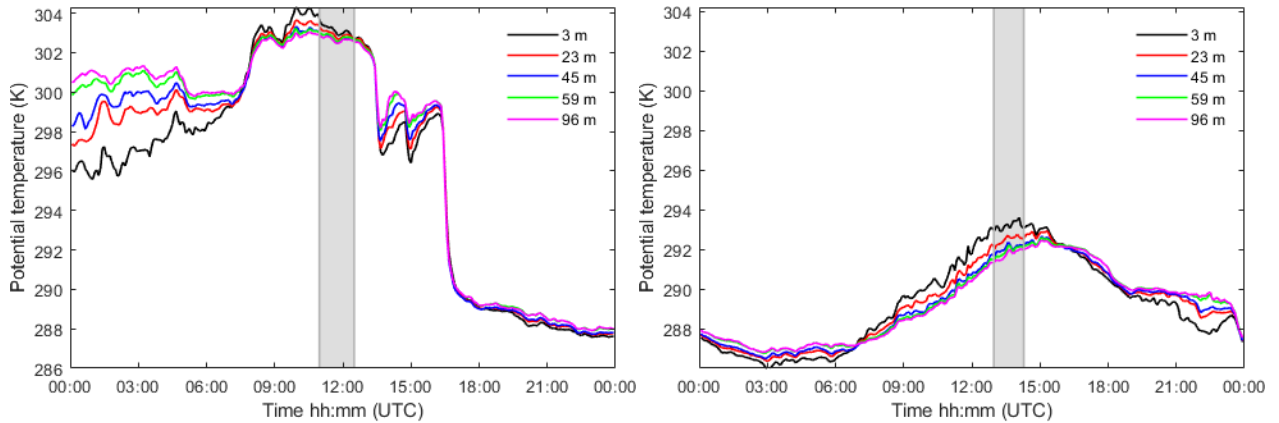


Figure 3.21: *Time series of 10-min averages of potential temperature on 21 (a) and 22 (b) September. The grey box marks the time flight periods.*

Vertical potential temperature differences profiles from the simulation and measurements for three regions are shown in Figure 3.22. Differences and not absolute values are shown since the potential temperatures were different for both days. The first position is located above the escarpment, the second one is centred around the tower while the last one represent the last third of the flight path. For both days, Figure 3.22 shows a decreasing potential temperature up to 50 m on the first day and 100 m for the second one. However, the lapse rate is stronger on 22 September. On that day, the tower shows a potential temperature which is decreased by 1.5 K in the lowest 100 m, indicating a superadiabatic layer. The airborne measurements shows a temperature which decreases by 0.5 K between 20 and 50 m. Although the MASC and the tower use different measurement technologies, associated to different spatial and temporal resolutions, the agreement between both system is good. The model produces similar shape profile for the potential temperature differences. Near the ground, the differences are however underestimated and may be the result of a low vertical resolution near the ground but also the surface heat fluxes from the mesoscale model, which are underestimated around mid-day, i.e., during the measurement campaigns.

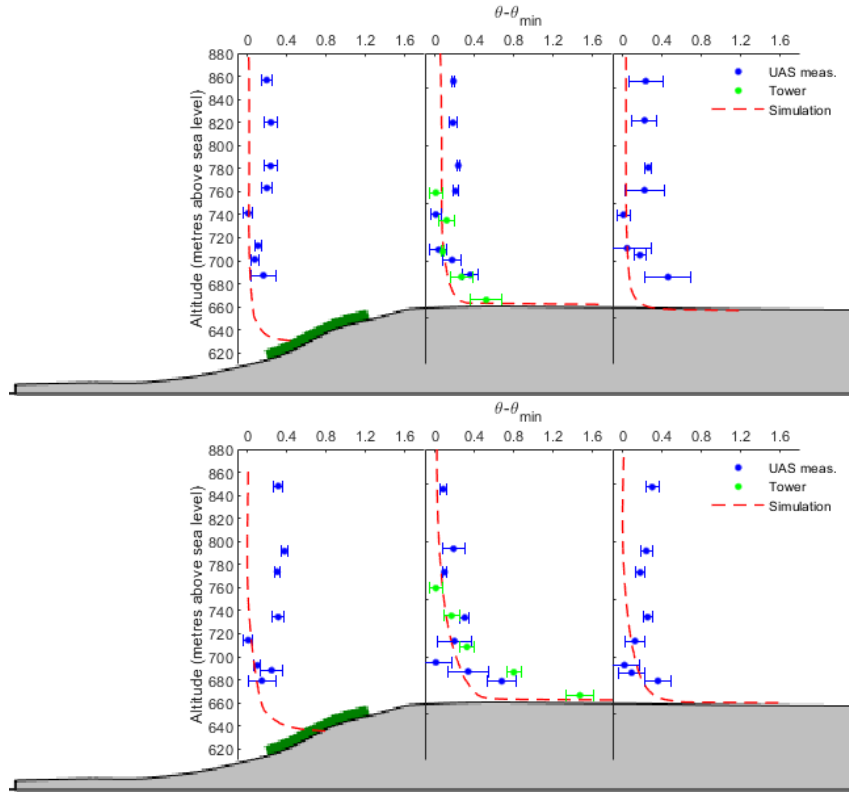


Figure 3.22: Vertical profiles of potential temperature differences (potential temperature minus its minimum value) from the MASC (blue dots), the tower (green dots) and the simulation (red lines) over, behind and further downstream the escarpment on 21 (top) and 22 (bottom) September.

Another usual measure of the local stratification, namely the bulk Richardson number, is investigated. The bulk Richardson number Ri_B (Stull, 1988), calculated from the wind and temperature measurement at two levels, is defined as:

$$Ri_B = \frac{g (\theta_u - \theta_l)(z_u - z_l)}{T_a (U_u - U_l)^2} \quad (3.13)$$

where T_a is the average air temperature of the layer, θ_l and θ_u are the potential temperature at the lower z_l and upper z_u level. U represents the horizontal wind speed and $g = 9.81 \text{ m s}^{-2}$ is the gravitational acceleration. The critical bulk Richardson number $Ri_{B,crit}$ values are still under debate in the scientific community but typically, a value of 0.25 for small Δz can be found in the literature (Miles, 1961; Zoumakis and Kelessis, 1991). The production of turbulence ceases to occur when $Ri_{B,crit}$ exceeds 0.25, while for smaller values the flow is dynamically unstable and turbulence is likely to occur.

The diurnal pattern of the computed Ri_B , computed from the tower measurements at 45 and 100 m, over the two days is presented in Figure 3.23. The plots clearly show that, during the flight time (grey box) a near neutral state on the first day is dominating, while the atmosphere is in an unstable state on the second day. The bulk Richardson number from the MASC and the model are computed using three levels: the lowest flown altitude, a medium level and the highest leg. The distribution of the computed

3.2. Publications 2 & 3: The wind flow in a rural area of complex topography

bulk Richardson number is shown in Figure 3.24. The computed Ri_B values using the low and medium height show a drop right after the escarpment and evidence a critical region dominated by shear instabilities. The negative Ri_B values on both days reveals thermodynamic instabilities up to 300 m downstream of the escarpment. In accordance with simulation results, the MASC Ri_B values computed from the mid and upper levels are getting almost equal to zero on 21 September due to a large vertical wind shear. This mechanical shear is also visible on the second day, with Ri_B values remaining negative (unstable layer) but approaching zero. The atmospheric stratification on the second day is not well represented near the ground, as already observed in the vertical potential temperature differences from Figure 3.22.

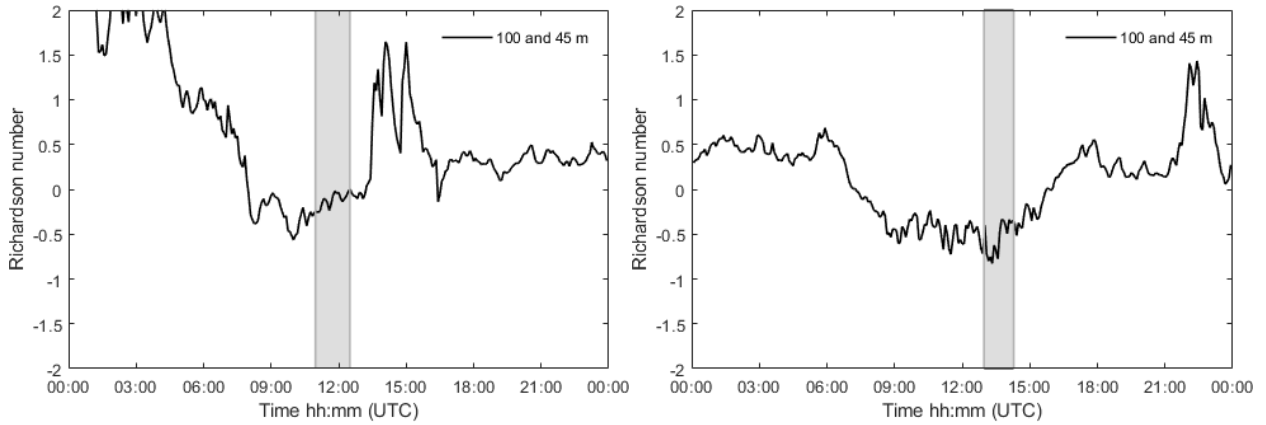


Figure 3.23: Time series of 10-min averages of Ri_B between 45 and 100 m on 21 (a) and 22 (b) September. The grey box marks the time flight periods.

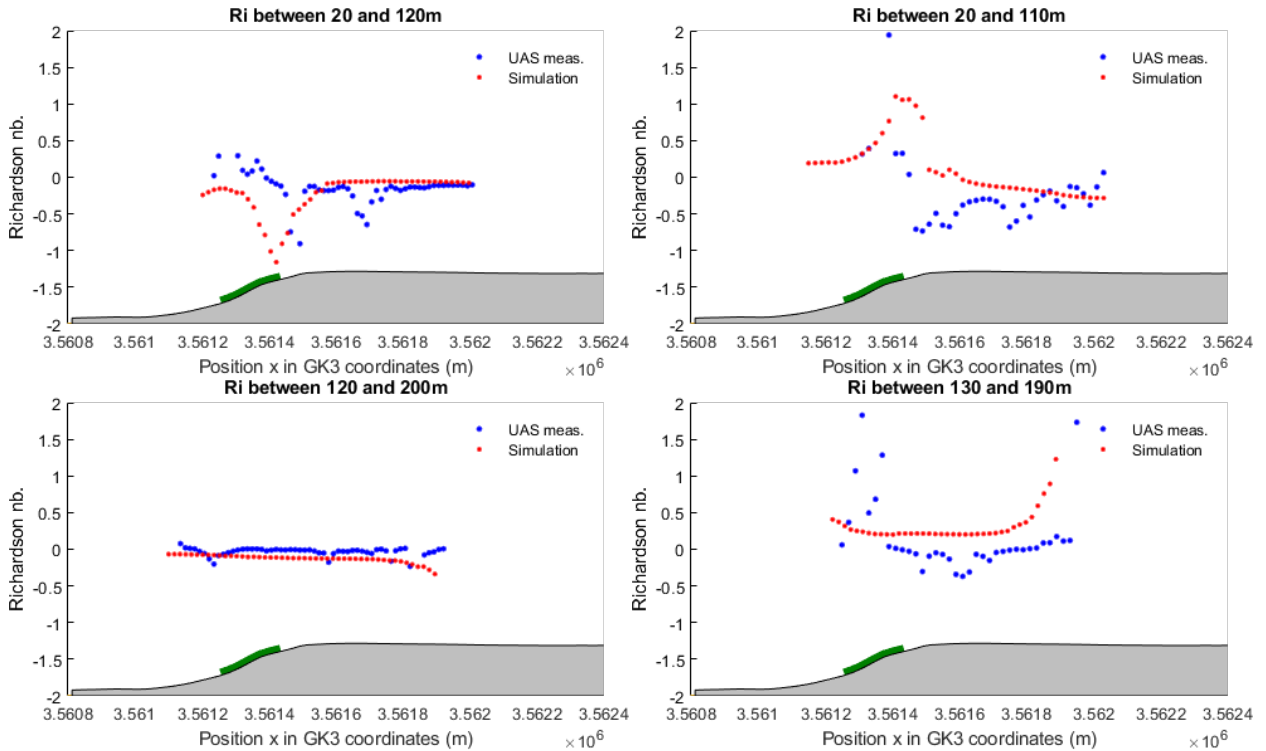


Figure 3.24: Bulk Richardson number computed from the UAS measurements on 21 (left) and 22 (right) September at different altitudes along the UAS's flight path using 20 m horizontal intervals. The green block represents the modelled forest.

Discussion and outlook

This thesis presents the development of a numerical modelling framework for characterizing the wind flow in complex terrains. Analysis of the flow phenomena at two complex sites based on a RANS model are presented. Data from field campaigns are used for the model validation.

The first study investigates the wind flow in a built-up environment, at the Morgenstelle campus site from the University of Tübingen, Germany. The site is characterized by several rectangular shaped buildings orientated against the prevailing wind direction in the area, that is 240° . West to the buildings a large forested area is present and lying in the inflow region. To mimic the effect of the forest on the flow, a canopy model is implemented in the numerical model together with a logarithmic wind profile for the inflow condition. The simulation with and without forest are performed and compared with an experiment setup consisting of six stations, equipped with ultrasonic anemometers, and spread over the campus. Simulation results with a forest show a significant improvement in terms of wind speed when compared to the non-forested case. Despite the drastic simplification of the ground by assuming a flat terrain, the study shows that the forest plays a dominant role. The large spread observed in the experimental data was no further analysed but it will be interesting to sort the wind data from the network stations according to meteorological seasons or the stability, for instance. Since then, the campus site raised interest, specially with the graduate program called ‘Windy Cities’ (<http://windycities.de/>) from the University of Stuttgart together with the Hochschule of Esslingen and Stuttgart. This interdisciplinary graduate training group aims at investigating the economic use of small wind turbines in urban areas. Further ongoing work is in progress by including a vertical axis wind turbine in the simulation (Zamre et al., 2020) or using real forest heights from Laser scan data for the canopy model (von der Grün et al., 2020).

The second study focuses on a complex site located in the Swabian Alb in Southern Germany. The site is characterized by a vegetated sloping escarpment up to 200 m. Here again, a canopy model is used to represent the forested area. The orography is known to influence local flows, that is why, a digital elevation model with a spatial resolution of 5 m is used for the terrain representation. The land cover is simplified by defining three categories (roughness length): forest, ground and city. The URANS approach with a $k - \epsilon$ model for the turbulence closure is chosen. The model has been modified to adapt boundary layer flows by including buoyancy, thermal effect for example. An experimental campaign conducted on 27 March 2015 with the MASC serves for the model validation. The CFD model is coupled to the COSMO-DE weather model. Because of the low resolution of the COSMO-DE model, two nested domains were built

for the CFD simulation. Despite the low resolution of the mesoscale model, the nesting strategy is able to capture flow patterns such as updraft, wind deceleration or high turbulent intensities at the site. Generally, a good agreement is found between the model and the airborne measurement except for the highest level, where the model tends to overestimate the wind speed. It was found that the inclusion of explicit canopy increases the turbulent kinetic energy values by up to a factor of four. The MASC also records high turbulence intensities at the lowest flight level, that is 75 m. The sensitivity study to the height and the foliage of the forest shows that the forest height has a dominant impact on the horizontal wind speed and inclination angles. The foliage is only affecting the turbulent kinetic energy values. A denser forest (LAI value of 5) generates higher levels of turbulence.

In a second step, the CFD model is coupled to a weather model (WRF) with higher vertical and horizontal resolutions. The transient approach is tested by using time-dependent boundary conditions deviated from the weather model and provided at 1 minute intervals. A transport equation for potential temperature is added to the set of our equations. Two measurement campaigns performed by the MASC were conducted adjacent to a 100 m meteorological tower. Numerical validation is performed by ‘following’ the MASC coordinates during the flight campaign (around 90 minutes). In this way, no time averaging is needed and changes related to the transient flow are considered. This approach shows very good agreement between the simulation and experimental results. All local features induced by the orography are captured. The high horizontal turbulent intensities recorded by the tower at 10 m, due to the forest wake, were not captured by the model. This issue should be further investigated, by comparing with another turbulence and canopy model. The second day, dominated by a more convective surface layer is not well simulated in terms of potential temperature. A superadiabatic layer next to the ground is observed by the tower and the MASC. The simulation tends to underestimate the potential temperature decrease near the ground. It can be attributed to the surface heat fluxes provided by the WRF model and a lack of grid resolution.

Future research should include a better description of the surface heat fluxes. Due to the heterogeneous land cover in the test site region, it will be necessary to add more EC stations to measure surface fluxes for validation. Using UAS for providing high temporal and spatial resolution surface temperature or fluxes can also be considered. Such experience has been done in the agriculture domain, where the thermal land surface measurement from UAS, were used for energy balance models inputs (boundary). Hoffmann et al. (2016) used a UAS to provide surface energy fluxes for their model during cloudy and overcast weather conditions as an alternative to satellites. Satellite thermal data can only be obtain in clear-sky conditions.

Another possibility to enhance the simulation results is the data assimilation in the model. In a recent study, an improved prediction of wind speed and direction is achieved by assimilating data collected by a UAS during the LAPSE-RATE Experiment in a WRF model (Boer et al., 2020). Assimilating data from the tower can also be explored.

Bibliography

- Al-Quraan, A., Stathopoulos, T., and Pillay, P. (2016). Comparison of wind tunnel and on site measurements for urban wind energy estimation of potential yield. *Journal of Wind Engineering and Industrial Aerodynamics*, 158:1–10.
- Altstädter, B., Platis, A., Wehner, B., Scholtz, A., Wildmann, N., Hermann, M., Kaethner, R., Baars, H., Bange, J., and Lampert, A. (2015). ALADINA – an unmanned research aircraft for observing vertical and horizontal distributions of ultrafine particles within the atmospheric boundary layer. *Atmospheric Measurement Techniques*, 8(4):1627–1639.
- Apsley, D. and Castro, I. P. (1997). A limited-length-scale k-epsilon model for the neutral and stably-stratified atmospheric boundary layer. *Boundary-Layer Meteorology*, 83(1):75–98.
- Bailey, B. H., McDonald, S. L., Bernadett, D. W., Markus, M. J., and Elsholz, K. V. (1997). Wind resource assessment handbook: Fundamentals for conducting a successful monitoring program. Technical report.
- Balsley, B. B., Lawrence, D. A., Fritts, D. C., Wang, L., Wan, K., and Werne, J. (2018). Fine Structure, Instabilities, and Turbulence in the Lower Atmosphere: High-Resolution In Situ Slant-Path Measurements with the DataHawk UAV and Comparisons with Numerical Modeling. *Journal of Atmospheric and Oceanic Technology*, 35(3):619–642.
- Baniotopoulos, C. and Rebelo, C. (2015). *Trends and Challenges for Wind Energy Harvesting (Proceedings of the WINERCOST Workshop, 30-31 March 2015)*. University of Coimbra.
- Bauweraerts, P. and Meyers, J. (2021). Reconstruction of turbulent flow fields from lidar measurements based on large-eddy simulation. *Journal of Fluid Mechanics*, 906:A17.
- Belcher, S. E., Harman, I. N., and Finnigan, J. J. (2012). The Wind in the Willows: Flows in Forest Canopies in Complex Terrain. *Annual Review of Fluid Mechanics*, 44(1):479–504.
- Blocken, B. (2018). LES over RANS in building simulation for outdoor and indoor applications: A foregone conclusion? *Building Simulation*, 11(5):821–870.
- Boer, G. d., Diehl, C., Jacob, J., Houston, A., Smith, S. W., Chilson, P., Schmale, D. G., Intrieri, J., Pinto, J., Elston, J., Brus, D., Kemppinen, O., Clark, A., Lawrence, D., Bailey, S. C. C., Sama, M. P., Frazier, A., Crick, C., Natalie, V., Pillar-Little, E., Klein, P., Waugh, S., Lundquist, J. K., Barbieri, L., Kral, S. T., Jensen, A. A.,

- Dixon, C., Borenstein, S., Hesselius, D., Human, K., Hall, P., Argrow, B., Thornberry, T., Wright, R., and Kelly, J. T. (2020). Development of Community, Capabilities, and Understanding through Unmanned Aircraft-Based Atmospheric Research: The LAPSE-RATE Campaign. *Bulletin of the American Meteorological Society*, 101(5):E684–E699.
- Båserud, L., Flügge, M., Bhandari, A., and Reuder, J. (2014). Characterization of the sumo turbulence measurement system for wind turbine wake assessment. *Energy Procedia*, 53:173 – 183.
- Carta, J., Velázquez, S., and Cabrera Santana, P. (2013). A review of measure-correlate-predict (MCP) methods used to estimate long-term wind characteristics at a target site. *Renewable and Sustainable Energy Reviews*, 27:362–400.
- Castro, F. A., Santos, C. S., and Costa, J. C. L. d. (2015). One-way mesoscale–microscale coupling for the simulation of atmospheric flows over complex terrain. *Wind Energy*, 18(7):1251–1272.
- Cescatti, A. and Marcolla, B. (2004). Drag coefficient and turbulence intensity in conifer canopies. *Agricultural and Forest Meteorology*, 121(3):197–206.
- Cheng, W. Y., Liu, Y., Liu, Y., Zhang, Y., Mahoney, W. P., and Warner, T. T. (2013). The impact of model physics on numerical wind forecasts. *Renewable Energy*, 55:347–356.
- Chow, F. K., Schär, C., Ban, N., Lundquist, K. A., Schlemmer, L., and Shi, X. (2019). Crossing Multiple Gray Zones in the Transition from Mesoscale to Microscale Simulation over Complex Terrain. *Atmosphere*, 10(5):274.
- Cione, J. J., Kalina, E. A., Uhlhorn, E. W., Farber, A. M., and Damiano, B. (2016). Coyote unmanned aircraft system observations in Hurricane Edouard (2014). *Earth and Space Science*, 3(9):370–380.
- Clifton, A., Clive, P., Gottschall, J., Schlipf, D., Simley, E., Simmons, L., Stein, D., Trabucchi, D., Vasiljevic, N., and Wuerth, I. (2018). IEA wind task 32: Wind lidar identifying and mitigating barriers to the adoption of wind lidar. *Remote Sensing*, 10:22.
- Cook, J., Oreskes, N., Doran, P. T., Anderegg, W. R. L., Verheggen, B., Maibach, E. W., Carlton, J. S., Lewandowsky, S., Skuce, A. G., Green, S. A., Nuccitelli, D., Jacobs, P., Richardson, M., Winkler, B., Painting, R., and Rice, K. (2016). Consensus on consensus: a synthesis of consensus estimates on human-caused global warming. *Environmental Research Letters*, 11:7.
- Detering, H. W. and Etling, D. (1985). Application of the e-epsilon turbulence model to the atmospheric boundary layer. *Boundary-Layer Meteorology*, 33(2):113–133.
- Deutsche Institut für Normung, DIN (2019). *Windenergieanlagen - Teil 1: Auslegungsanforderungen (IEC 61400-1:2019)*. Deutsche Institut für Normung. VDE Verlag.

- Doms, G. and Baldauf, M. (2018). A Description of the Nonhydrostatic Regional COSMO-Model. *Deutscher Wetterdienst*, page 167.
- Drew, D. R., Barlow, J. F., and Cockerill, T. T. (2013). Estimating the potential yield of small wind turbines in urban areas: A case study for Greater London, UK. *Journal of Wind Engineering and Industrial Aerodynamics*, 115:104–111.
- Dudhia, J. (1993). A Nonhydrostatic Version of the Penn State–NCAR Mesoscale Model: Validation Tests and Simulation of an Atlantic Cyclone and Cold Front. *Monthly Weather Review*, 121(5):1493–1513.
- Duraisamy, V. J., Dupont, E., and Carissimo, B. (2014). Downscaling wind energy resource from mesoscale to microscale model and data assimilating field measurements. *Journal of Physics: Conference Series*, 555:012031.
- Duran, P., Meissner, C., and Casso, P. (2020). A new meso-microscale coupled modelling framework for wind resource assessment: A validation study. *Renewable Energy*, 160:538–554.
- El Bahlouli, A., Leukauf, D., Platis, A., zum Berge, K., Bange, J., and Knaus, H. (2020). Validating CFD Predictions of Flow over an Escarpment Using Ground-Based and Airborne Measurement Devices. *Energies*, 13(18):4688.
- El Bahlouli, A., Rautenberg, A., Schön, M., zum Berge, K., Bange, J., and Knaus, H. (2019). Comparison of CFD Simulation to UAS Measurements for Wind Flows in Complex Terrain: Application to the WINSENT Test Site. *Energies*, 12(10):1992.
- Fernando, H. J. S., Mann, J., Palma, J. M. L. M., Lundquist, J. K., Barthelmie, R. J., Belo-Pereira, M., Brown, W. O. J., Chow, F. K., Gerz, T., Hocut, C. M., Klein, P. M., Leo, L. S., Matos, J. C., Oncley, S. P., Pryor, S. C., Bariteau, L., Bell, T. M., Bodini, N., Carney, M. B., Courtney, M. S., Creegan, E. D., Dimitrova, R., Gomes, S., Hagen, M., Hyde, J. O., Kigle, S., Krishnamurthy, R., Lopes, J. C., Mazzaro, L., Neher, J. M. T., Menke, R., Murphy, P., Oswald, L., Otarola-Bustos, S., Pattantyus, A. K., Rodrigues, C. V., Schady, A., Sirin, N., Spuler, S., Svensson, E., Tomaszewski, J., Turner, D. D., Veen, L. v., Vasiljević, N., Vassallo, D., Voss, S., Wildmann, N., and Wang, Y. (2019). The Perdigão: Peering into Microscale Details of Mountain Winds. *Bulletin of the American Meteorological Society*, 100(5):799–819.
- Filippelli, M. V. (2019). IEC 61400-15 Progress Update and call for participation. Presented at the American Wind Energy Association Wind Resource and Project Energy Assessment Conference (AWEA WRA) .
- Fitch, A. C., Olson, J. B., Lundquist, J. K., Dudhia, J., Gupta, A. K., Michalakes, J., and Barstad, I. (2012). Local and Mesoscale Impacts of Wind Farms as Parameterized in a Mesoscale NWP Model. *Monthly Weather Review*, 140(9):3017–3038.
- Flores-Maradiaga, A., Benoit, R., and Masson, C. (2019). Enhanced modelling of the stratified atmospheric boundary layer over steep terrain for wind resource assessment. *Journal of Physics: Conference Series*, 1222:10.

- Franke, J., Hellsten, A., Schlunzen, K. H., and Carissimo, B. (2011). The COST 732 Best Practice Guideline for CFD simulation of flows in the urban environment: a summary. *International Journal of Environment and Pollution*, 44(1-4):419–427.
- Hemingway, B., Frazier, A., Elbing, B., and Jacob, J. D. (2020). High-Resolution Estimation and Spatial Interpolation of Temperature Structure in the Atmospheric Boundary Layer Using a Small Unmanned Aircraft System . *Boundary-Layer Meteorology*, 175:397–416.
- Hill, M. L., Konrad, T. G., Meyer, J., and Rowland, J. (1970). A small, radio-controlled aircraft as a platform for meteorological sensors.
- Hoffmann, H., Nieto, H., Jensen, R., Guzinski, R., Zarco-Tejada, P., and Friborg, T. (2016). Estimating evaporation with thermal uav data and two-source energy balance models. *Hydrol. Earth Syst. Sci.*, 20:17.
- International Electrotechnical Commission (2017). Wind energy generation systems - Part 12-1: Power performance measurements of electricity producing wind turbines. Technical report, International Electrotechnical Commission (IEC), Geneva, Switzerland.
- Kitamura, Y. (2016). Improving a Turbulence Scheme for the Terra Incognita in a Dry Convective Boundary Layer. *Journal of the Meteorological Society of Japan. Ser. II*, 94(6):491–506.
- Klaas, T., Pauscher, L., and Callies, D. (2015). LiDAR-mast deviations in complex terrain and their simulation using CFD. *Meteorologische Zeitschrift*, pages 591–603.
- Kwak, K.-H., Baik, J.-J., Ryu, Y.-H., and Lee, S.-H. (2015). Urban air quality simulation in a high-rise building area using a CFD model coupled with mesoscale meteorological and chemistry-transport models. *Atmospheric Environment*, 100:167–177.
- Lange, J., Mann, J., Berg, J., Parvu, D., Kilpatrick, R., Costache, A., Chowdhury, J., Siddiqui, K., and Hangan, H. (2017). For wind turbines in complex terrain, the devil is in the detail. *Environmental Research Letters*, 12(9):094020.
- Lauder, B. E. and Spalding, D. B. (1974). The numerical computation of turbulent flows. *Computer Methods in Applied Mechanics and Engineering*, 3(2):269–289.
- Leukauf, D., El-Bahlouli, A., zum Berge, K., Schön, M., Knaus, H., and Bange, J. (2019). The impact of a forest parametrization on coupled WRF-CFD simulations during the passage of a cold front over the WINSSENT test-site. *Wind Energy Science Discussions*.
- Lundquist, J., Clifton, A., Dana, S., Huskey, A., Moriarty, P., Van Dam, J., and Herges, T. (2019). Wind energy instrumentation atlas. Technical report. National Renewable Energy Lab.(NREL), Golden, CO (United States).
- Mauz, M., Rautenberg, A., Platis, A., Cormier, M., and Bange, J. (2019). First identification and quantification of detached-tip vortices behind a wind energy converter using fixed-wing unmanned aircraft system. *Wind Energy Science*, 4(3):451–463.

- Menke, R., Vasiljević, N., Wagner, J., Oncley, S. P., and Mann, J. (2020). Multi-lidar wind resource mapping in complex terrain. *Wind Energy Science*, 5(3):1059–1073.
- Merino, L., Caballero, F., Martínez-de Dios, J., Maza, I., and Ollero, A. (2011). An unmanned aircraft system for automatic forest fire monitoring and measurement. *Journal of Intelligent and Robotic Systems*, 65:533–548.
- Miguel, J. V. P., Fadigas, E. A., and Sauer, I. L. (2019). The Influence of the Wind Measurement Campaign Duration on a Measure-Correlate-Predict (MCP)-Based Wind Resource Assessment. *Energies*, 12(19):3606.
- Miles, J. W. (1961). On the stability of heterogeneous shear flows. *Journal of Fluid Mechanics*, 10(4):496–508.
- Millward-Hopkins, J. T., Tomlin, A. S., Ma, L., Ingham, D. B., and Pourkashanian, M. (2013). Assessing the potential of urban wind energy in a major UK city using an analytical model. *Renewable Energy*, 60:701–710.
- Montelpare, S., D’Alessandro, V., Lops, C., Costanzo, E., and Ricci, R. (2019). A Mesoscale-Microscale approach for the energy analysis of buildings. *Journal of Physics: Conference Series*, 1224:012022.
- Pauscher, L., Vasiljevic, N., Callies, D., Lea, G., Mann, J., Klaas, T., Hieronimus, J., Gottschall, J., Schwesig, A., Kühn, M., and Courtney, M. (2016). An Inter-Comparison Study of Multi- and DBS Lidar Measurements in Complex Terrain. *Remote Sensing*, 8(9):782.
- Platis, A., Altstädter, B., Wehner, B., Wildmann, N., Lampert, A., Hermann, M., Birmili, W., and Bange, J. (2016). An Observational Case Study on the Influence of Atmospheric Boundary-Layer Dynamics on New Particle Formation. *Boundary-Layer Meteorology*, 158:67–92.
- Podlaha, A., Bowen, S., Lörinc, M., Kerschner, B., and Srivastava, G. (2021). Weather, climate & catastrophe insight: 2020 annual report. Technical report, Aon Benfield, Chicago, USA. <https://www.aon.com/global-weather-catastrophe-natural-disasters-costs-climate-change-2020-annual-report/index.html> accessed on 15 July 2020.
- Pope, S. B. (2000). *Turbulent Flows*. Cambridge University Press.
- Popovac, M. (2012). Analytical Method for Estimating Energy Output of Small Wind Turbines Integrated in Urban Areas. *EPJ Web of Conferences*, 33:05011.
- Porté-Agel, F., Bastankhah, M., and Shamsoddin, S. (2020). Wind-Turbine and Wind-Farm Flows: A Review. *Boundary-Layer Meteorology*, 174(1):1–59.
- Rautenberg, A., Schön, M., zum Berge, K., Mauz, M., Manz, P., Platis, A., van Kesteren, B., Suomi, I., Kral, S. T., and Bange, J. (2019). The Multi-Purpose Airborne Sensor Carrier MASC-3 for Wind and Turbulence Measurements in the Atmospheric Boundary Layer. *Sensors*, 19(10):2292.

- Ricci, A., Kalkman, I., Blocken, B., Burlando, M., Freda, A., and Repetto, M. P. (2017). Local-scale forcing effects on wind flows in an urban environment: Impact of geometrical simplifications. *Journal of Wind Engineering and Industrial Aerodynamics*, 170:238–255.
- Richards, P. J. and Hoxey, R. P. (1993). Appropriate boundary conditions for computational wind engineering models using the k-epsilon turbulence model. *Journal of Wind Engineering and Industrial Aerodynamics*, 46-47:145–153.
- Rogers, A., Rogers, J., and Manwell, J. (2005). Uncertainties in results of measure-correlate-predict analyses. *American Wind Energy Association*.
- Rogers, M. M. and Moser, R. D. (1992). The three-dimensional evolution of a plane mixing layer: the Kelvin–Helmholtz rollup. *Journal of Fluid Mechanics*, 243:183–226.
- Santos, P., Mann, J., Vasiljević, N., Cantero, E., Sanz Rodrigo, J., Borbón, F., Martínez-Villagrasa, D., Martí, B., and Cuxart, J. (2020). The Alaiz experiment: untangling multi-scale stratified flows over complex terrain. *Wind Energy Science*, 5(4):1793–1810.
- Santos, P., Yoshiaki, S., Reinaldo, H., Julio, P., and Taves., F. F. (2015). *Atmospheric Stability Effects on Small Wind Turbine Power Collection in a Complex Terrain*. In *Renewable Energy in the Service of Mankind*, volume 1. Springer, Cham.
- Sanz Rodrigo, J., Chavez Arroyo, R., Moriarty, P., Churchfield, M., Kosovic, B., Rethore, P.-E., Hansen, K., Hahmann, A., Mirocha, J., and Rife, D. (2017). Mesoscale to microscale wind farm flow modeling and evaluation. *Wiley Interdisciplinary Reviews: Energy and Environment*, 6:30.
- Sathe, A. and Mann, J. (2013). A review of turbulence measurements using ground-based wind lidars. *Atmospheric Measurement Techniques*, 6(11):3147–3167.
- Sathe, A., Mann, J., Gottschall, J., and Courtney, M. (2011). Can Wind Lidars Measure Turbulence? *Journal of Atmospheric and Oceanic Technology*, 28:853–868.
- Segalini, A., Nakamura, T., and Fukagata, K. (2016). A Linearized k-epsilon Model of Forest Canopies and Clearings. *Boundary-Layer Meteorology*, 161(3):439–460.
- Shaw, R. H. and Schumann, U. (1992). Large-eddy simulation of turbulent flow above and within a forest. *Boundary-Layer Meteorology*, 61(1):47–64.
- Shaw, W. J., Berg, L. K., Cline, J., Draxl, C., Djalalova, I., Gritmit, E. P., Lundquist, J. K., Marquis, M., McCaa, J., Olson, J. B., Sivaraman, C., Sharp, J., and Wilczak, J. M. (2019). The Second Wind Forecast Improvement Project (WFIP2): General Overview. *Bulletin of the American Meteorological Society*, 100(9):1687–1699.
- Skamarock, W. C., Klemp, J. B., Dudhia, J., Gill, D. O., Barker, D. M., Duda, M. G., Huang, X.-Y., Wang, W., and Powers, J. G. (2008). A Description of the Advanced Research WRF Version 3. page 125.
- Smagorinski, J. (1963). General circulation experiments with the primitive equations: I. The basic experiment. *Monthly Weather Review*, 91(3):99–164.

- Stull, R. (1988). *An Introduction to Boundary Layer Meteorology*, volume 13. Springer Science and Business Media.
- Taylor, M., Ralon, P., Anuta, H., and Al-Zoghoul, S. (2020). Renewable power generation costs in 2019. Technical report, International Renewable Energy Agency (IRENA), Abu Dhabi, UAE.
- Tewari, M., Kusaka, H., Chen, F., Coirier, W. J., Kim, S., Wyszogrodzki, A. A., and Warner, T. T. (2010). Impact of coupling a microscale computational fluid dynamics model with a mesoscale model on urban scale contaminant transport and dispersion. *Atmospheric Research*, 96(4):656–664.
- Toja-Silva, F., Kono, T., Peralta, C., Lopez-Garcia, O., and Chen, J. (2018). A review of computational fluid dynamics (CFD) simulations of the wind flow around buildings for urban wind energy exploitation. *Journal of Wind Engineering and Industrial Aerodynamics*, 180:66–87.
- Tominaga, Y., Mochida, A., Shirasawa, T., Yoshie, R., Kataoka, H., Harimoto, K., and Nozu, T. (2004). Cross Comparisons of CFD Results of Wind Environment at Pedestrian Level around a High-rise Building and within a Building Complex. *Journal of Asian Architecture and Building Engineering*, 3(1):63–70.
- van den Kroonenberg, A., Martin, T., Buschmann, M., Bange, J., and Voersmann, P. (2008). Measuring the Wind Vector Using the Autonomous Mini Aerial Vehicle M2AV. *Journal of Atmospheric and Oceanic Technology*, 25(11):1969–1982.
- Veers, P., Dykes, K., Lantz, E., Barth, S., Bottasso, C. L., Carlson, O., Clifton, A., Green, J., Green, P., Holttinen, H., Laird, D., Lehtomäki, V., Lundquist, J. K., Manwell, J., Marquis, M., Meneveau, C., Moriarty, P., Munduate, X., Muskulus, M., Naughton, J., Pao, L., Paquette, J., Peinke, J., Robertson, A., Sanz Rodrigo, J., Sempreviva, A. M., Smith, J. C., Tuohy, A., and Wisser, R. (2019). Grand challenges in the science of wind energy. *Science*, 366(6464):9.
- Versteeg, H. K. and Malalasekera, W. (2007). *An introduction to computational fluid dynamics: the finite volume method*. Pearson Education Ltd, Harlow, England.
- von der Grün, M., Zamre, P., Chen, Y., Lutz, T., Voß, U., and Kraemer, E. (2020). Numerical study and LiDAR based validation of the wind field in urban sites. *Journal of Physics: Conference Series*, 1618.
- Vosper, S. B., Ross, A. N., Renfrew, I. A., Sheridan, P., Elvidge, A. D., and Grubišić, V. (2018). Current Challenges in Orographic Flow Dynamics: Turbulent Exchange Due to Low-Level Gravity-Wave Processes. *Atmosphere*, 9(9):361.
- Wang, Y. S., Miller, D. R., Anderson, D. E., Cionco, R. M., and Lin, J. D. (1992). A spatial length scale analysis of turbulent temperature and velocity fluctuations within and above an orchard canopy. *Boundary-Layer Meteorology*, 59(1-2):125–139.
- Weller, H. G., Tabor, G., Jasak, H., and Fureby, C. (1998). A tensorial approach to computational continuum mechanics using object-oriented techniques. *Computers in Physics*, 12(6):620–631.

- Wharton, S. and Lundquist, J. K. (2012). Atmospheric stability affects wind turbine powercollection. *Environmental Research Letters*, 11:9.
- Wildmann, N., Bernard, S., and Bange, J. (2017). Measuring the local wind field at an escarpment using small remotely-piloted aircraft. *Renewable Energy*, 103:613–619.
- Wyngaard, J. C. (2004). Toward Numerical Modeling in the “Terra Incognita”. *Journal of the Atmospheric Sciences*, 61(14):1816–1826.
- Zamre, P., Dessoky, A., von der Grün, M., Lutz, T., and Krämer, E. (2020). Numerical Study of the Impact of Urban Terrain on the Loads and Performance of a Small Vertical Axis Wind Turbine. *Journal of Physics: Conference Series*, 1618.
- Zängl, G., Gantner, L., Hartjenstein, G., and Noppel, H. (2004). Numerical errors above steep topography: A model intercomparison. *Meteorologische Zeitschrift*, 13(2):69–76.
- Zoumakis, N. M. and Kelessis, A. G. (1991). The dependence of the bulk Richardson number on stability in the surface layer. *Boundary-Layer Meteorology*, 57(4):407–414.
- zum Berge, K., Schoen, M., Mauz, M., Platis, A., van Kesteren, B., Leukauf, D., El Bahlouli, A., Letzgus, P., Knaus, H., and Bange, J. (2021). A Two-Day Case Study: Comparison of Turbulence Data from an Unmanned Aircraft System with a Model Chain for Complex Terrain. *Boundary-Layer Meteorology*, 180(1):53–78.

Appendix: Peer reviewed first-author publications

A.1 Publication I

Experimental and Numerical Wind-Resource Assessment of an University Campus Site

A. El Bahlouli and J. Bange

Abstract During a 3 year research project funded by the local government of Baden-Württemberg, Germany, the potential of wind-energy production was studied at the university campus of Tübingen, a town in the south-west of Germany. The 3D wind field was studied both experimentally and numerically in order to identify optimal locations for small wind turbine installation. Within the scope of this project, a full-scale field experiment and RANS (Reynolds Averaged Navier-Stokes) models were applied in order to yield a better understanding of the airflow around the buildings. We validate our CFD predictions of the flow field with wind-speed measurements using ultrasonic anemometers at several stations within the campus. The simulation results (in direct comparison with the measured data) improved greatly when trees were explicitly considered using a simple canopy model at the inflow boundary. This study is intended to support and guide the next steps of the wind resources assessment at similar sites. We gladly offer our site, instrumentation and (simulated and measured) data to other groups that perform urban wind energy studies.

Keywords Wind flow · Urban environment · RANS · Anemometers

1 Introduction

Several international and national policies and grant programmes are encouraging the use of renewable sources of energy, among which are small-scale wind-energy technologies. Small wind turbines (SWT, less than 100 kW as defined by the World Wind Energy Association WWEA) have shown a remarkable growth in use during recent years mainly in China and the USA. In 2015, an increase of 14% compared with the previous year has been registered for the small wind capacity installed worldwide. This market is expected to reach a steady growth rate of 20% from 2015 to 2020 as reported by the WWEA in their ‘Small Wind World Report Summary’

A. El Bahlouli · J. Bange (✉)
Environmental Physics, University of Tübingen, Hölderlinstr. 12,
72074 Tübingen, Germany
e-mail: jens.bange@uni-tuebingen.de

(www.wwindea.org). These small wind energy technologies were in the focus of a 3 year research project at the University of Tübingen, in the south-west of Germany, as a pioneer study in sustainability and environmental management in the region. The university and the university hospitals of Tübingen are using around 20% of their electricity from renewable sources, at the time of writing. The aim is to increase this share to 35% by 2020. A large and efficient photo-voltaic system is already in service but no wind energy resources are there to complement them. Thus first aim of the study was a detailed wind resource site assessment before locations could be identified where wind-energy resources are possible.

Historically, wind energy technologies were built in open areas with favourable wind conditions, the basic condition in order to harvest significant wind power. The atmospheric boundary layer (ABL) behaves differently in urban environments compared to the flow in open areas. The surface geometry in urban areas is significantly more complex than for open spaces and has a critical influence on wind flow at the micro-meteorological scale. Several studies have shown that urban areas have relatively low average wind speeds [8, 18], but turbulence can be much stronger due to the larger shear and strong local convection in the presence of obstacles and heated concrete, causing extreme wind events of relatively short duration (strong gusts). The presence of buildings disturbs the wind flow by generating zones of wind acceleration, channelling, blocking, re-circulation and increasing turbulence. Wind turbines installed in urban areas should take the features of the urban ABL into account. Such wind turbines will experience frequent wind changes, a large amount of turbulence, gusts and a significant vertical wind component (in conflict with the usual design of wind turbines). All this reduces the expected life time of the turbines, and can increase the risk of breakdowns due to the large amount of fatigue load on the structure. It is therefore necessary to perform more measurements and a detailed wind resource assessment in the potential site to optimise the placement of SWT.

In situ measurements are the only way to characterise the wind flow at the potential sites, adequately. Such measurements are a good way to quantify the wind resource as it accounts for all environmental parameters and weather fluctuations. But these measurements are often limited to a meteorological station installed at a single location that is usually not be fully representative of the flow over the site. And such measurements have to be performed over a long period to get reliable statistics [2]. All these constraints make in situ measurement in the urban environment relatively limited. Thus many studies are conducted in wind tunnel experiments to measure wind flows around building models in a stationary flow.

During the past two decades, many CFD (Computational Fluid Dynamics) methods have been applied in wind project studies. CFD tools offer considerable advantages and provide detailed information of the flow in the whole calculation domain. The use of numerical models for wind engineering application known as Computational Wind Engineering (CWE) increased significantly during the last decade [3]. It is widely recognised that the availability of many physical and numerical parameters in these methods, which can be freely chosen by the user, can lead to wrong assumptions or numerical errors. Typically, a user has to choose the approximation form of the governing equations, the turbulence models, the discretisation schemes, the

computational domain, etc. To overcome this problem, the wind-energy community published several best practice guideline documents and recommendations on the use of CWE, as in [4, 6, 17].

Since the power output from a wind turbine is proportional to the wind speed cubed, accurate estimation of the campus wind speed is essential for accurate power output estimates. In order to study the wind-energy resources at the university site, a detailed wind resource site assessment was planned. Here, we like to present the first step of the wind resources assessment study which include a CFD validation with high-resolution wind data measured on-site.

After 3 years, the project stopped since the funding expired. But we gladly offer our site, instrumentation and (simulated and measured) data to other groups that perform urban wind energy studies.

2 Methodology

2.1 *The Campus Site Specification*

The project focuses on one area, called Morgenstelle, where the average wind speed is estimated to be the highest among the university buildings. The chosen investigation site is located in outlying districts of the city, on top of a hill. The site has a mix of shallow and high buildings with three of them approximately 50 m height. Previous simulation using the meso-scale model METRAS PC [13] on a 500 m × 500 m grid spacing, indicated the prevailing wind direction at the site is south-west, as shown in Fig. 1. The majority of the buildings are oriented in a south-west direction, as well. Upstream the site, i.e. the western part of the campus, is covered with a forest. This area lies in a valley that influences the wind flow at Morgenstelle directly, in case of west or south-west wind direction.

2.2 *The Full Scale Experiment*

A common technique to calculate the energy potential includes wind measurements at least for one annual cycle. Thus, six stations consisting of three-dimensional ultrasonic anemometers (RM Young 81000) have been installed at the site since April, 2014. In order to measure the distortion of the flow due to building effects, different kind of locations for the instruments were chosen, such as roofs, balconies or on the ground (see Fig. 2).

The anemometers are mounted on 3 m masts (the maximum height authorised), except for the balcony station which has a 1 m horizontal boom. Around the anemometers, complementary equipment (e.g. power supply and data acquisition systems) were installed. Due to different conditions at the chosen measurement

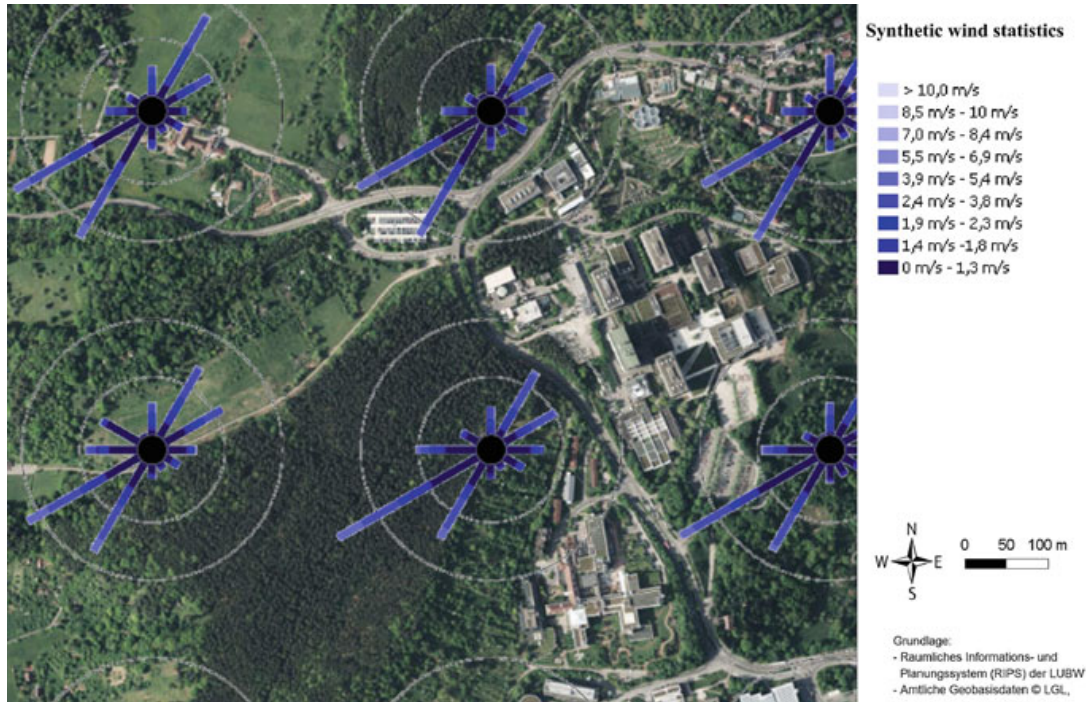


Fig. 1 Aerial view of the site and wind statistics from the METRAS-PC model. *Source* www.udo.lubw.baden-wuerttemberg.de

locations, at some stations data loggers (Campbell Scientific CR800) operating on an external battery are used. For the remaining stations, grid powered systems driven by a microcomputer (Raspberry Pi) were developed and built. The anemometers provide the three wind components and the ‘sonic’ (close to virtual) temperature with high temporal resolution (10 Hz). Therefore, the stations generate a large amount of data, around 300 MByte per day. Thus, a database management using a Structured Query Language (SQL) became necessary.

2.3 The Simulation Set-Up

In the current study, the calculations are carried out only for the prevailing wind direction of 240° . The simulations are performed using the open source C++ code OpenFOAM (openfoam.org). Here, a Reynolds Averaged Navier-Stokes (RANS) approach is used to investigate the flow around and through the site. The computational geometry and domain are built in accordance with the best practice guidelines by [6, 17]. Considering these guidelines, the resulting computational domain has dimensions of $L \times W \times H = 750 \text{ m} \times 1250 \text{ m} \times 350 \text{ m}$. The size of the entire computational domain in the vertical, lateral and flow directions is not limited to the region of interest but includes the surroundings (Fig. 3).



Fig. 2 Photographs of measurement station. 1: balcony, 2: garden, 3: canteen, 4: 'A' building, 5: lecture hall and 6: heating plant

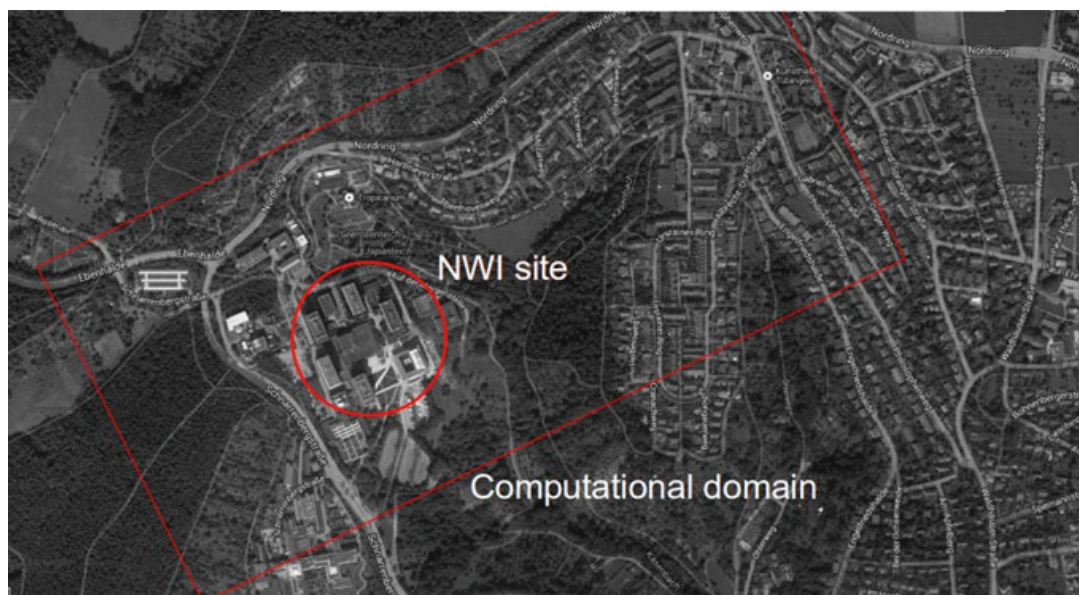


Fig. 3 The computational domain around the Morgenstelle (NWI site)

In the model, the ground has been simplified by assuming it to be flat. The computational grid has been created with the SnappyHexMesh utility (the OpenFOAM mesh generator) and contains approximately 8 millions cells with a resolution of 1.5 m near the area of interest. The simulations were carried out with the k - ε model of [9] and the simpleFoam solver, which is a steady state, incompressible solver. The inlet uses Dirichlet conditions for the velocity U , the turbulent kinetic energy k and the dissipation rate ε with a log-law velocity profile using the OpenFOAM libraries as in [14] with a reference wind speed of 5 m/s at 10 m height. Flow is considered to be fully developed in the outlet, thus we apply a Neumann zero gradient condition for all variables, except for pressure. For this last variable a Neumann zero gradient condition is assumed. For the ground, a no-slip condition is set for the wind field and zero gradient condition is used for the pressure. The wall shear stress is computed by the standard OpenFOAM wall functions with a homogeneous roughness height of 0.03 m. A slip condition is used for the sides (parallel to the flow direction) and the top of the domain.

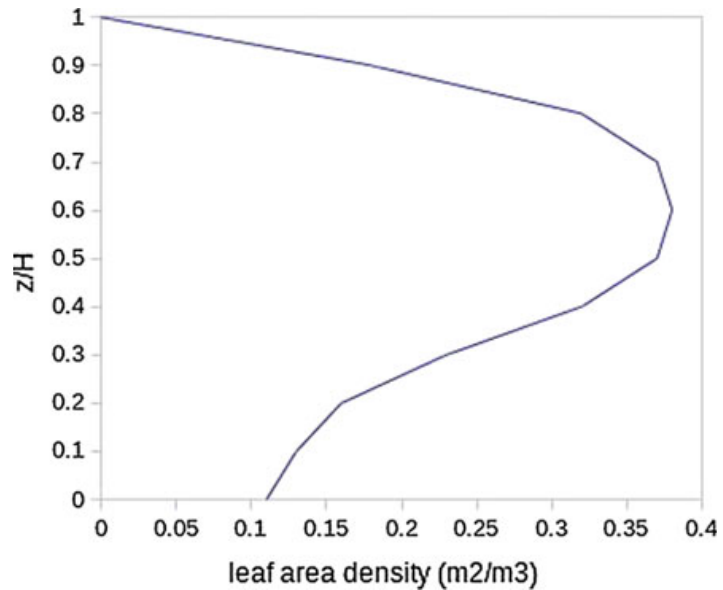
2.4 The Canopy Model

Figure 1 shows that the site is located at the edge of a forest at the in-flow boundary for westerly winds. Thus, it was necessary to include the effect of the forest on the wind flow in our study. In many studies in urban area, details like trees are neglected or implicitly considered in the roughness parameter. E.g. [12, 15] used an explicit representation with a canopy model for reproducing the aerodynamic effects of the trees in urban area. These studies showed that using the implicit approach leads to small effects of trees in most of the urban domain simulated. Thus we decided to consider the effect of the forest at the in-flow boundary using an explicit approach. To include the impact of the forest on the spatial distribution of wind speed, we use a canopy model based on the work of [10] where the vegetation is represented by a leaf area density (LAD) profile. To consider the effects of the canopy of the flow, the incompressibly filtered Navier-Stokes equations have been modified following the ideas of [10]. This method adds an additional drag force D_i in the x_i direction generated by the forest in the following way:

$$D_i = -C_d \text{LAD}(z) V U_i \quad (1)$$

where C_d is a constant drag coefficient, V is the mean wind speed, U_i the local wind velocity in i direction, and LAD the leaf area density at height z . The drag force D_i is added in the momentum equation but also in the kinetic-energy equation and the dissipation equation. The drag coefficient C_d is a parameter which links the canopy architecture with its aerodynamic behaviour. In two mixed forests of the Italian Alps, [5] investigated the drag coefficient experimentally and found mean values around 0.09 ± 0.06 and 0.12 ± 0.06 . Having a mixed forest in our site, we decided to continue our study with a value of 0.15.

Fig. 4 Vertical distribution of leaf area density



The LAD (m^2 leaf area per m^3 canopy volume) is only a function of height in this model and depends on species, developmental stage, leaf season, etc. This function varies over height, since the leaves are not equally distributed along the trunk height. The LAD is derived from the leaf area index LAI as follows:

$$\text{LAI} = \int_z^H \text{LAD} dz \quad (2)$$

A LAI of 5 is chosen after a literature survey, e.g. [7, 11, 16]. Figure 4 shows the resulting leaf area density profile as a function of z/H , where H is the tree height of about 22 m, in our study.

3 Results

3.1 Verification of the Numerical Simulation

Our approach to compare measurements with simulations is somewhat upside-down. We first conducted a simulation and then identified periods in our database that agree with the boundary conditions of the simulation. In order to compare the RANS simulations with our measurement stations, we chose the station mounted on the highest building near the inflow, named ‘A-building’, also shown in Fig. 5, as a first reference. In case of south-west wind, this station is not in the wind shadow of any other building. Also the instruments are located at the leading edge in the centre of the roof. Thus, the wind direction at this station is assumed to be identical with the inlet profile, which equals 240° due to our simulation settings. Knowing the other

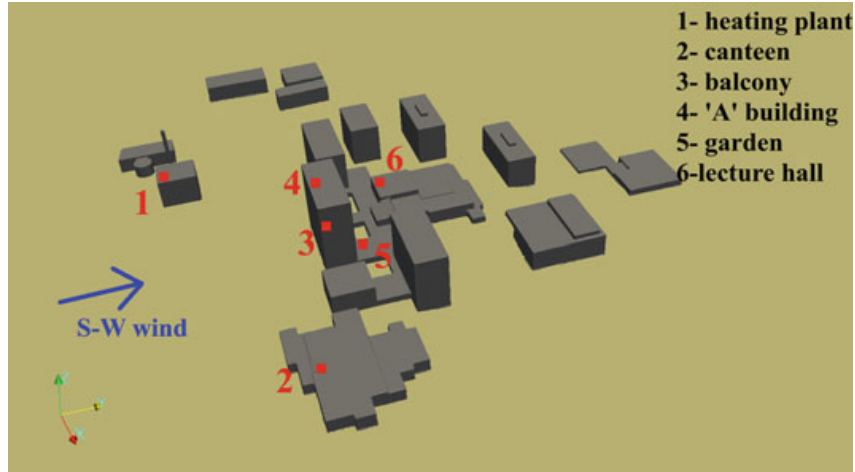


Fig. 5 Top: 3D perspective of Morgenstelle site, buildings are shown in grey, and idealised smoothed topography is shown in brown, the station network is shown in red (color figure online)

station's location, we can easily find the corresponding coordinates in our simulation and extracted the simulated values of the mean wind speed to be expected at the remaining stations.

The simulation gives a mean velocity of 5.40 m s^{-1} at the 'A-building' station. In the SQL database, we look for 30 min periods fulfilling both following conditions at the A-building station:

1. The mean wind speed is $5.40 \pm 0.1 \text{ m s}^{-1}$.
2. The wind direction is $240 \pm 10^\circ$.

Finally, 28 data sets were chosen in order to have various weather conditions (day and night time, cold or warm days), and listed in Table 1.

The scatter plot in Fig. 6 shows the simulated velocities without the application of our canopy model (Sect. 2.4), matched by the 30 min-average wind speed from the stations. The spread in the experimental data (vertical axis) is in the order of 2 m s^{-1} and almost constant for all the stations. The plot shows that the experimental data don't match the simulation well. The stations 5 (garden) and 3 (balcony) are the ones closer to the line of best fit. This can be explained by the fact that station 5 and station 3 are located behind or in a corner of a building (Fig. 5). Thus the data shows mainly the effect of the building regardless of the incoming wind field. Stations 1 (heating plant) and 2 (canteen) are the ones directly influenced by the inlet profile. Here, measurements show much smaller wind speeds compared to the simulation. In general, the simulation over-estimated the real wind speeds significantly, probably due to the insufficient modelling of the incoming wind profile.

Our first simple approach of a flat terrain with a homogeneous roughness height is not suited to the problem. Mainly because the site is surrounded by a significant number of trees in the upstream area. We need to adjust the upstream area of the campus by adding the canopy model (Sect. 2.4) as we expect that the forest has an impact on the spatial distribution of wind speed.

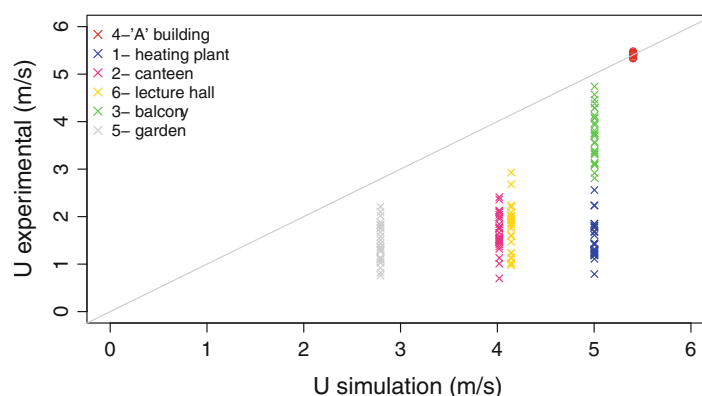
Table 1 Data sets used for comparison. Units for the wind speed are m s^{-1}

Date time	A-Building	Canteen	Heating plant	Balcony	Garden	Lecture hall
03/05/15 12:00	5.43	2.09	1.81	4.29	2.10	–
03/05/15 20:30	5.42	1.50	1.22	3.75	1.51	–
06/05/15 20:30	5.42	1.99	2.23	4.57	1.43	1.87
06/05/15 16:00	5.42	2.13	1.67	3.31	1.83	2.73
06/07/15 01:30	5.43	1.48	1.77	3.76	1.27	2.09
06/07/15 03:30	5.39	1.47	1.80	3.83	1.03	2.01
07/07/15 20:00	5.41	1.01	1.61	3.39	0.82	1.61
07/07/15 04:30	5.34	0.70	1.22	3.13	1.04	1.75
08/07/15 03:30	5.43	1.66	2.24	1.12	4.09	2.02
08/07/15 12:30	5.43	2.36	2.06	1.45	4.38	2.43
15/11/15 20:00	5.44	2.04	1.25	3.57	2.21	2.08
15/11/15 22:00	5.42	1.52	0.89	3.55	2.02	0.97
17/11/15 02:30	5.43	1.13	1.43	3.31	1.09	1.24
17/11/15 04:00	5.45	1.84	1.85	4.29	1.77	1.12
25/12/15 10:00	5.41	1.59	1.32	2.91	1.01	1.88
25/12/15 20:30	5.41	1.37	1.19	3.72	1.03	0.98
29/12/15 05:00	5.36	1.78	1.2	1.46	1.31	1.93
29/12/15 09:00	5.33	2.11	1.11	3.34	0.76	3.34
04/01/16 06:00	5.44	1.47	1.43	3.81	1.28	1.23
04/01/16 18:30	5.42	1.32	1.18	3.09	1.75	1.80

(continued)

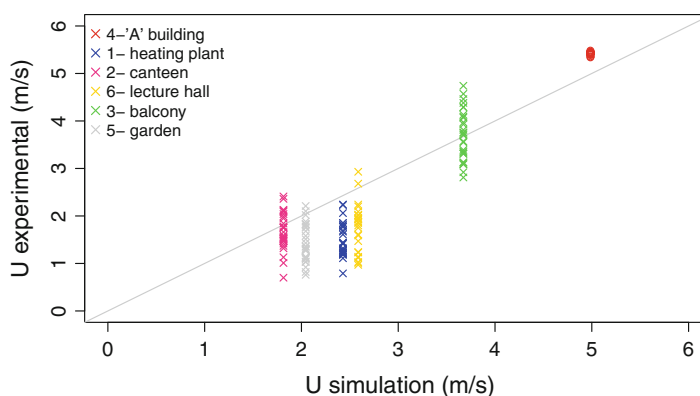
Table 1 (continued)

Date time	A-Building	Canteen	Heating plant	Balcony	Garden	Lecture hall
05/01/16 14:30	5.44	1.53	1.29	3.12	1.28	1.94
05/01/16 19:30	5.42	1.42	1.23	3.36	1.30	1.14
05/02/16 09:00	5.44	1.54	1.44	3.70	1.58	1.85
05/02/16 15:30	5.48	1.75	1.77	3.97	1.81	2.20
06/02/16 08:00	5.40	2.41	1.41	4.74	1.11	1.96
06/02/16 14:00	5.44	1.56	1.28	2.92	1.36	1.47
10/02/16 03:00	5.45	1.75	1.69	4.13	1.68	2.24
10/02/16 05:30	5.45	1.95	1.85	4.07	1.83	1.92

Fig. 6 Scatter plot of measured wind speed against simulated wind speed

Results of the simulation using the canopy model are shown in the Fig. 7. Now, all the simulated wind velocities are decreased compared to the previous case, but meet the experimental data much better. However, station 1 (heating plant) still shows a significant difference between the experimental data and simulation result. It should be noted that this station is located only 30m away from the forest and thus is very sensitive to the forest representation in the model, which is—so far in this study and in contrast to reality—horizontally homogeneous. An even more detailed forest model might give further improvements. However, the results illustrate the importance of having a realistic inlet profile by considering, for example, the forest canopy.

Fig. 7 Scatter plot of measured wind speed against simulated wind direction with a canopy forest



3.2 Accelerated Flow Around and Above the Buildings

The following 3D figures were obtained using the post-processing tool Paraview [1] which helps to identify the areas where the velocity is increased (in comparison to the inlet velocity) and to visualise the air flow, both in three dimensions. Figure 8 shows the velocity streamlines. Air flow patterns around buildings is quite complex. At the windward surface of the buildings, where the wind first impacts the buildings, the wind stream splits above and around the sides of the buildings. The air flow accelerates around the corners of the building causing a high speed region of the corner and a weak wind region on the sides of the buildings.

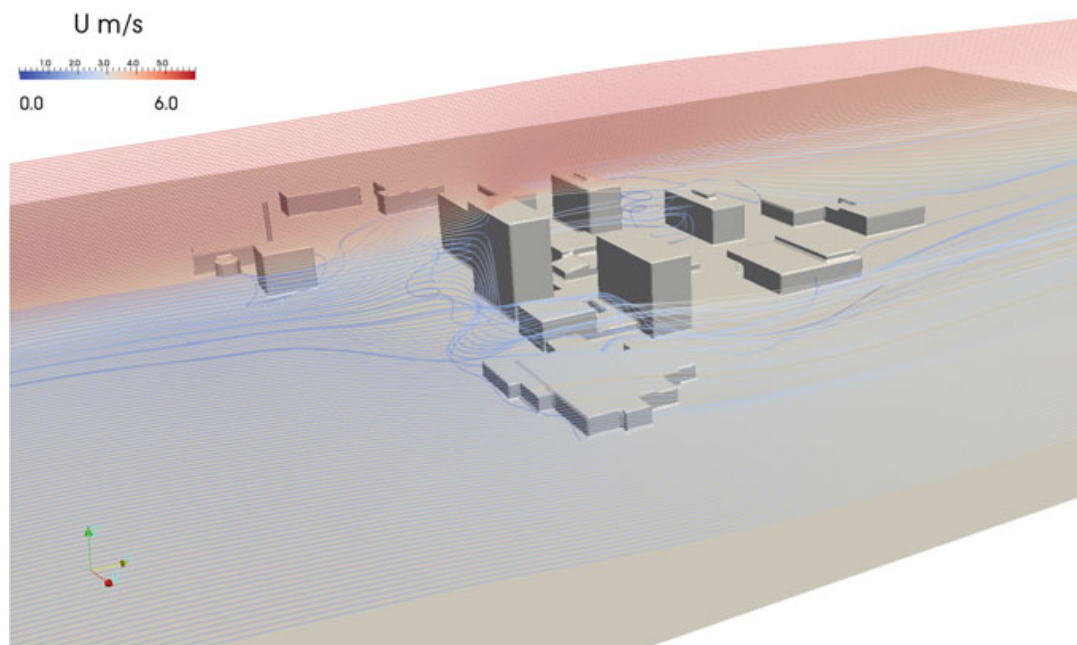


Fig. 8 Velocity stream lines at Morgenstelle campus. Colours indicate wind speed close to zero (blue) up to 6 m/s (red) (color figure online)

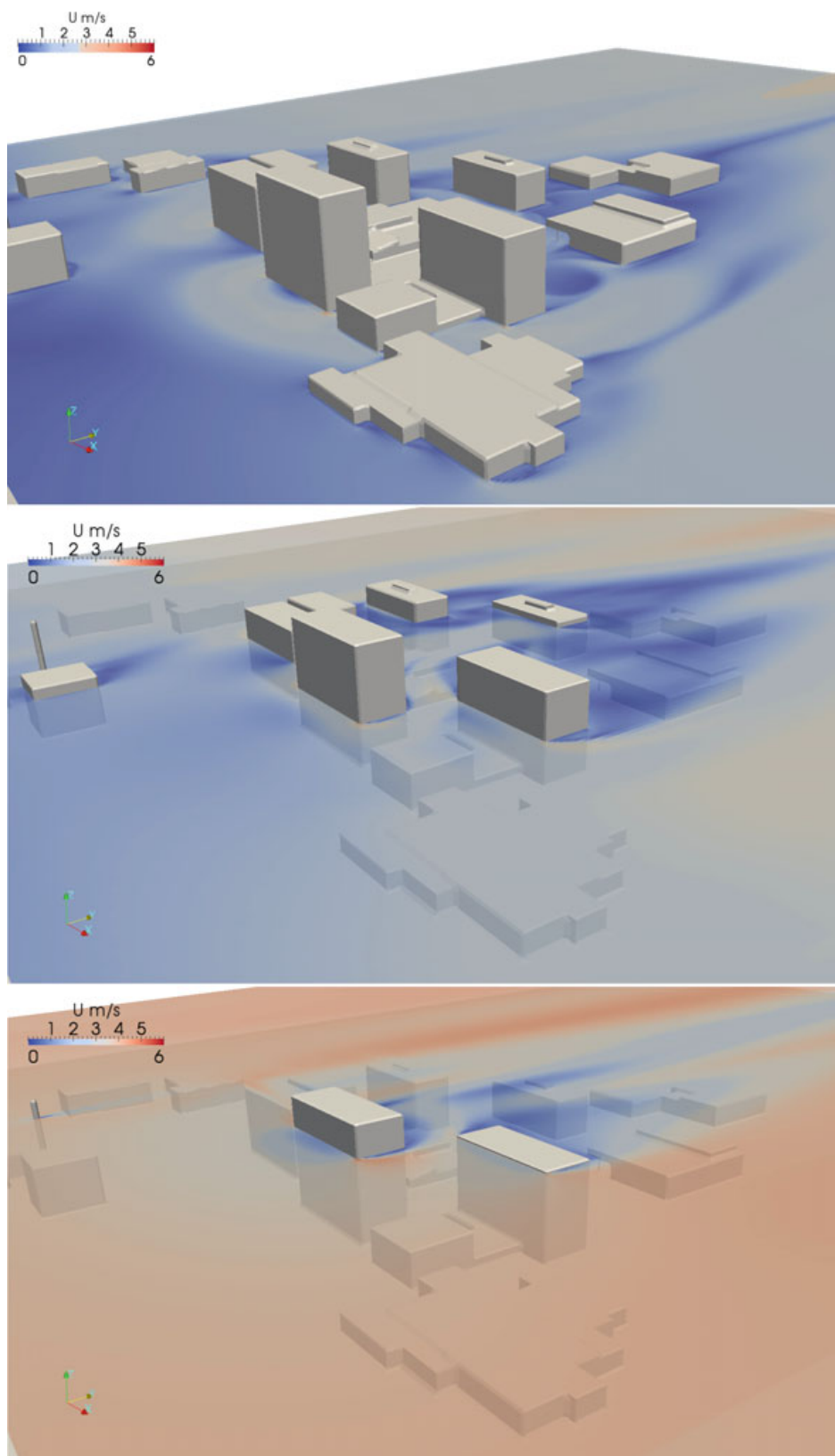


Fig. 9 Velocity contour-plots at height of: (top) 2 m, (centre) 20 m and (bottom) 50 m

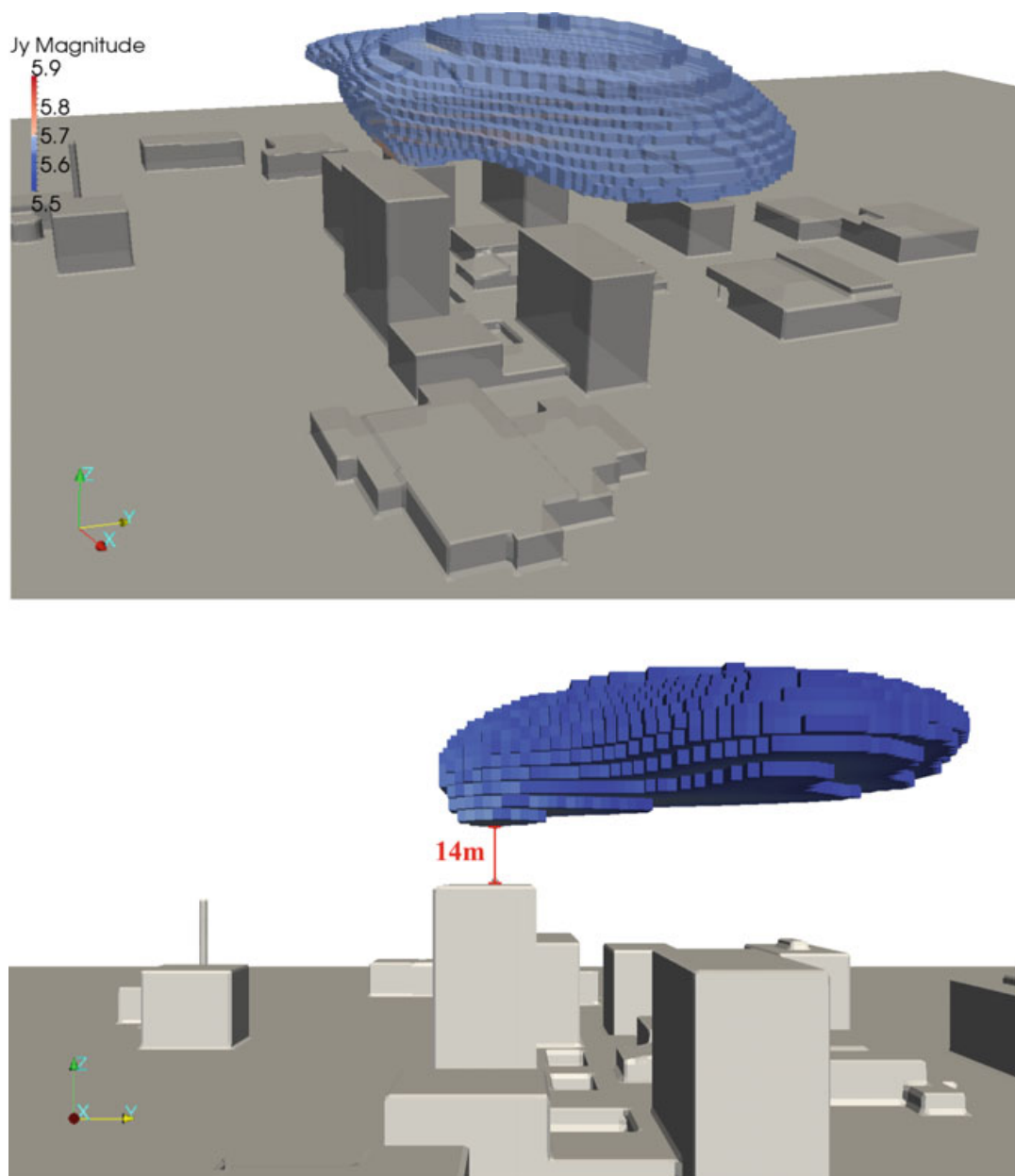


Fig. 10 Model cells with a minimum velocity increase of 10%. Top: 3D view, and bottom: side view

The velocity contour-plots at different heights (Fig. 9) illustrate this phenomena. The wind speed is also increasing with altitude as expected (due to the logarithmic wind profile at the inlet).

The blue area in Fig. 10 (top) represents the cells with a minimum horizontal wind speed increase of 10%, which corresponds to a minimum of 5.5 m/s. This area is located over the 'A'-building and—due to its increased wind speed—is attractive for wind-energy production. To reach this area, a mast of minimum 14m height with a turbine on top would be necessary, as seen in Fig. 10 (bottom).

4 Conclusion and Outlook

This paper reports the first step of the feasibility of wind power utilisation in a university campus and find out how to model the wind flow in the built environment more effectively. Two RANS simulations were performed for the flow over and through the university buildings. Including a canopy model improved the simulation results significantly, demonstrating the importance of having a realistic inlet profile. While these simulations represent first results, they illustrate the potential for future investigations of canopy turbulence. And a more realistic ground model (and horizontally heterogeneous inlet) would improve the results even more.

We planned to measure the incoming wind flow over the forest in more detail using a small unmanned aerial vehicle UAV [19, 20]. The research UAV MASC (Multi-purpose Airborne Sensor Carrier) can resolve turbulence fluctuation of wind and temperature up to 30Hz. Legs (straight and level flight sections) of approximately 1 km total length can be flown over the forest at various altitudes. By comparing turbulent statistics calculated over several legs at a given height, the average and temporal trend of any spatially averaged variables can be computed for that height. Therefore, new experimental data will be added for CFD validation.

The first step of this wind resource assessment helped us to identify important parameters in our model which were validated with our long term measurements. The next step will consist of identifying spots with higher wind speeds and low magnitude of turbulence using CFD tools which can provide detailed information of the flow in the whole calculation domain. After picking the best locations, the optimal type of wind turbine will be chosen, and an estimation of the power output can be given.

However, after 3 years the project funding ceased. During this period, six turbulence stations were built and mounted, and a measurement data base including user interface was designed. Also various CFD methods were tested and simulation runs were performed on different computation clusters. It is understood that the presented results are preliminary and that there is room for plenty of improvements and extensions. Currently, the project is paused until we applied successfully for a new grant or/and we found a new partner who wants to use the installations and the database at the urban wind field research site Morgenstelle.

Acknowledgements The authors thank the Ministry of Science, Research and the Arts of the State of Baden-Württemberg for funding this study, the Geographical Institute of the University of Tübingen for providing terrain data, and the Technical Building Management (TBA) of the University of Tübingen for assisting the experimental part. The computational resources were provided by the bwGRiD Cluster at the University of Tübingen.

References

1. Ayachit, U.: The paraview guide: a parallel visualization application (2015)
2. Bailey, B.H., McDonald, S.L., Bernadett, D., Markus, M., Elsholz, K.: Wind resource assessment handbook: fundamentals for conducting a successful monitoring program. Tech. rep., National Renewable Energy Lab., Golden, CO (US); AWS Scientific, Inc., Albany, NY (US) (1997)
3. Blocken, B.: 50 years of computational wind engineering: past, present and future. *J. Wind Energy Ind. Aerodyn.* **129**, 69–102 (2014)
4. Blocken, B., Gualtieri, C.: Ten iterative steps for model development and evaluation applied to computational fluid dynamics for environmental fluid mechanics. *Env. Model. Softw.* **33**, 1–22 (2012)
5. Cescatti, A., Marcolla, B.: Drag coefficient and turbulence intensity in conifer canopies. *Agric. For. Meteorol.* **121**, 197–206 (2004)
6. Franke, J., Hellsten, A., Schlunzen, H., Carissimo, B.: The COST 732 best practice guideline for CFD simulation of flows in the urban environment: a summary. *Int. J. Env. Pollut.* **44**, 419–427 (2011)
7. Greens, S., Grace, J., Hutchings, N.: Observations of turbulent air flow in three stands of widely spaced sitka spruce. *Agric. For. Meteorol.* **74**, 205–225 (1996)
8. Landberg, L., Myllerup, L., Rathmann, O., Petersen, L., Hoffmann Jrgensen, B., Badger, J., Gylling Mortensen, N.: Wind resource estimation—an overview. *Wind Energy* **6**, 261–271 (2003)
9. Launder, B.E., Spalding, D.: The numerical computation of turbulent flows. *Comput. Meth. Appl. Mech. Eng.* **3**, 269–289 (1974)
10. Liu, J., Chen, J., Novak, M.: k-epsilon modelling of turbulent air flow downwind of a model forest edge. *Bound.-Layer Meteorol.* **77**, 21–44 (1996)
11. Meier, I., Leuschner, C.: Leaf size and leaf area index in fagus sylvatica forests: competing effects of precipitation, temperature, and nitrogen availability. *Ecosystems* **11**, 655–669 (2008)
12. Mochida, A., Tabata, Y., Iwata, T., Yoshino, H.: Examining tree canopy models for CFD prediction of wind environment at pedestrian level. *J. Wind Energy Ind. Aerodyn.* **96**, 1667–1677 (2008)
13. Rau, I.M., Bigalke, K.: Synthetische Windstatistiken Baden-Württemberg Hinweise für Anwender. Landesanstalt für Umwelt, Messungen und Naturschutz Baden-Württemberg (2007)
14. Richards, P., Hoxey, R.: Appropriate boundary conditions for computational wind engineering models using the k-epsilon turbulence models. *J. Wind Energy Ind. Aerodyn.* **46–47**, 145–153 (1993)
15. Salim, M.H., Schlunzen, H.K., Grawe, D.: Including trees in the numerical simulations of the wind flow in urban areas: should we care? *J. Wind Energy Ind. Aerodyn.* **144**, 84–95 (2015)
16. Thimonier, A., Sedivy, I., Schleppi, P.: Estimating leaf area index in different types of mature forest stands in switzerland: a comparison of methods. *Eur. J. For. Res.* **129**, 543–562 (2010)
17. Tominaga, Y., Mochida, A., Yoshie, R., Kataoka, H., Nozu, T., Yoshikawa, M., Shirasawa, T.: AIJ guidelines for practical applications of CFD to pedestrian wind environment around buildings. *J. Wind Energy Ind. Aerodyn.* **96**, 1749–1761 (2008)
18. Walker, S.: Building mounted wind turbines and their suitability for the urban scale: a review of methods of estimating urban wind resource. *J. Energy Build.* **43**, 1852–1862 (2013)
19. Wildmann, N., Hofsäß, M., Weimer, F., Joos, A., Bange, J.: MASC—a small remotely piloted aircraft (RPA) for wind energy research. *Adv. Sci. Res.* **11**, 55–61 (2014)
20. Wildmann, N., Rau, G., Bange, J.: Observations of the early morning boundary-layer transition with small remotely-piloted aircraft. *Bound.-Layer Meteorol.* **157**(3), 345–373 (2015)

A.2 Publication II

Article

Comparison of CFD Simulation to UAS Measurements for Wind Flows in Complex Terrain: Application to the WINSENT Test Site

Asmae El Bahlouli ^{1,*}, Alexander Rautenberg ², Martin Schön ², Kjell zum Berge ², Jens Bange ² and Hermann Knaus ¹

¹ Faculty of Building Services-Energy-Environment, Esslingen University of Applied Sciences, 73728 Esslingen, Germany; hermann.knaus@hs-esslingen.de

² Center for Applied Geoscience, Eberhard Karls University, 72074 Tübingen, Germany; alexander.rautenberg@uni-tuebingen.de (A.R.); martin.schoen@uni-tuebingen.de (M.S.); kjell.zum-berge@uni-tuebingen.de (K.z.B.); jens.bange@uni-tuebingen.de (J.B.)

* Correspondence: asmae.el-bahlouli@hs-esslingen.de

Received: 7 April 2019; Accepted: 21 May 2019; Published: 24 May 2019



Abstract: This investigation presents a modelling strategy for wind-energy studies in complex terrains using computational fluid dynamics (CFD). A model, based on an unsteady Reynolds Averaged Navier-Stokes (URANS) approach with a modified version of the standard $k-\varepsilon$ model, is applied. A validation study based on the Leipzig experiment shows the ability of the model to simulate atmospheric boundary layer characteristics such as the Coriolis force and shallow boundary layer. By combining the results of the model and a design of experiments (DoE) method, we could determine the degree to which the slope, the leaf area index, and the forest height of an escarpment have an effect on the horizontal velocity, the flow inclination angle, and the turbulent kinetic energy at critical positions. The DoE study shows that the primary contributor at a turbine-relevant height is the slope of the escarpment. In the second step, the method is extended to the WINSENT test site. The model is compared with measurements from an unmanned aircraft system (UAS). We show the potential of the methodology and the satisfactory results of our model in depicting some interesting flow features. The results indicate that the wakes with high turbulence levels downstream of the escarpment are likely to impact the rotor blade of future wind turbines.

Keywords: wind simulation; complex terrain; unsteady Reynolds averaged Navier-Stokes (URANS); design of experiments (DoE); unmanned aircraft system (UAS)

1. Introduction

Wind power is currently one of the most promising renewable energy sources. The year 2017 was a record year for annual installations in Europe, with 16.8 GW of additional wind power capacity installed. Wind energy remains the second largest form of power generation capacity in Europe, closely approaching gas installations. In the EU, wind energy overtook nuclear energy in 2013, hydro in 2015, and coal in 2016. In 2017, offshore installed wind power capacity represented 15.8 GW against 153 GW for onshore installations [1]. Onshore installations are mainly built on flat terrain, making them easier to operate compared to those mounted on hilly terrain, where forecasts are more uncertain, wear and tear is greater, and maintenance and construction costs are higher. However, wind energy in mountainous regions has been making inroads in recent years and is of increasing interest to the wind-energy community.

WindForS, a wind energy research cluster in Southern Germany, aims to answer the question of how to optimize installations in complex terrains and extend their service life. In the framework of the

project Wind Science and Engineering in Complex Terrain (WINSSENT), a field-test site for research and industry, located behind an escarpment in the Swabian Alps, near the town of Geislingen an der Steige is setting up. The project working plan is divided into two stages: the first phase investigates the local wind flow without wind turbines where different measurement equipment is used to characterize the wind flow, such as towers equipped with anemometers, Lidar [2], eddy-covariance stations, and an unmanned aircraft system (UAS) (see [3–5]). The second stage will include two wind turbines with a nominal output of around 750 kW. The turbine-terrain interference will be studied in this second phase.

Characterizing the wind flow in complex terrain is more challenging compared to flat terrain. At these locations, wind flows are more complex, and they are influenced by changes in topography such as hills, escarpments, and roughness, leading to non-linear features such as high levels of turbulence, wind shear, unsteadiness, etc. Analytical models, mainly developed in the 1970s and 1980s such as the well-known Wind Atlas Analysis and Application Program (WASP), are capable of predicting the mean wind field only in simple geometries and are suitable only for attached flow (see [6–9] and others). Modelling non-linear features of the flow became a feasible option with the help of computational fluid dynamics (CFD) solvers which retain the nonlinearity of the Navier-Stokes equations and simulate momentum, turbulence, and energy [10]. The commonly referenced field experiment of Bolund hill, which consists of a steep hill, has been used for a blind comparison of models with different ranges of fidelity (linearized and CFD models) as reported in [11]. One of the outcomes of this comparison was that the linearized models were not able to predict the mean flow features such as the speed-up, unlike the CFD models (see [12] for a complete review). In [13], the flow field over a large-scale model of the same hill was investigated experimentally and showed that the mean wind, wind shear, and turbulence level are extremely sensitive to the details of the terrain. Making the edge of the hill sharper resulted in a reduction of the estimated annual energy production by at least 50% and an increase in the turbulent level by a factor of five in the worst-case scenario. They concluded “the mean wind, wind shear, and turbulence level are extremely sensitive to the exact details of the terrain”. This shows that special attention should be paid not only to the model but also to the topography representation in complex terrains by using high-resolution topographic data and information on land use, such as the Corine land cover [14].

The use of large eddy simulation (LES) or detached eddy simulation (DES) in complex terrain has increased in recent years. These models are superior to both steady and unsteady Reynolds averaged Navier-Stokes (RANS) as they have the advantage of providing additional information on turbulent structures and non-linear features of wind flow over complex terrain. However, the requirement of high computational resources and the challenge of obtaining proper inflow boundary conditions limits their usefulness for wind engineering studies where a fast solution is required [10]. In addition, for wind-energy applications, the simulation often needs to be computed for different wind directions or stability conditions. Due to these constraints, RANS/URANS models are still appropriate for use as they provide a good balance between computational effort and model accuracy.

A common problem when using CFD models in a complex terrain is how to specify initial and boundary conditions. A standard way to proceed is to impose a standard logarithmic velocity profile at an inlet which is orientated perpendicular to the wind direction. Another approach is to use numerical weather prediction (NWP) models, also called mesoscale models, to provide more realistic boundary conditions for the CFD simulations. Mesoscale models, generally, have a low spatial resolution with a horizontal extent on the order of 2 km and they generally present a bias on the predicted wind speed and turbulent quantities in complex terrains due to unresolved topographic effects. In [15], the WRF mesoscale model for the Horns Rev wind farm was applied with a horizontal resolution of 333 m and showed that the model still underestimates the power deficit due to its coarse resolution. Nevertheless, as demonstrated in [16], much effort has been made to improve the NWP models. Coupling a mesoscale model to a microscale model (CFD), which presents a more detailed representation of the topography seems to be one of the more promising approaches for wind-energy assessment in complex terrain. Several coupling methods of mesoscale and microscale models have been developed in the last decade,

and an overview of these methods can be found in [10,17]. One of the most common coupling methods is the one-way approach where the mesoscale model is coupled to the microscale model through the lateral boundaries at fixed times (time-slice). This approach has been successfully applied in complex terrain by several authors as [18–20] among others.

In the present paper, the WINSSENT test site is studied by means of numerical simulations along with UAS data. We confine the study to a neutral stratification case. Section 2 presents the physical model with its validation, while Section 3 presents the parametric study. The parametric study is conducted with the help of a design of experiment (DoE) method applied to a two-dimensional case. This study intends to assess the sensitivity of our model results for different parameters and predict their effect on some relevant variables for wind turbines. Section 4 gives an overview of the test site and the measurement system, while Section 5 presents the model which uses the one-way coupling approach. The same section compares simulation results against UAS measurements. Section 6 draws a summary and discusses the limitation of the model and possible future improvements.

2. Methods

2.1. Numerical Model

To simulate the atmospheric boundary layer (ABL) flow, the finite volume method (FVM) on the OpenFOAM v2.4.0 (Open Source Field Operation and Manipulation) software, provided by the OpenFOAM Foundation U.K., was used [21]. The OpenFOAM toolbox includes open source C++ libraries released under the general public license (GPL). An unsteady Reynolds Averaged Navier-Stokes approach under the Boussinesq approximation, where density is only influenced by buoyancy forces, was considered [22]. The transport equations for mass, momentum, and potential temperature can be written relative to a hydrostatic state (index h) in a Cartesian coordinate as:

$$\frac{\partial(\rho_h)}{\partial t} + \frac{\partial(\rho_h u_j)}{\partial x_j} = 0 \quad (1)$$

$$\frac{\partial(\rho_h u_i)}{\partial t} + \frac{\partial(\rho_h u_i u_j)}{\partial x_j} = -\frac{\partial p}{\partial x_i} + \frac{\partial}{\partial x_j} \left[(\mu + \mu_t) \left(\frac{\partial u_i}{\partial x_j} + \frac{\partial u_j}{\partial x_i} \right) - \frac{2}{3} k \delta_{ij} \right] - \rho_h \left(\frac{\theta - \theta_h}{\theta_h} \right) g + F_c + S_u \quad (2)$$

$$\frac{\partial(\rho_h \theta)}{\partial t} + \frac{\partial(\rho_h u_i \theta)}{\partial x_i} = \frac{\partial}{\partial x_j} \left[\left(\mu + \frac{\mu_t}{\sigma_h} \right) \left(\frac{\partial \theta}{\partial x_j} \right) \right] \quad (3)$$

where U_i ($i = 1, 2, 3$) are the velocity component in the x , y , and z directions, respectively, p and θ are the pressure and potential temperature, μ and μ_t are the molecular and the turbulent eddy viscosities, g is the gravitational acceleration, and σ_h is the turbulent Prandtl number. F_c is the Coriolis force defined as $\varepsilon_{ijk} f_c U_k$, where $f_c = 2\Omega \sin \lambda$ is the Coriolis parameter, a function of the Earth's angular velocity Ω and the latitude λ . S_u is the source term representing a forest canopy and described later by Equation (14). The hydrostatic fluid density ρ_h is given in a hydrostatic reference state (subscript 0) as a function of the hydrostatic pressure p_h and the temperature T_h as:

$$\rho_h = \frac{p_h}{R_d T_h} \quad (4)$$

$$T_h = \sqrt{T_0^2 - \frac{2 A g z}{R_d}} \quad (5)$$

$$p_h = p_0 \left(-\frac{T_0}{A} + \sqrt{\left(\frac{T_0}{A} \right)^2 - \frac{2 A g z}{R_d A}} \right) \quad (6)$$

with the constant reference pressure p_0 usually set to 1000 hPa, T_0 is the reference temperature equal to 288.5 K, $A = 50$ K and $R_d = 287.05 \text{ J}\cdot\text{kg}^{-1}\cdot\text{K}^{-1}$ according to [23,24].

We introduce the hydrostatic potential temperature which is, by definition, a function of the temperature and the pressure according to an adiabatic state change as follows:

$$\theta_h = T_h \left(\frac{p_0}{p_h} \right)^{\frac{R}{c_p}} \quad (7)$$

To close the given set of equations above, the $k - \varepsilon$ model was used. The standard $k - \varepsilon$ model, when applied to ABL studies, is known to lead to a turbulent length scale l , that grows approximately linearly with the height and thus, possesses very deep boundary layers. In real ABL flows, the turbulent length scale is limited by the ABL height or the stability [25,26]. To overcome this problem, the mixing length model proposed by [25], which introduces a limiting size of turbulent eddies l_{max} in the ABL is used. The two modified transport equations for the turbulent kinetic energy k and the dissipation ε read:

$$\frac{\partial(\rho_h k)}{\partial t} + \frac{\partial(\rho_h u_j k)}{\partial x_j} = \frac{\partial}{\partial x_j} \left[\left(\mu + \frac{\mu_t}{\sigma_k} \right) \left(\frac{\partial k}{\partial x_j} \right) \right] + P + G + S_k - \rho_h \varepsilon \quad (8)$$

$$\frac{\partial(\rho_h \varepsilon)}{\partial t} + \frac{\partial(\rho_h u_j \varepsilon)}{\partial x_j} = \frac{\partial}{\partial x_j} \left[\left(\mu + \frac{\mu_t}{\sigma_\varepsilon} \right) \left(\frac{\partial \varepsilon}{\partial x_j} \right) \right] + C_{\varepsilon 1}^* (P + G) + S_\varepsilon - C_{\varepsilon 2} \frac{\varepsilon^2}{k} \quad (9)$$

where P represents the production rate of turbulent kinetic energy due to shear and G represents the production/destruction of turbulence by buoyancy forces defined as:

$$P = \tau_{ij} \left(\frac{\partial u_i}{\partial x_j} \right) = \mu_t \left(\frac{\partial u_i}{\partial x_j} + \frac{\partial u_j}{\partial x_i} \right) \frac{\partial u_i}{\partial x_j} - \frac{2}{3} \rho_h \frac{\partial u_k}{\partial x_k} \delta_{ij} \quad (10)$$

$$G = -\frac{1}{T_h} g \frac{\mu_t}{\sigma_h} \frac{\partial \theta}{\partial x_i} \quad (11)$$

S_k and S_ε are source terms relative to the forest canopy and described later in Equations (15) and (16). $\sigma_k, \sigma_\varepsilon, C_{\varepsilon 1}^*, C_{\varepsilon 2}$ are model coefficients listed in Table 1. These constants were adapted to atmospheric conditions, as proposed by [26]. $C_{\varepsilon 1}^*$ introduces the maximum mixing length l_{max} in the following:

$$C_{\varepsilon 1}^* = C_{\varepsilon 1} + (C_{\varepsilon 2} - C_{\varepsilon 1}) \frac{l}{l_{max}} \quad (12)$$

where the mixing length l is equal to the dissipation length defined as $l_\varepsilon = (C_\mu^{\frac{3}{4}} k^{\frac{3}{2}}) / \varepsilon$. Several mixing-length models in the literature enable estimation of the limiting turbulent size of turbulent eddies in the ABL l_{max} , see [27] for a review. For neutral flows, this length is computed using the Blackadar equation [28] as:

$$l_{max} = 0.00027 \frac{U_g}{2\Omega \sin \lambda} \quad (13)$$

where U_g is the geostrophic wind velocity.

Table 1. Constants used in $k - \varepsilon$ turbulence models.

Turbulence Model Constants	C_μ	$C_{\varepsilon 1}$	$C_{\varepsilon 2}$	σ_ε	σ_k
Standard [29]	0.09	1.44	1.92	1.00	1.3
Adapted [26]	0.256	1.13	1.90	0.74	1.3

In order to account for the effects of vegetation on the wind flow, terms in the transport equation of momentum Equation (2), turbulent kinetic energy Equation (8), and turbulence dissipation rate Equation (9) were added:

$$S_u = -\rho_h C_d LAD(z) |U| u_i \quad (14)$$

$$S_k = -\rho_h C_d LAD(z) (\beta_p |U|^3 - \beta_d |U| k) \quad (15)$$

$$S_\varepsilon = -\rho_h C_d LAD(z) \frac{\varepsilon}{k} (C_{\varepsilon 4} \beta_p |U|^3 - C_{\varepsilon 5} \beta_d |U| k) \quad (16)$$

where $|U|$ is the velocity magnitude and C_d the leaf drag coefficient. The values of this drag coefficient vary between 0.1 and 0.3 for most of the vegetation [30]. A value of 0.2 will be considered for the rest of the study. β_p , β_d , $C_{\varepsilon 4}$, and $C_{\varepsilon 5}$ are model constants proposed by [30] and reported in Table 2. Vegetation is discretized into finite volumes where the total amount of leaves per given volume is defined by the leaf area density (LAD) and the sum of each layer's LAD value over the total canopy height H is called the leaf area index (LAI). A typical profile of the LAD for a deciduous forest can be seen in Figure 1. The relationship between the LAI and LAD can be expressed as follows:

$$LAI = \int_0^h LAD(z) dz \quad (17)$$

Table 2. Constants used for the canopy model.

Closure Constants	β_p	β_d	$C_{\varepsilon 4}$	$C_{\varepsilon 5}$
Value	1	5.1	0.9	0.9

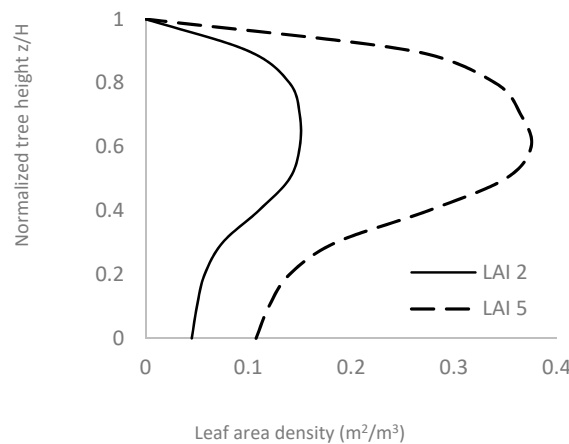


Figure 1. Typical distribution of LAD for a deciduous forest. LAI of 2 and 5 are used in the simulations in this study.

The URANS equations were solved using a PIMPLE pressure-velocity coupling algorithm. The PIMPLE solver is considered as it offers the possibility to visualize the transient effects, which will be part of our future investigation. The gradient terms and Laplacian terms were discretized using a 2nd order linear interpolation, while a 2nd order upwind interpolation was applied for divergence terms. The convergence criteria for residuals were ensured to be less than 10^{-6} .

2.2. k - ε Model Validation

The numerical model was verified using the solution of the Leipzig wind profile. This profile was measured from a set of 28 double-theodolite balloons between 9:15 and 16:15 on the 20 October 1931 as reported in [31]. The ABL was considered as horizontally-homogeneous with a geostrophic

wind speed $U_g = 17.5 \text{ m}\cdot\text{s}^{-1}$ and a Coriolis parameter $f_c = 1.13 \times 10^{-4} \text{ s}^{-1}$ corresponding to a latitude of 45 degrees N. Simulations were carried out using two $k - \varepsilon$ models with the constants adapted to atmospheric conditions, as listed in Table 1, except for $C_{\varepsilon 1}$. $C_{\varepsilon 1}$, which were considered as constant in the first model and as a function of the size of turbulent eddies in the second model (Equation (12)), called respectively $k - \varepsilon$ unlimited and $k - \varepsilon$ limited. A maximum mixing length l_{max} of 36 m was used in the $k - \varepsilon$ limited, as reported by [25,26]. A computational domain of $1 \text{ km} \times 1 \text{ km} \times 3 \text{ km}$ in the x , y , and z directions, spatially resolved with $50 \times 50 \times 200$ cells was defined. A geostrophic wind velocity $U_g = (17.7, 0, 0) \text{ m}\cdot\text{s}^{-1}$ at the top of the domain and at a constant roughness length of $z_0 = 0.3 \text{ m}$ was prescribed on the ground. The boundaries at the domain sides were defined as cyclic.

The results of the two models, together with the experimental data, are shown in Figure 2. Figure 2a,b shows vertical profiles of the wind component v perpendicular to the geostrophic wind and the component u , parallel to the geostrophic wind U_g . The measured vertical profile of the velocity shows a low-level jet and shear on the wind direction. The Coriolis term in the model lead to a turning in the boundary layer which is depicted by the velocity component v . While the limited model simulated the profile reasonably well, the unlimited model showed a flat profile. Figure 2c shows a surface wind turned by 24.3° to the geostrophic wind for the limited model. This is close to the measured value of 26° . The unlimited version predicts a smaller cross-isobar angle of 12.0° due to the flat v -profile.

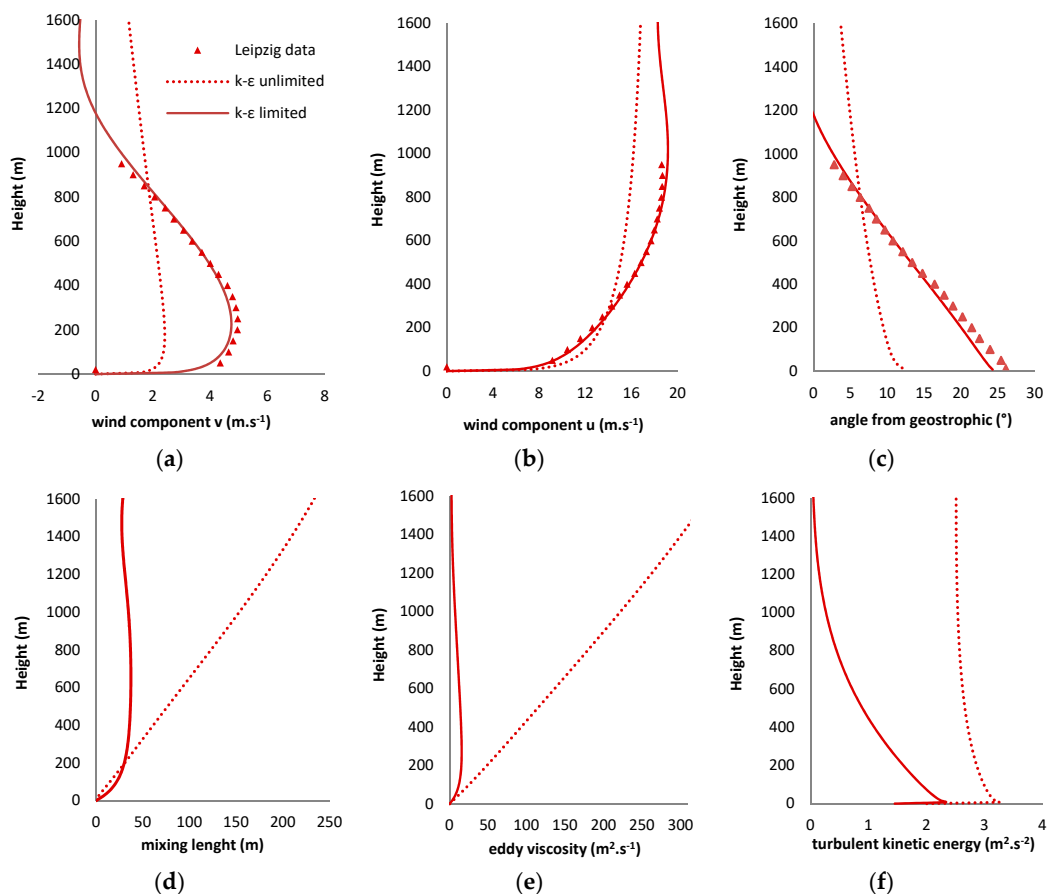


Figure 2. Vertical profile of the wind velocity component u (a), wind velocity component v (b), tuning of wind (c), mixing length (d), eddy viscosity (e) and turbulent kinetic energy (f).

The limited variant leads to turbulent kinetic energy and viscosity decreasing over the depth of the boundary layer while the standard variant shows a more or less linear increase causing a very

deep boundary layer (Figure 2d–f). Overall, this validation study shows that the limiting effect is significant. For the Leipzig test case, the limited $k - \varepsilon$ model yields results that have a better agreement with the observed profiles. Due to overestimation of the eddy viscosity with increasing height, the effects captured by the unlimited $k - \varepsilon$ model were underestimated.

3. Design of Experiments (DoE) Study

After verifying the capability of the model to reproduce the flow features in the ABL, the next step was to identify primary contributors to the wind flow at the WINSSENT test site. One of the main features of the test site is an escarpment covered by heterogeneous vegetation. The two planned test wind turbines, with a hub height of 75 m and a rotor diameter of 50 m will be installed approximately 200 m downstream of the forested escarpment and will be directly influenced by the canopy. Finding the impact of the forest height and density (which varies seasonally as the foliage grows and develops) on the wind flow can be assessed using a DoE approach. Combining CFD simulations with a DoE can be used to accurately rank the importance of the design parameters in a study [32] and can significantly reduce, for a real test site, the amount of simulated case and computational time. In our study, the influence of three parameters (namely the slope of the escarpment α , the LAI, and the forest height H) on the horizontal velocity, the flow inclination angle, and the turbulent kinetic energy at different locations, corresponding to the future position of the turbines was investigated. Table 3 lists the three parameters and their assigned values.

Table 3. Variables and their corresponding values used in the design of experiments (DoE) study.

Variable Level	Variables		
	Slope α (°)	Height H (m)	LAI
−1	15	20	2
+1	30	25	5

In order to apply the DoE, a simplified test case was defined as shown in Figure 3. The test case represents a simplification of the test site in two dimensions. We consider a 150 m high escarpment and the slope α to be of 15° or 30°, corresponding to a West and West-North-West wind direction. The escarpment is covered by a forest (green block in Figure 3).

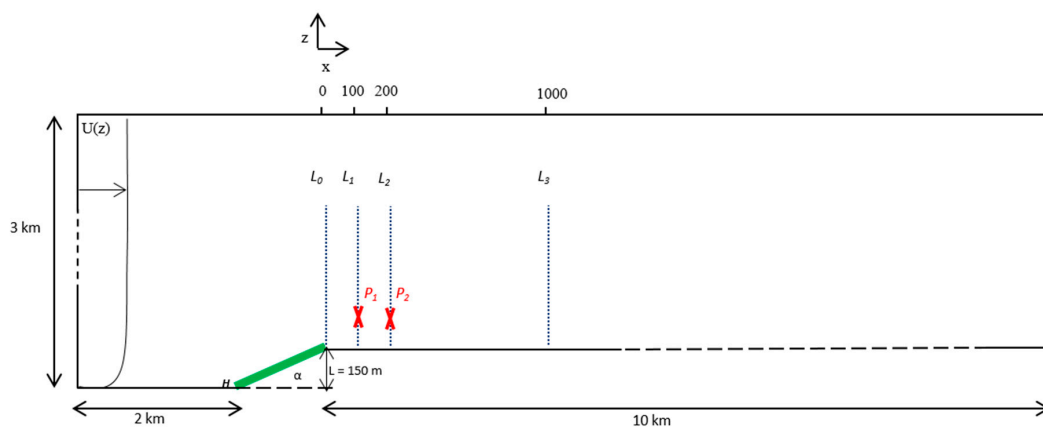


Figure 3. 2D geometry for the DoE study and the location of lines L_0 , L_1 , L_2 and L_3 , situated 0 m, 100 m, 200 m, and 1000 m downstream of the forested escarpment (green block), respectively.

In the real case, the separation between the forest and the ground is not as sharp, but rather shows a smooth transition. Several studies in the literature on the flow over an escarpment, including wind

tunnel, full-scale and simulations exist [33–35]. However, none of these studies presents results for a vegetated escarpment.

At the inflow, an empirical power law is used to describe the vertical wind profile as in [22]:

$$u(z) = u(z_r) \left(\frac{z}{z_r} \right)^a \quad (18)$$

where $\mu(z)$ is the average streamwise velocity at height z . $\mu(z_r) = 6 \text{ m}\cdot\text{s}^{-1}$ is the reference wind speed at the reference height $z_r = 80 \text{ m}$ and a is the power law exponent. This exponent depends on the surface roughness and the thermal stability parameter α . A value of 0.14 is taken as we assume the neutral case in this DoE study. It is worth mentioning that such a wind profile is an idealized one and is rarely found in a hilly complex terrain. However, our DoE study aims to assess the impact of modelling assumptions for a vegetated escarpment on certain parameters of interest and is not conducted in order to obtain the exact profiles at our specific test site with complex terrains.

We define the speed-up ratio S_u as being the mean wind speed at a height z above the ground divided by the mean wind speed of the undisturbed flow at the same height:

$$S_u = \frac{u(z)}{u_{undisturbed}(z)} \quad (19)$$

Similarly, we define S_k as the speed-up ratio for the turbulent kinetic energy as:

$$S_k = \frac{k(z)}{k_{undisturbed}(z)} \quad (20)$$

Speed-up ratio profiles for the wind speed downstream of the escarpment along L_0 , L_1 , L_2 and L_3 are presented in Figure 4. All the possible configurations of variables listed in Table 3 were simulated, and, additionally, the case of an escarpment with no canopy was simulated. The case without forest allows one to distinguish between the effect caused by the slope of the escarpment and the canopy. Figure 4 reveals the influence of the canopy, particularly up to 80 m above ground level (agl.). At L_0 , i.e., at the crest, the speed-up ratio shows a reduction in the velocity due to the drag effect generated by the forest, whereas for the case with no canopy, a strong acceleration of the flow can be seen. This effect is still perceptible 1 km downstream of the escarpment (at position L_3). The same observation was made in the work of [33]. There, a wind tunnel investigation of the flow over several escarpment shapes with a slope of 2:1 (26.7°) and 4:1 (14.0°) was performed. It was found that the region of influence of the escarpment persists $10 H$ (H being the escarpment height) downstream of the crest. The largest speed-up ratios were found close to the ground and decreased with increasing height for all cases. The location of the maximum moved upward as the flow proceeded downstream. The inclusion of a forest along the escarpment deflected the position of the maximum speed-up ratio S to higher altitudes. At L_1 , the position of the maximum of S_u located between 10 m and 20 m agl. with no canopy model, and between 80 m and 90 m agl. for the cases with a canopy. The maximum values of S , for a slope of 30° , are higher than in the case of 15° . For example, at L_1 , a maximum value of 1.33 and 1.26 was reached with a slope of 30° and 15° , respectively. This effect was reduced 1 km downstream of the crest, where a maximum of 1.27 and 1.24 was reached. For the same forest height (blue vs. red lines), as expected, a higher deceleration of the flow, i.e., lower value of S_u was observed for an LAI of 5 instead of an LAI of 2. All the positions, except the crest position, show an acceleration of the flow at the relevant heights for a wind turbine (between 80 m and 100 m agl.).

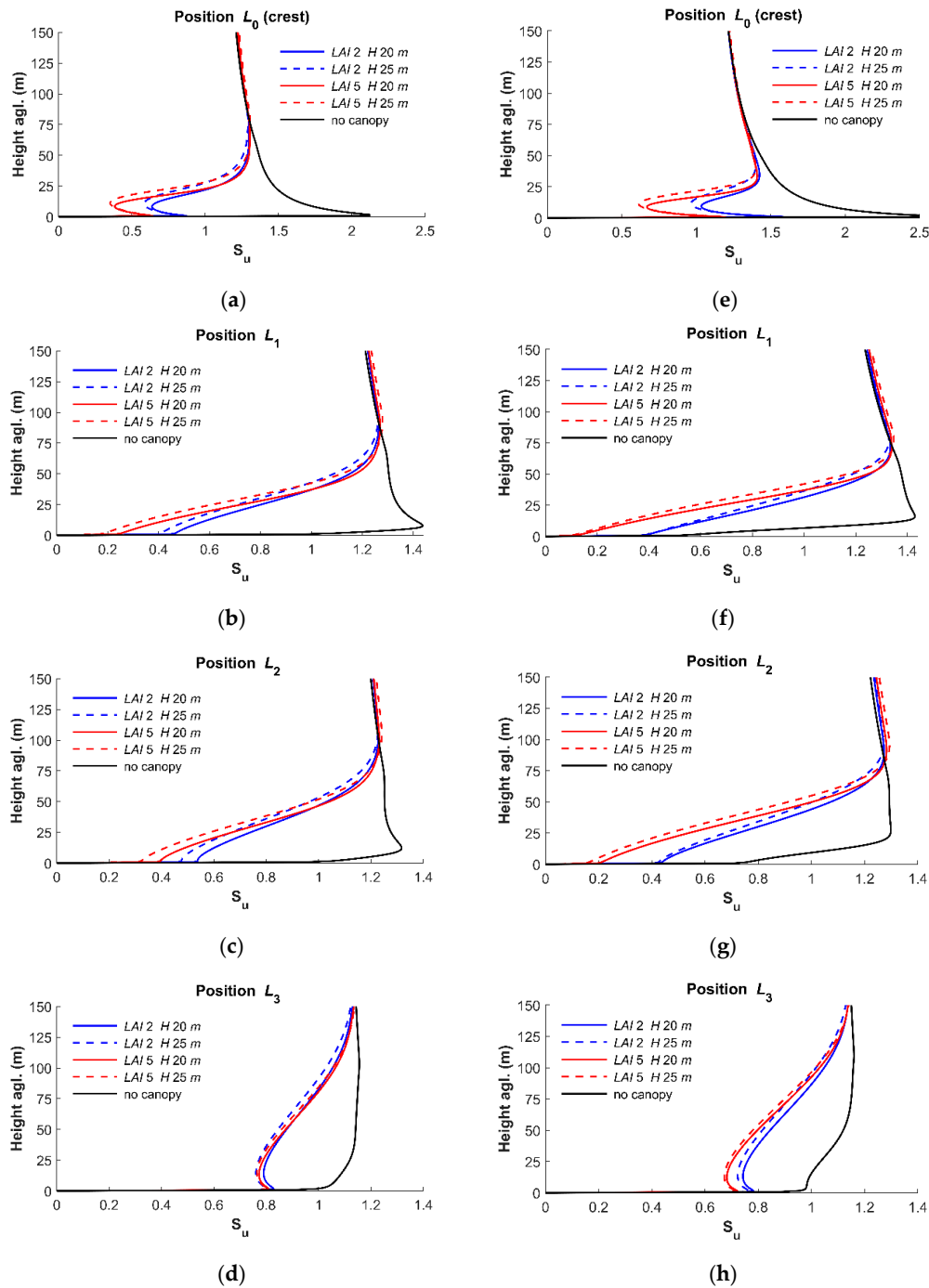


Figure 4. Speed-up profiles for the horizontal velocity at L_0 , L_1 , L_2 and L_3 position for an angle of 15° (a–d) and 30° (e–h). The red and blue curves are the simulation results with an LAI of 2 and 5, respectively. The solid and dashed lines indicate a forest height of 20 m and 25 m, respectively.

Figure 5 presents the results for the speed-up ratio for the turbulent kinetic energy speed, S_k . Speed-up ratio profiles for the turbulent kinetic energy are highly dependent on the canopy height and the LAI. The crest position (L_0) shows a maximum turbulent kinetic energy occurring near the top of the canopy and decaying rapidly above the forest. At position L_3 , the high turbulence levels indicate that the wake generated behind the crest was not dissipated. However, the case without forest seems to be almost recovered and suggests that the changes in the turbulent kinetic energy were only

due to the canopy. In general, the turbulent kinetic energy levels increased with the slope angle of the escarpment, but also with the forest height.

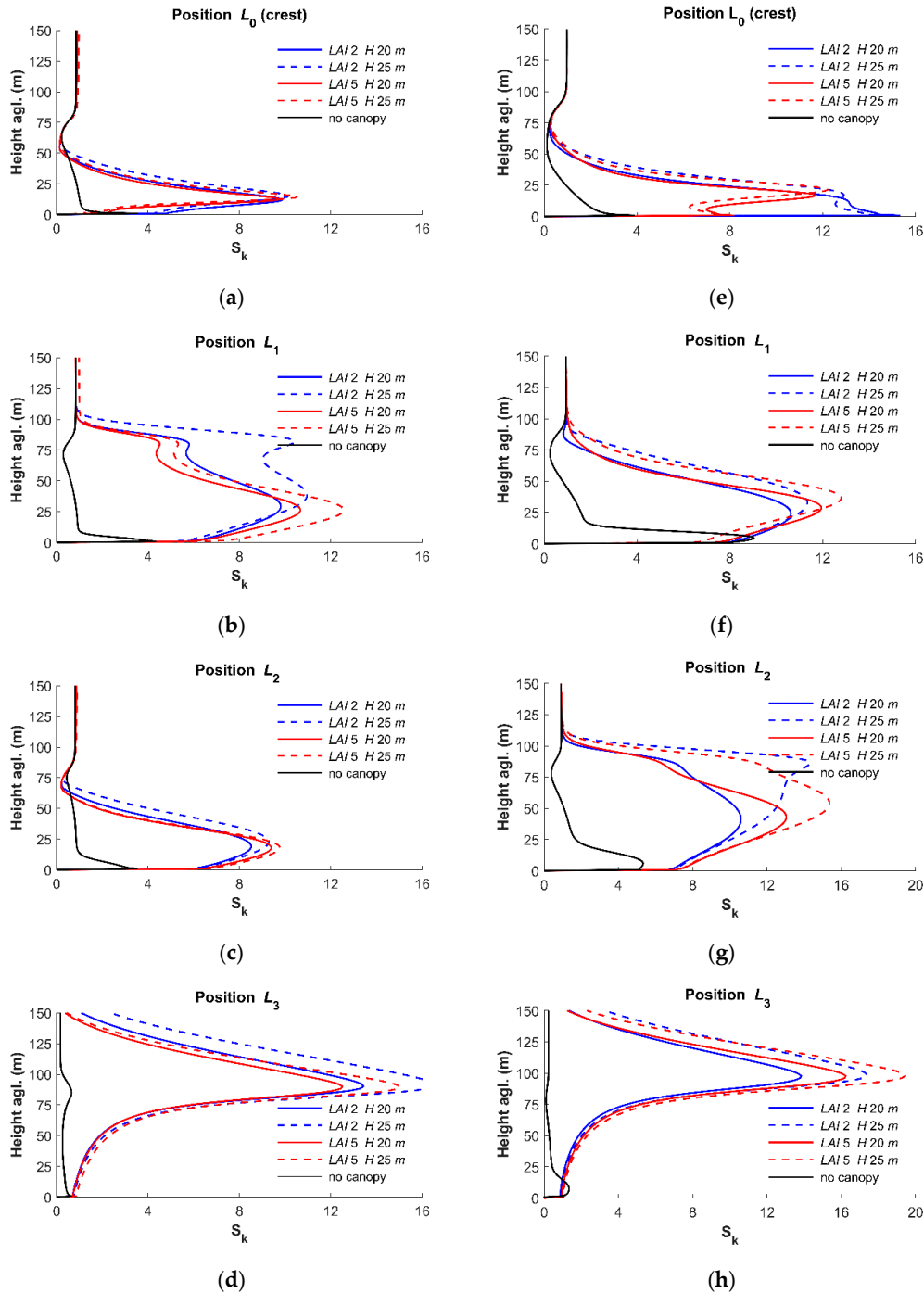


Figure 5. Speed-up profiles of the turbulent kinetic energy at L_0 , L_1 , L_2 , and L_3 position for an angle of 15° (a–d) and 30° (e–h). The red and blue curves are the simulation results with a LAI of 2 and 5, respectively. The solid and dashed lines indicate a forest height of 20 m and 25 m, respectively.

The results of the DoE on the 2D escarpment are shown in Figures 6–8. The DoE method was applied at two points, P_1 and P_2 , located at different altitudes (50 m, 75 m, and 100 m agl.) on the lines

L_1 and L_2 . The absolute effects of each factor, listed in Table 3, on the horizontal velocity, the inclination angle and the turbulent kinetic energy were evaluated. A similar behaviour for the horizontal velocity (Figure 6) and the flow inclination angle (Figure 7) can be seen: the main variability in the response is dominated by the slope of the escarpment. This becomes even more evident for the flow inclination angle. The effect of the forest height H or the leaf area index LAI remains small relative to the slope, except for the lowest positions at 50 m agl., where the forest height parameter can exceed the same absolute value as the angle (Figure 6). Generally, as we go further downstream of the escarpment (P_1 vs. P_2), the effect for the three parameters becomes smaller. The response for the turbulent kinetic energy k was different. The forest height, followed by the LAI , was as important as the slope at lower levels. All the effects were then dissipated at 100 m agl.

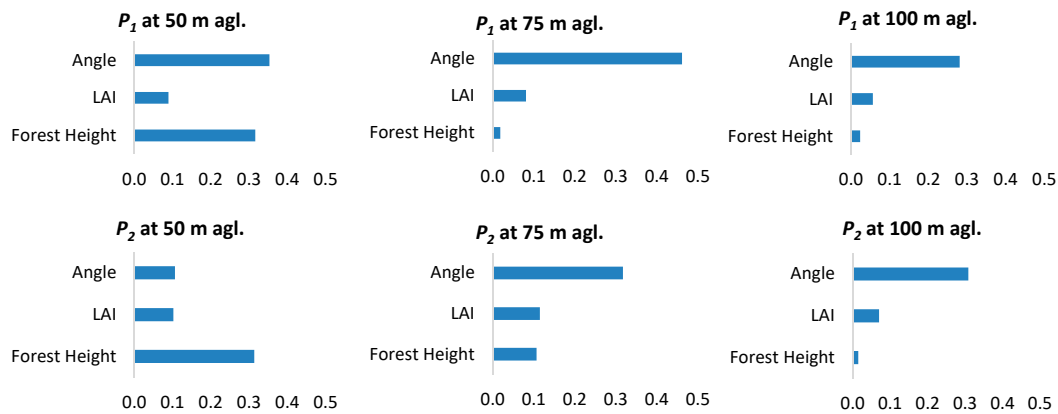


Figure 6. Pareto chart of effects for the horizontal velocity at different altitudes on L_1 and L_2 .

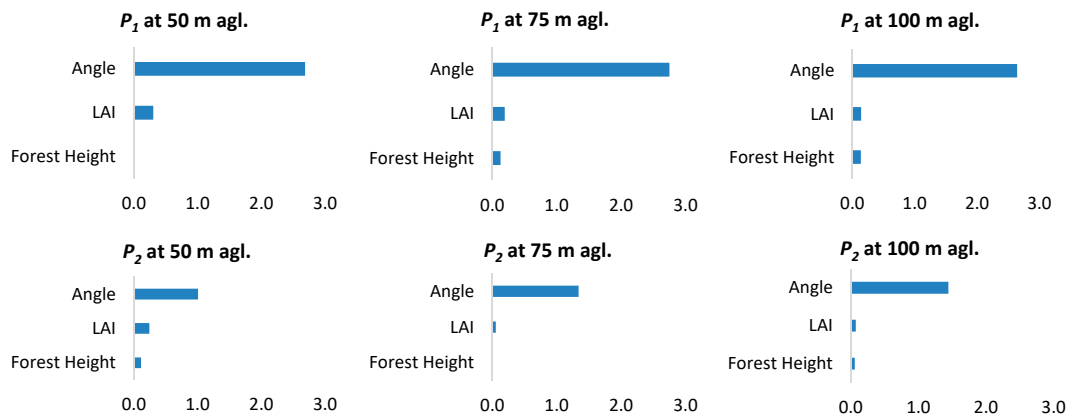


Figure 7. Pareto chart of effects for the flow inclination angle at different altitudes on L_1 and L_2 .

Considering a turbine hub-height of 75 m and the top of the rotor blade located at 100 m agl., this parametric study shows that the primary contributor was generally the angle, i.e., for the test site, the wind direction. The forest height H and LAI play a significant role only at 50 m agl. This is in accordance with the results from Figure 4, where the main differences for all the configurations were only perceptible in the lower levels. For the simulations of the WINSSENT test site, described in Section 4.1, a sensitivity analysis using the same parameter values will be conducted.

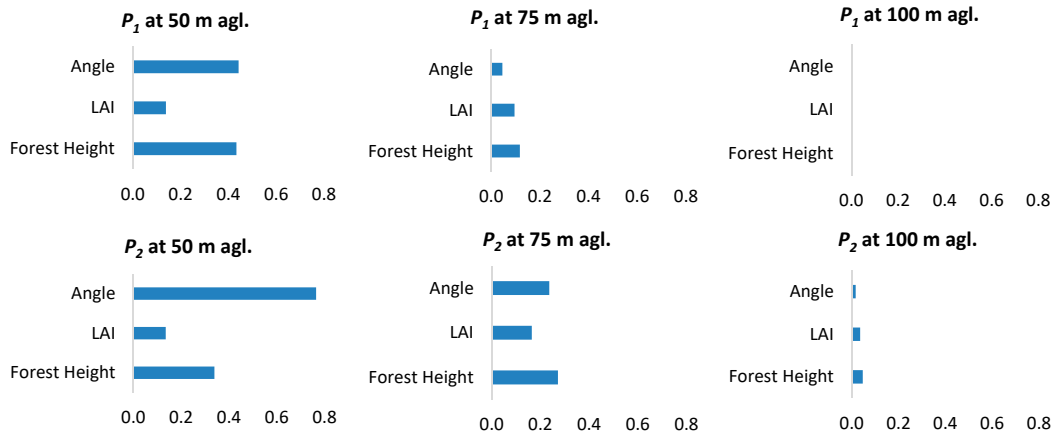


Figure 8. Pareto chart of effects for the turbulent kinetic energy at different altitudes on L_1 and L_2 .

4. WINSENT Test Site Overview and Measurement Techniques

4.1. Site Description

The test site is located in the Swabian Alb in Southern Germany. The main feature of the site is an escarpment up to 200 m in height with respect to the valley (Figure 9). The escarpment is characterized by a very steep slope of around 30° from the Northwest and a more gradual slope at around 15° further west. The escarpment is covered by a deciduous forest. Downstream, it is essentially flat with an agriculturally used land. Measurements from the German Meteorological Service at Stötten (734 m a.s.l., 48.6657° latitude, 9.8646° longitude), located approximately 2 km upstream of the escarpment, indicate a westward wind direction for most of the year. This wind direction makes the test site interesting in the sense that the predominant wind direction is perpendicular to the escarpment. More details about the WINSENT test site can be found in [36].

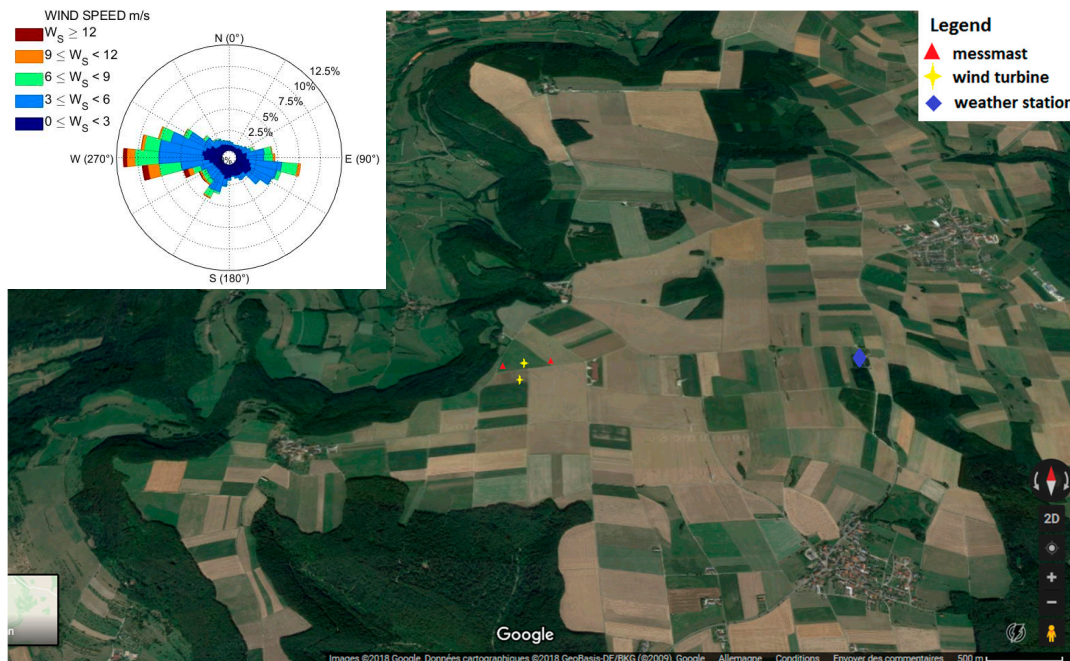


Figure 9. Overview of the test site and the wind rose generated from a cup anemometer at 10 m agl. at the weather station of Stötten for the time frame 2016–2017.

4.2. Description of the Experiment Setup

The field measurements were carried out on the top of the plateau, over and downstream of the escarpment using the multipurpose airborne sensor carrier (MASC) operated by the Environmental Physics group at the University of Tübingen, Germany. The MASC is a UAS which can resolve turbulent fluctuations of wind and temperature with a resolution of about 30 Hz. The wind measurement was performed by measuring the flow speed and flow angles at the aircraft nose with a multi-hole flow probe. Typical absolute errors in wind speed for the sensors mounted on the MASC are of the order of $\pm 0.5 \text{ m}\cdot\text{s}^{-1}$ (for more information, see [4,5,37,38]). In order to measure the three-dimensional flow field at the test site, a vertical grid of racetracks with legs going back and forth over the test site was performed. The wind speed measurements were then averaged over subsections of 20 m in length along each leg. Each racetrack consisted of two horizontal straight flight legs, one in the flow direction and the second one going against the wind direction. The legs against the wind direction had a higher spatial resolution and thus were used for comparison with the simulation results.

In the present study, we consider the date 27 March 2015. The site was dominated by dry weather, almost neutral ABL, and a northwest wind (290° at the nearby weather station of Stötten during the measuring time). A vertical grid of the racetrack flight pattern with vertical steps of 25 m was performed between 13:00 and 16:00 UTC. The lowest and the highest flight heights were 75 m and 275 m agl., respectively. Two racetracks were flown at each height. In total, three flights with a duration of one hour each were carried out between 13:00 and 16:00. Figure 10 shows a three-dimensional view of the flight path performed by the MASC. The flight path covers the upstream and downstream region of the escarpment.

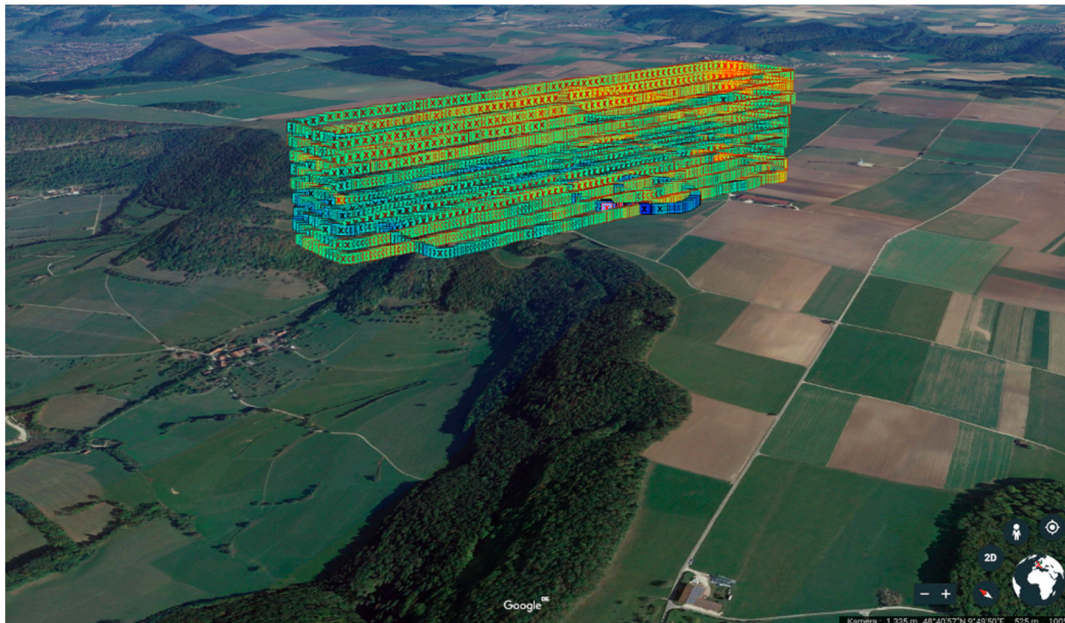


Figure 10. Flight paths (racetracks) performed on the 27 March 2015. The colors indicate the measured horizontal velocity.

5. Simulation of the WINSSENT Test Site

5.1. CFD Settings for the Test Site

The simulations were conducted on two nested domains with varying size and spatial resolution. A parent domain of $20 \text{ km} \times 20 \text{ km} \times 2 \text{ km}$ and a nested domain of $5 \text{ km} \times 5 \text{ km} \times 1.5 \text{ km}$, centred on the escarpment, were defined. The terrain data was based on the digital terrain model DTM from

the Baden-Württemberg Authorities for Spatial Information and Rural Development (LGL) with a spatial resolution of 5 m. A horizontal grid resolution of 25 m was provided for the first domain and a finer resolution of approximately 7 m was provided for the small domain (cf. Table 4). A volume mesh, finer near the ground and conforming to the site orography, was constructed for the domains using SnappyHexMesh, the mesh generator of OpenFOAM. Details of meshes can be found in Table 4. Additionally, the digitized landscape model DLM from LGL was utilized to describe the land cover on the Earth’s surface. Three classes of land uses were used for this study: urban, ground, and forest (Figure 11). The urban and the ground classes were assigned values of $z_0 = 0.50$ m and $z_0 = 0.02$ m for the aerodynamic roughness length. A no-slip boundary condition was used for the velocity. A sensitivity analysis using several LAI values and forest height was conducted (cf. Table 5). The source terms, associated with the forest, as described in Equations (14)–(16), were applied to all cells, which were located below the top of the forest canopy.

Table 4. Mesh resolutions for the domains.

Mesh Properties	Number of Cells	Maximum Cell Size	Horizontal Resolution at the Ground	Vertical Resolution at the Ground
Basis	66.8 million	100 m	25 m	2.6 m
Nested	25.4 million	50 m	6.75 m	1.2 m

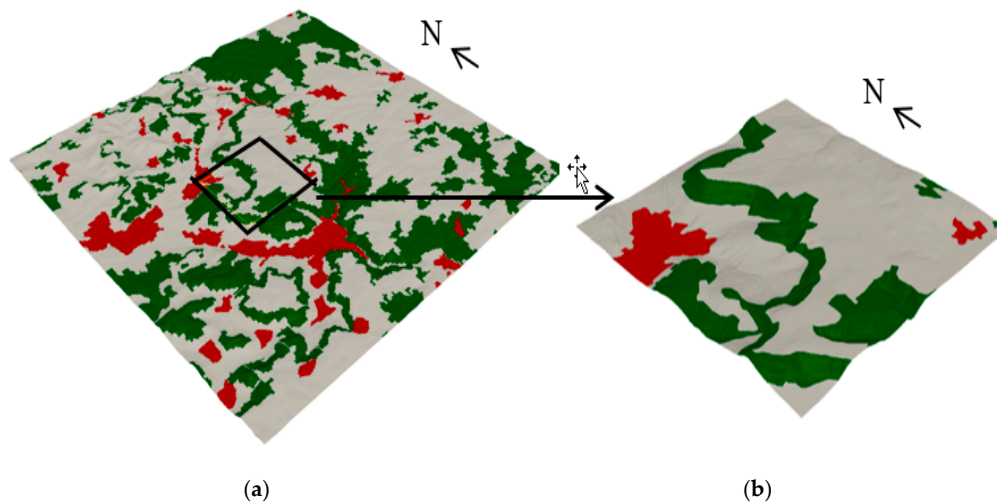


Figure 11. Big domain 20 km \times 20 km (a). The color indicates the type of classes used in the simulation: red for urban, grey for ground, and green for forest. The black box shows the position of the small domain 5 km \times 5 km (b).

Table 5. Summary of simulations run to investigate the sensitivity of the model to the LAI and forest height H .

Run	LAI	Forest Height H (m)
Run 1 (no canopy)	0	0
Run 2	2	20
Run 3	2	25
Run 4	5	20
Run 5	5	25

For the nested domain, boundary conditions were extracted from the solution of the parent domain. The parent domain was initialized using input data from the COSMO-DE (Consortium for Small-scale Modeling) weather model of the German Weather Service (DWD, [23]). COSMO-DE has a

horizontal resolution of $2.8 \text{ km} \times 2.8 \text{ km}$ and 20 vertical levels in the lower 3000 m of the computational domain. Only hourly data are delivered by the DWD. These data provide the wind components, pressure, air and surface temperature, as well as the turbulent kinetic energy. A time-slice approach was used in order to join the COSMO-DE and the CFD model. In this method, the boundary conditions for the simulation were based on one specific time slice from the COSMO-DE weather model: 27 March 2015, 15:00 UTC.

5.2. Numerical Results

In order to gain a better understanding of the wind flow at Stötten, a global view of the flow pattern at different heights agl. is presented in Figure 12. An additional black line corresponding to the legs performed by the UAS at the same altitude was added. These legs have a length of approximately 1 km. The large differences in the velocity contour plots highlight the complexity of the flow with high gradients of wind speed, especially at lower levels. A high speed-up zone along the escarpment can be seen. This speed-up extends downstream of the escarpment but not uniformly.

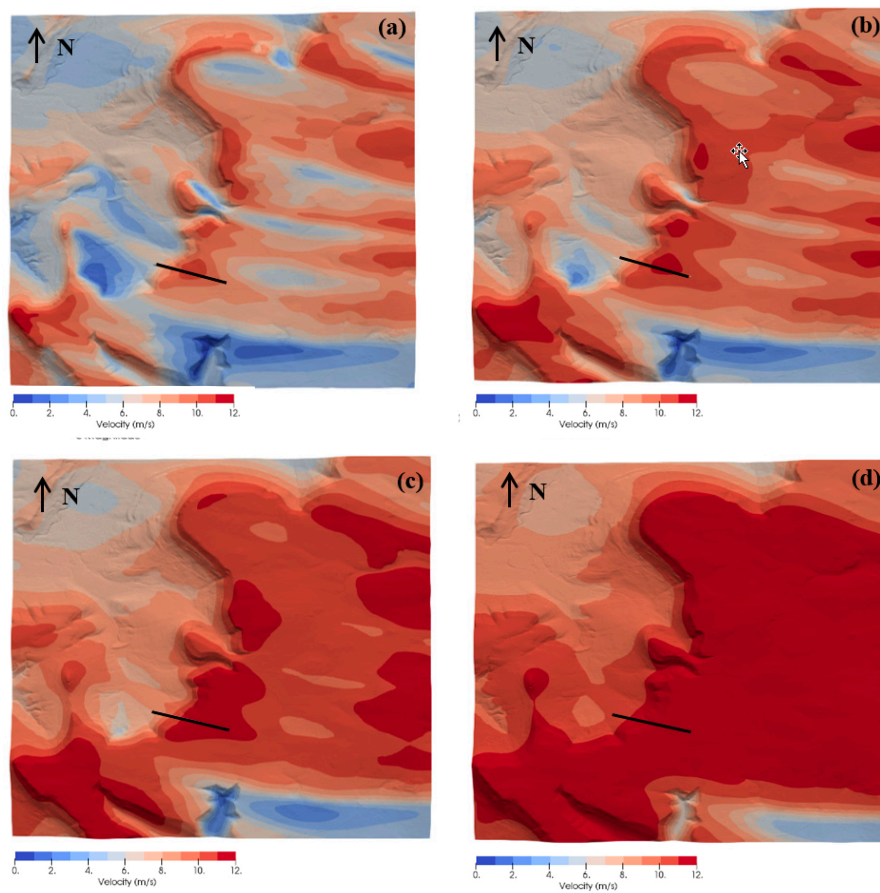


Figure 12. Velocity contour plots for leaf area index ($LAI = 2$) and $h = 20 \text{ m}$ at 75 m (a), 125 m (b), 175 m (c) and 275 m (d) agl. on the 27 March 2015. The black lines correspond to the UAS flight path.

For the evaluation of the results, the quantities will be plotted along a horizontal line, corresponding to the performed flight path and three vertical lines (Figure 13). Error bars, corresponding to one standard deviation, were inserted for the UAS measurements.

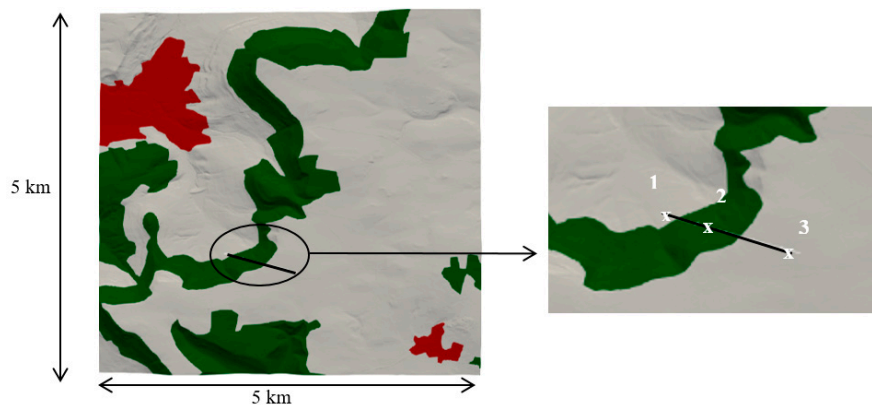


Figure 13. Position of the horizontal (black line) and vertical (1, 2 and 3) lines for the evaluation related to Figures 14 and 15.

Figure 14 shows the horizontal wind speed and the flow inclination angle at the same altitudes as those presented in Figure 12. The modelled and measured values are in good agreement, although the profile shape of the modelled wind speed at higher levels is slightly over predicted (up to $2 \text{ m}\cdot\text{s}^{-1}$) relative to the UAS measurements. The simulation results and measurements show a horizontal profile which is becoming flat with increasing height. This can be explained by the flow becoming more homogeneous with increasing altitude and no longer being influenced by the terrain. At a height of 75 m, the UAS recorded the maximum wind speed at a distance of around 500 m. The simulation predicts a maximum at the same position. This maximum corresponds to the area over the escarpment with a speed-up as shown in the velocity contour plot in Figure 12a,b. This maximum was shifted to the east with increasing altitude, in accordance with the DoE study. At 125 m height, the maximum was located at a distance of 600 m according to the model. The position of this maximum cannot be seen in the measurement data. Figure 14 shows that using a forest height of 25 m lead to a positive velocity bias, except at the lower level of 75 m, where the velocity was reduced. By comparing the results with different LAI values (blue vs. red lines), we see that the foliage density does not have an impact on the horizontal wind speed. At a height of 275 m, the impact of the canopy and the escarpment was strongly reduced: all the canopy variants converge to a similar profile, with the differences getting smaller.

Flow angles, measured by the UAS and predicted by the simulation, indicate a complex flow near the escarpment. Figure 14 shows the flow inclination angles to have a non-constant profile. Such a change in the inclination angle is due to a local phenomenon induced by local features of the terrain. It is noticeable that, for the first two-thirds of the flight path, positive flow angles of up to 10 degrees were reached. This position corresponds to the area located upwind and over the escarpment that is dominated by updrafts. The flow inclination angle becomes smaller with increasing height, indicating that the wind was less deflected by the orography. At a height of 75 m, zero inclination angles appear at a distance of around 800 m for the simulation and 700 m for the measurements. At higher levels, the model no longer predicts large positive values but angles approaching a zero value, indicating a flow that is rather horizontal. In accordance with the simulation results, the UAS also reports zero-angle values at the highest level. Upon observation of the different parametrization of the forest, no significant differences were found. This is in accordance with the 2D DoE study, where the effect on the inclination angle was largely dominated by the slope of the escarpment.

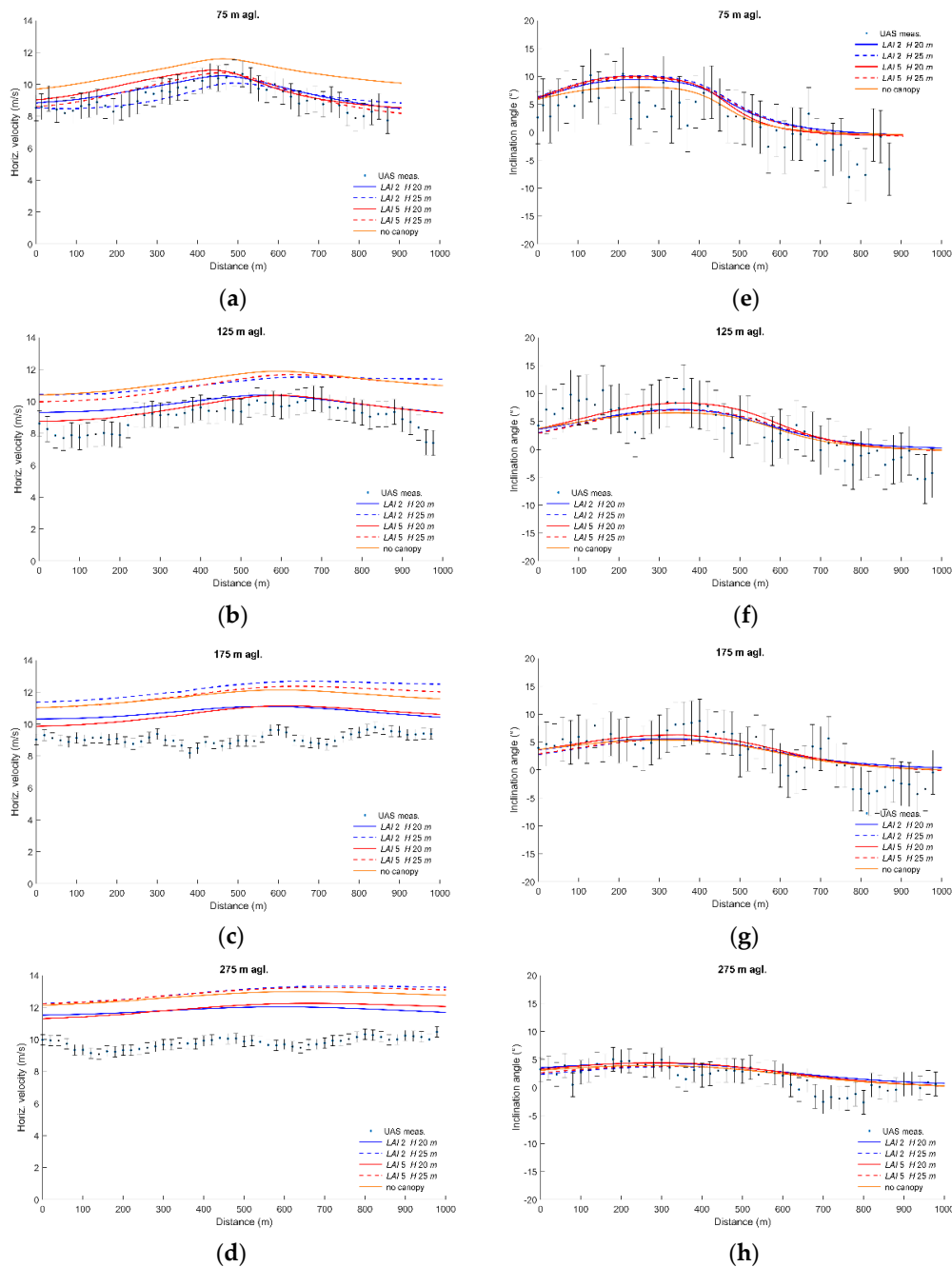


Figure 14. Horizontal velocity (a–d) and inclination angle (e–h) at 75 m, 125 m, 175 m, and 275 m agl. on the 27 March 2015. The dots are the UAS measurements and the lines of the simulation results. The colors represent the different values of LAI and height for the forest.

Figure 15 presents the vertical profiles of the horizontal velocity and the turbulent kinetic energy at three positions along the flight path. The first position was located a few meters upstream the forest, the second one in the canopy and the last one approximately 300 m downstream of the escarpment (Figure 13). The plots confirm the overprediction of the model relative to the measurements at the upper levels. At position 1, i.e., upwind of the escarpment, the flow seems to already be decelerated. At position 2, the velocity profile shows an inflexion point in the lower height due to the explicit integration of the forest in our model. The effect of the escarpment and forest can be detected even at

position 3; however, the profile becomes more uniform with increasing height. This feature is almost too difficult to observe in the UAS data due to the low resolution in the vertical direction. The strong shear, observed in the horizontal velocity profiles, indicated that there is a large amount of turbulence generated by vertical wind shear. Looking at the profiles of the turbulent kinetic energy, the modelled and observed values of the turbulent kinetic energy decreased with increasing height and attain their maximum values in the region of strong wind shear. The turbulent kinetic energy profiles were highly dependent on the canopy model. Upstream of the escarpment, the maximum simulated value was located at 100 m agl. At position 2, this maximum occurred at approximately 20 m agl., i.e., at the top of the forest, where a large portion of the turbulent kinetic energy was produced, due to high shear and shear-stress. Downstream of the escarpment, this maximum was carried to the upper heights with values between 3.5 and 4.0 $\text{m}^2\cdot\text{s}^{-2}$ at a height of 40 m in the model. The UAS measurement also showed an increasing turbulence value of 2.4 $\text{m}^2\cdot\text{s}^{-2}$ at a height of 75 m.

Due to a low vertical spatial resolution in the measurements, it is difficult to determine the location and the intensity of this maxima. The simulation results show that the location of this maximum can be critical as it is approaching the bottom of the rotor plane of the future wind turbine. The turbulent kinetic energy profiles obtained at position 3 were the result of a flow which has been decelerated but, in the meantime, production of turbulent kinetic energy near the canopy top was generated.

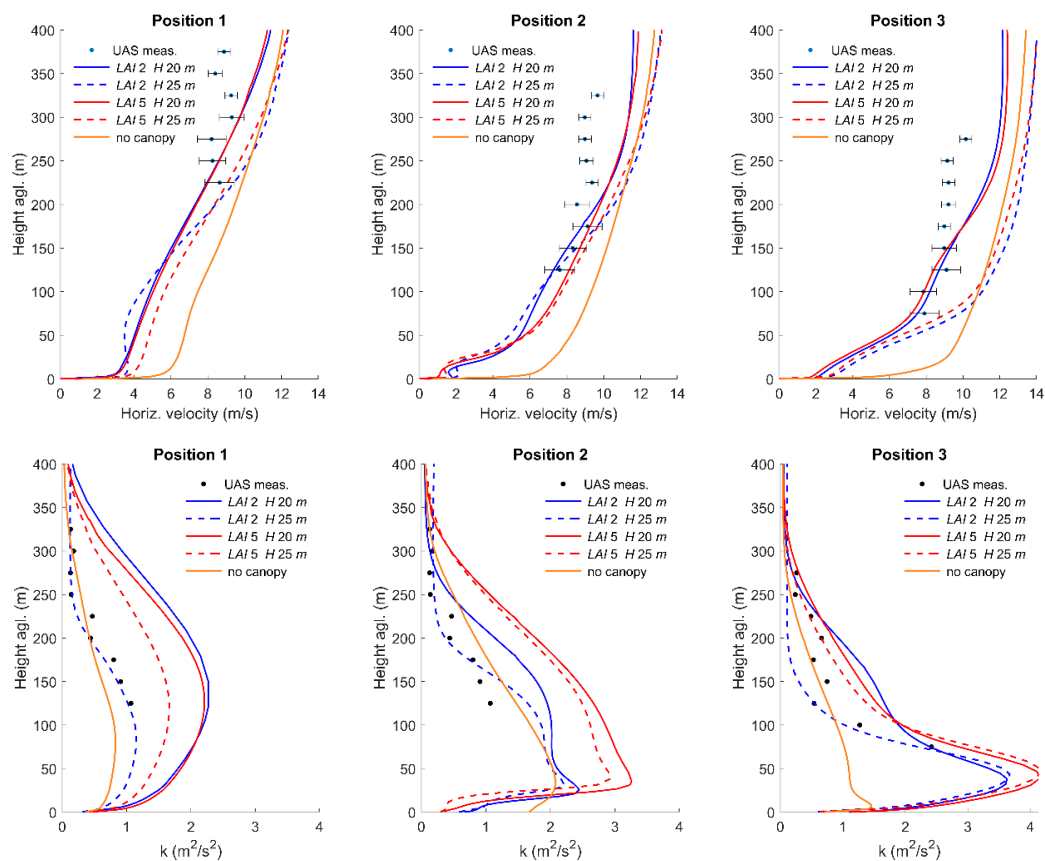


Figure 15. Vertical profiles of the horizontal velocity and the turbulent kinetic energy at three positions on the 27 March 2015. The dots are the UAS measurements and lines of the simulation results. The colors represent the different values of LAI and height for the forest.

6. Summary and Conclusions

This study aimed to assess whether or not our model can reproduce relevant features of the flow. The results show the potential of the proposed model based on the Boussinesq approximation and

considering the Coriolis effect. The implementation of a limited version of the $k - \varepsilon$ model has been successfully applied to predict the Leipzig experiment profiles. The limited $k - \varepsilon$ model consists of reducing C_{μ} to 0.0256 and to make the production of ε as a function of height. The Coriolis force introduces a velocity component v perpendicular to the direction of the geostrophic wind and causes a turning in the wind. The limiting effect successfully reproduces the Leipzig profile by generating a surface wind turned value close to the experimental one, while the standard $k - \varepsilon$ model obtains about half the limited value.

In the second step, we analyzed the flow on a 2D case of the escarpment. The focus was to understand the impact of the slope of the escarpment, the forest height, and the leaf area density on the horizontal velocity, the flow inclination angle, and the turbulent kinetic energy at turbine-relevant heights. A DoE was applied to the simulation results and showed that the primary contributor is the slope of the escarpment, i.e., for the test site, the wind direction. For the wind speed, it was found that the forest height and LAI plays a minor role in comparison to the slope of the escarpment. However, for the turbulent kinetic energy, we showed that the LAI and canopy height is as important as the escarpment slope.

In the final step, the simulations were performed on the WINSENT test site. The aim of the study was to evaluate the accuracy of a modified version of $k - \varepsilon$ model in complex terrain. A validation against UAS measurements was performed. For the computation, the boundary conditions were derived from the mesoscale COSMO-DE model. Despite the low resolution of the COSMO-DE model, the one-way coupling method works well in complex terrain. The microscale model captures the varying pattern in the test site, such as the deceleration of the wind speed, the upward flow, and the increased turbulent kinetic energy in the lower levels. Generally, a good agreement was found in the lower levels (75 m and 125 m agl.) but discrepancies between the simulated results and the UAS measurements were found at upper levels. While the model shows enhanced absolute turbulent values in the lower altitudes, the measurements could not confirm the location of this maximum due to a low vertical resolution. Measurement campaigns with low flight heights, down to 20 m, are planned and will confirm or disprove the region of high turbulences. A remark on the stability should be mentioned. The assumption of an almost neutral ABL in our study was considered by checking the potential temperature profiles from UAS measurements (between 50 m and 300 m above the ground). This is also true at those levels, but only measurements near the ground could confirm the flow stratification. However, we have to recognize that it was likely a convective ABL and we should acknowledge that limitation in the paper. Additional measurement systems, such as Lidar, an eddy-covariance micro-meteorological station, and a tower equipped with an anemometer are going to be installed permanently on the test site, a few meters on the upwind and downwind side of the escarpment. This will also enable the attainment of values in lower levels and further valuable data for characterizing the flow and its stratification at the WINSENT test site.

The thermal stratification has a large impact on the vertical wind profile and turbulence levels. Therefore, different thermal stratification cases will be conducted in future studies when the complete measurement set up will be running. For a better comparison of UAS measurements and simulation results, the one-way coupling method with only one time step will be replaced by transient outputs from a mesoscale model.

Author Contributions: All the authors have substantial contribution to this work.

Funding: This publication was made possible through the collaboration in the WindForS wind energy research cluster. The authors acknowledge the State of Baden-Württemberg through bwHPC for providing computational resources and the German Federal Ministry for Economic Affairs and Energy for funding measurement campaigns in the framework of the German joint research projects Lidar complex (grant number 0325519) and KonTest (grant number 0325665), as well of the simulations within WINSENT (grant number 0324129).

Conflicts of Interest: The authors declare no conflict of interest.

References

1. Fraile, D.; Tardieu, P. *Wind in Power 2017—Annual Combined Onshore and Offshore Wind Energy Statistics*; WindEurope: Brussels, Belgium, 2018; p. 25.
2. Hofsäß, M.; Clifton, A.; Cheng, P.W. Reducing the Uncertainty of Lidar Measurements in Complex Terrain Using a Linear Model Approach. *Remote Sens.* **2018**, *10*, 1465. [[CrossRef](#)]
3. Wildmann, N.; Höfsäß, M.; Weimer, F.; Joos, A.; Bange, J. MASC—A small Remotely Piloted Aircraft (RPA) for wind energy research. *Adv. Sci. Res.* **2014**, *11*, 55–61. [[CrossRef](#)]
4. Wildmann, N.; Bernard, S.; Bange, J. Measuring the local wind field at an escarpment using small remotely-piloted aircraft. *Renew. Energy* **2017**, *103*, 613–619. [[CrossRef](#)]
5. Rautenberg, A.; Graf, M.; Wildmann, N.; Platis, A.; Bange, J. Reviewing Wind Measurement Approaches for Fixed-Wing Unmanned Aircraft. *Atmosphere* **2018**, *9*, 422. [[CrossRef](#)]
6. Sykes, R.I. An asymptotic theory of incompressible turbulent boundarylayer flow over a small hump. *J. Fluid Mech.* **1980**, *101*, 647–670. [[CrossRef](#)]
7. Mason, P.J.; King, J.C. Measurements and predictions of flow and turbulence over an isolated hill of moderate slope. *Q. J. R. Meteorol. Soc.* **1985**, *111*, 617–640. [[CrossRef](#)]
8. Taylor, P.A. Some numerical studies of surface boundary-layer flow above gentle topography. *Bound.-Layer Meteorol.* **1977**, *11*, 439–465. [[CrossRef](#)]
9. Jackson, P.S.; Hunt, J.C.R. Turbulent wind flow over a low hill. *Q. J. R. Meteorol. Soc.* **1975**, *101*, 929–955. [[CrossRef](#)]
10. Rodrigo, J.S.; Arroyo, R.A.C.; Moriarty, P.; Churchfield, M.; Kosovic, B.; Rethore, R.-E.; Hansen, K.S.; Hahmann, A.; Mirocha, J.D.; Rife, D. Mesoscale to microscale wind farm flow modeling and evaluation. *WIREs Energy Environ.* **2017**, *6*, e214. [[CrossRef](#)]
11. Berg, J.; Mann, J.; Bechmann, A.; Courtney, M.S.; Jørgensen, H.E. The Bolund experiment, part I: Flow over a steep, three-dimensional hill. *Bound.-Layer Meteorol.* **2011**, *141*, 219. [[CrossRef](#)]
12. Bechmann, A.; Sørensen, N.N.; Berg, J.; Mann, J.; Rethore, P.-E. The Bolund Experiment, Part II: Blind Comparison of Microscale Flow Models. *Bound.-Layer Meteorol.* **2011**, *141*, 245–271. [[CrossRef](#)]
13. Lange, J.; Mann, J.; Berg, J.; Parvu, D.; Kilpatrick, R.; Costache, A.; Jubayer, C.; Hangan, H. For wind turbines in complex terrain, the devil is in the detail. *Environ. Res. Lett.* **2017**, *12*, 094020. [[CrossRef](#)]
14. CORINE Land Cover—Copernicus Land Monitoring Service. Available online: <https://land.copernicus.eu/pan-european/corine-land-cover> (accessed on 11 February 2019).
15. Jimenez, P.A.; Navarro, J.; Palomares, A.M.; Dudhia, J. Mesoscale modeling of offshore wind turbine wakes at the wind farm resolving scale: A composite-based analysis with the Weather Research and Forecasting model over Horns Rev. *Wind Energy* **2015**, *18*, 559–566. [[CrossRef](#)]
16. Khani, S.; Porté-Agel, F. A Modulated-Gradient Parametrization for the Large-Eddy Simulation of the Atmospheric Boundary Layer Using the Weather Research and Forecasting Model. *Bound.-Layer Meteorol.* **2017**, *165*, 385–404. [[CrossRef](#)]
17. Schlünzen, H.K.; Grawe, D.; Bohnenstengel, S.I.; Schlüter, I.; Koppmann, R. Joint modelling of obstacle induced and mesoscale changes—Current limits and challenges. *J. Wind Eng. Ind. Aerodyn.* **2011**, *99*, 217–225. [[CrossRef](#)]
18. Zajaczkowski, F.; Haupt, S.; Schmehl, K. A preliminary study of assimilating numerical weather prediction data into computational fluid dynamics models for wind prediction. *J. Wind Eng. Ind. Aerodyn.* **2011**, *99*, 320–329. [[CrossRef](#)]
19. Knaus, H.; Höfsäß, M.; Rautenberg, A.; Bange, J. Application of Different Turbulence Models Simulation Wind Flow in Complex Terrain: A Case Study for the WindForS Test Site. *Computation* **2018**, *6*, 25. [[CrossRef](#)]
20. Knaus, H.; Rautenberg, A.; Bange, J. Model comparison of two different non-hydrostatic formulations for the Navier-Stokes equations simulationg wind flow in complex terrain. *J. Wind Eng. Ind. Aerodyn.* **2017**, *169*, 290–307. [[CrossRef](#)]
21. Weller, H.G.; Tabor, G.; Jasak, H.; Fureby, C. A tensorial approach to computational continuum mechanics using object-oriented techniques. *Comput. Phys.* **1998**, *12*, 620–631. [[CrossRef](#)]
22. Etling, D. *Theoretische Meteorologie*; Springer: Berlin, Germany, 2008; ISBN 978-3-540-75978-2.
23. Doms, G.; Baldauf, M. *A Description of the Nonhydrostatic Regional COSMO-Model. Part I: Dynamics and Numerics*; Consortium for Small-Scale Modelling (COSMO): Offenbach, Germany, 2018; p. 158.

24. Dudhia, J. A Nonhydrostatic Version of the Penn State–NCAR Mesoscale Model: Validation Tests and Simulation of an Atlantic Cyclone and Cold Front. *Monthly Weather Rev.* **1993**, *121*, 1493–1513. [[CrossRef](#)]
25. Apsley, D.D.; Castro, I.P. A limited-length-scale $k-\epsilon$ model for the neutral and stably-stratified atmospheric boundary layer. *Bound.-Layer Meteorol.* **1997**, *83*, 75–98. [[CrossRef](#)]
26. Detering, H.W.; Etling, D. Application of the $k-\epsilon$ turbulence model to the atmospheric boundary layer. *Bound.-Layer Meteorol.* **1985**, *33*, 113–133. [[CrossRef](#)]
27. Pena, A.; Gryning, S.-E.; Mann, J.; Hasager, C.B. Length scales of the neutral wind profile over homogeneous terrain. *J. Appl. Meteorol. Climatol.* **2010**, *49*, 792–806. [[CrossRef](#)]
28. Blackadar, A.K. The vertical distribution of wind and turbulent exchange in a neutral atmosphere. *J. Geophys. Res.* **1962**, *67*, 3095–3102. [[CrossRef](#)]
29. Launder, B.E.; Spalding, D.B. The numerical computation of turbulent flows. *Numer. Predict. Flow Heat Transf. Turbul. Combust.* **1974**, *3*, 269–289. [[CrossRef](#)]
30. Katul, G.G.; Larry, M.; Sanz, C. one- and two-equation models for canopy turbulence. *Bound.-Layer Meteorol.* **2004**, *113*, 81–109. [[CrossRef](#)]
31. Lettau, H. A Re-examination of the “Leipzig Wind Profile” Considering some Relations between Wind and Turbulence in the Frictional Layer. *Tellus* **1950**, *2*, 125–129. [[CrossRef](#)]
32. Elder, R.; Tourlidakis, A.; Yates, M. *Advances in CFD in Fluid Machinery Design*; Wiley: Hoboken, NJ, USA, 2003; ISBN 978-1-86058-353-7.
33. Bowen, A.J.; Lindley, D. A wind-tunnel investigation of the wind speed and turbulence characteristics close to the ground over various escarpment shapes. *Bound.-Layer Meteorol.* **1977**, *12*, 259–271. [[CrossRef](#)]
34. Jensen, N.O.; Peterson, E. On the escarpment wind profile. *Q. J. R. Meteorol. Soc.* **1978**, 719–728. [[CrossRef](#)]
35. Emeis, S.; Frank, H.; Fiedler, F. Modification of air flow over an escarpment—Results from the Hjärdemal experiment. *Bound.-Layer Meteorol.* **1994**, *74*, 131–161. [[CrossRef](#)]
36. WINSSENT—WindForS. Available online: <https://www.windfors.de/en/projects/test-site/winsent/> (accessed on 5 February 2019).
37. Wildmann, N.; Rau, G.A.; Bange, J. Observations of the Early Morning Boundary-Layer Transition with Small Remotely-Piloted Aircraft. *Bound.-Layer Meteorol.* **2015**, *157*, 345–373. [[CrossRef](#)]
38. Rautenberg, A.; Allgeier, J.; Jung, S.; Bange, J. Calibration Procedure and Accuracy of Wind and Turbulence Measurements with Five-Hole Probes on Fixed-Wing Unmanned Aircraft in the Atmospheric Boundary Layer and Wind Turbine Wakes. *Atmosphere* **2019**, *10*, 124. [[CrossRef](#)]




© 2019 by the authors. Licensee MDPI, Basel, Switzerland. This article is an open access article distributed under the terms and conditions of the Creative Commons Attribution (CC BY) license (<http://creativecommons.org/licenses/by/4.0/>).

A.3 Publication III

Article

Validating CFD predictions of flow over an escarpment using ground-based and airborne measurement devices.

Asmae El Bahlouli ^{1,†} , Daniel Leukauf ², Andreas Platis ³, Kjell zum Berge ³, Jens Bange ³ and Hermann Knaus ^{1*}

¹ Faculty of Building Services-Energy-Environment, Esslingen University of Applied Sciences, 73728 Esslingen, Germany 1; asmae.el-bahlouli@hs-esslingen.de

³ Institute of Meteorology and Climate Research, Karlsruhe Institute of Technology, 82467 Garmisch Partenkirchen, Germany; daniel.leukauf@kit.edu

² Center for Applied Geoscience, Eberhard Karls University, 72074 Tübingen, Germany; kjell.zum-berge@uni-tuebingen.de

* Correspondence: asmae.el-bahlouli@hs-esslingen.de

† Current address: Faculty of Building Services-Energy-Environment, Esslingen University of Applied Sciences, 73728 Esslingen, Germany

Version August 20, 2020 submitted to Energies

Abstract: Micrometeorological observations from a tower, an eddy-covariance (EC) station and an unmanned aircraft system (UAS) at the WINSSENT test-site are used to validate a computational fluid dynamics (CFD) model, driven by a mesoscale model. The observation site is characterised by a forested escarpment in a complex terrain. Two measurement campaigns, with a flow almost perpendicular to the escarpment, are analysed. The first day is dominated by high wind speeds, while on the second one, calm wind conditions are present. Despite some minor differences, the flow structure, analysed in terms of horizontal wind speeds and inclination angles, shows similarities for both days. A real time strategy is used for the CFD validation with the UAS measurement, where the model follows spatially and temporally the aircraft. This strategy has proved to be successful. Stability indices such as the potential temperature and the Richardson number are calculated to diagnose atmospheric boundary layer (ABL) characteristics up to the highest flight level. The calculated Richardson values indicate a dynamically unstable region behind the escarpment and near the ground for both days. At higher altitudes, the ABL is returning to a near neutral state. The same characteristics are found in the model but only for the first day. The second day, where shear instabilities are more dominant, is not well simulated. UAS proves its great value for sensing the flow over complex terrains at high altitudes and we demonstrate the usefulness of UAS for validating and improving models.

Keywords: Complex terrain; mesoscale-microscale coupling; unmanned aircraft systems (UAS); meteorological mast measurements.

1. Introduction

To achieve the objective of making the European Union climate-neutral by 2050, it will be necessary to maximize the deployment of renewable energy in the years to come [1]. The clean energy transition involves encouraging high levels of renewable energy penetrations. Harvesting power from wind power is one of the fastest-growing renewable energy methods. To meet the climate-neutral target, more wind energy capacity will be installed in the coming years. Independent of the exact number of new installations, most of them will be onshore [2].

27 A wind energy project includes site investigation, resource assessment, environmental impact
28 assessment, technical and administrative procedures with local communities and finally, construction
29 work. The site investigation and resource assessment phases need accurate and reliable models for
30 predicting the wind flow. During the last two decades, linear flow models, mainly based on the
31 Jackson-Hunt theory [3], were extensively used in the wind industry for wind resource assessment and
32 micro-siting. These models are however inaccurate for wind speed prediction in very complex terrain,
33 which led to the use of computational fluid dynamics (CFD), capable of modelling the wind flow in
34 details around specific orographic features. The spatial and temporal variability of the atmospheric
35 boundary layer (ABL) makes the prediction of the wind flow by models one of the main challenges,
36 especially in complex terrain. The commercial CFD software for wind resource assessment uses
37 logarithmic wind profile and tunes parameters from the Monin-Obukhov similarity theory [4] to
38 calculate annual energy prediction for site assessment. The logarithmic wind profiles are not site
39 specific and don't have micro meteorological information of wind at the particular site. This is a
40 major error source for the calculation in annual energy production. Hence the variability of the
41 atmosphere should be considered at the mesoscale and only mesoscale models, driven by global
42 models, can capture the dynamic processes of the atmosphere [5]. Today's mesoscale models are
43 used increasingly for wind-energy applications with efforts in improving surface winds in complex
44 terrain [6,7]. However, it has been observed that numerical noise is appearing with increasing terrain
45 complexity [8]. A remedy is to use the data from mesoscale models of a given region as a realistic
46 boundary condition for a more detailed microscale modelling. That way, the wind characteristics can
47 be determined at a high resolution in the area of interest. This approach is referred in the literature as
48 mesoscale-microscale modelling and have been successfully used in different domains. For instance,
49 the improved predictability of pollutants such as NO_x and NO₂ in urban areas by coupling a mesoscale
50 model with a CFD model has been demonstrated in recent studies [9,10]. For wind assessment studies,
51 the performance of coupled simulations is more and more recognized and has been extended even in
52 the industry as it showed improving wind power forecasting [11].

53 All methods and models should be validated, ideally with in-situ and/or remote sensing
54 measurements. The need for field campaigns to provide data for model validation in complex terrain
55 has led to the funding of several projects over the last few years. Examples are the Kassel Experiment
56 in Germany [12], the Alaiz Experiment in Spain [13], the double-ridge Perdigao in Portugal [14]
57 or the Wind Forecast Improvement Project (WFIP2) in the U.S [15], all aiming at improving the
58 understanding of physical processes and wind forecasts in complex terrain. Traditional in situ
59 platforms for atmospheric measurements are towers installed at a certain location. The vertical
60 information is provided by instruments installed at several discrete levels. They can provide continuous
61 recording of the investigated variables over long time periods. To follow the growth of wind turbine
62 sizes, the meteorological mast should ideally become taller and have the same height as the wind
63 turbines, making their installation technically complicated and more expensive. These limitations have
64 led to the use of lidar (light detection and ranging) technologies for wind measurements. However,
65 in complex environments, the spatial heterogeneity and transient features introduced by terrain can
66 lead to difficulties in interpreting the line of sight wind speed and reconstructing the wind field
67 [16]. For instance, the central goal of the International Energy Agency Wind Task 32 community is
68 developing frameworks for the deployment and use of wind lidars in complex flow. One promising
69 approach is the use of two or more lidars to reconstruct the flow field in a complex terrain. Limitations
70 of this approach are mainly the high costs and the uncertainties [17]. Other emerging techniques
71 for wind-energy applications are flying platforms. Small unmanned aircraft systems (UAS) have
72 become frequently used platforms for ABL research. They have the advantage to be versatile, even
73 in highly complex terrain and the necessary infrastructure is small compared to masts and active
74 remote sensing techniques. They can fly in the close vicinity of a wind turbine, even at very low
75 altitudes, where the main vertical and horizontal inhomogeneities are occurring. The capability of
76 UAS for turbulence characterization and providing high spatial-temporal sampling frequencies has

77 been demonstrated in research works over the last several years. The use of these systems contributed
 78 to a better characterisation and understanding in aerosol formations [18,19], storm developments [20],
 79 atmospheric research [21–23] or for wind energy purposes [24,25].

80 In the research project WINSSENT (Wind Science and Engineering Test Site in Complex Terrain),
 81 a field test-site is being built on the Swabian Alb in Southern Germany [26]. It will be the first wind
 82 energy test site of this size in complex terrain. The first phase of the WINSSENT project investigates
 83 the local wind flow at the test site using different measurement equipments and simulation models.
 84 During the second stage, two wind turbines with a nominal output of around 750 kW, will be installed
 85 next to the escarpment. The effect of the topography on the wind-turbines performances, wakes and
 86 material fatigue will be studied both experimentally and numerically [27,28]. The on-site instruments
 87 consist of permanently installed towers equipped with ultrasonic anemometers and eddy-covariance
 88 (EC) micro-meteorological stations. Additionally, the multipurpose airborne sensor carrier MASC
 89 [29] and several lidars [30] carry out measurements over and downstream of the escarpment during
 90 different measurement campaigns. All those equipments are going to provide new datasets to evaluate
 91 and validate the numerical models. In the framework of the WINSSENT project, a numerical study is
 92 conducted with models, with different range of scales such as the Weather Research and Forecasting
 93 (WRF) model [31], the Open Source Field Operation and Manipulation (OpenFOAM) software [32]
 94 and the solver FLOWer [33].

95 In the present study, a numerical and experimental investigation of the flow at the WINSSENT test
 96 site is presented. Two flight measurement campaigns, which took place over two days in September
 97 2018, are analysed. The first day is dominated with high wind speeds while the conditions on the
 98 second day are calmer. Measurements from the MASC, along with a meteorological mast and an EC
 99 station are used for the evaluation of our model. A real time strategy is adopted for the comparison
 100 of the numerical results with the MASC measurements. The performance of our methodology is
 101 presented in this study as follows: in Section 2, the numerical tools are presented while in Section 3
 102 the test site along with the measurement devices are described. Section 4 discusses the numerical and
 103 experimental results from the measurement campaigns together with a stability analysis and finally a
 104 conclusion with outlooks is given in Section 5.

105 2. Methods

106 2.1. Numerical model

107 In the current study, the wind flow is simulated using the software OpenFOAM v6. An unsteady
 108 Reynolds Averaged Navier-Stokes (URANS) approach, necessary for the investigation of non-stationary
 109 flow features, was considered [34,35]. The governing equations for mass, momentum and potential
 110 temperature, under the Boussinesq approximation, are written relative to a hydrostatic state (index h)
 111 in a Cartesian coordinate system as:

$$\frac{\partial}{\partial t}(\rho_h) + \frac{\partial}{\partial x_j}(\rho_h u_j) = 0 \quad (1)$$

$$\frac{\partial}{\partial t}(\rho_h u_i) + \frac{\partial}{\partial x_j}(\rho_h u_i u_j) = -\frac{\partial p^*}{\partial x_i} + \frac{\partial}{\partial x_j} \left[(\mu + \mu_t) \left(\frac{\partial u_i}{\partial x_j} + \frac{\partial u_j}{\partial x_i} - \frac{2}{3} k \delta_{ij} \right) \right] - \rho_h g_i \frac{\theta - \theta_h}{\theta_h} + F_{Ci} + F_{Di} \quad (2)$$

$$\frac{\partial}{\partial t}(\rho_h \theta) + \frac{\partial}{\partial x_i}(\rho_h u_i \theta) = \frac{\partial}{\partial x_i} \left[(\mu + \frac{\mu_t}{\sigma_h}) \left(\frac{\partial \theta}{\partial x_i} \right) \right] \quad (3)$$

112 here, $u_i (i = 1, 2, 3)$ are the velocity components in a Cartesian framework (x, y, z , where z is aligned
 113 with gravity), p and θ are the pressure perturbation from the hydrostatic reference state and potential
 114 temperature, μ and μ_t are the dynamic molecular and turbulent eddy viscosities, g_i is the gravitational
 115 acceleration term, and σ_h is the turbulent Prandtl number. F_{Ci} and F_{Di} are the source term representing
 116 the Coriolis and the drag force exerted by the forest on the wind flow, respectively. The hydrostatic
 117 fluid density ρ_h is defined in a hydrostatic reference state (subscript 0) as a function of the hydrostatic
 118 pressure p_h and the temperature T_h as:

$$\rho_h = \frac{p_h}{R_d T_h} \quad (4)$$

$$T_h = T_0 \sqrt{1 - \frac{2Agz}{R_d T_0^2}} \quad (5)$$

$$p_h = p_0 \exp\left(\frac{-T_0}{A} \left(1 - \sqrt{1 - \frac{2Agz}{R_d T_0^2}}\right)\right) \quad (6)$$

119 where p_0 is the constant reference pressure set to 1000 hPa, T_0 is the reference temperature equal to
 120 288.5 K, $A = 50$ K and $R_d = 287.05$ J kg⁻¹ K⁻¹ [36,37]. The Sogachev $k - \epsilon$ model is used for the
 121 turbulence closure [38]. Additionally, source terms in the turbulent kinetic energy and turbulence
 122 dissipation rate equations, using the constants proposed by [39] were added in order to take into
 123 account for the drag effect of vegetation on the flow.
 124 The PIMPLE pressure-velocity coupling algorithm is used for solving the URANS equations.
 125 Second-order interpolation schemes are used for the gradient, Laplacian and divergence terms, with a
 126 convergence criteria for residuals lower than 10⁻⁶.

127 2.2. Computational set up and mesoscale forcing

128 The simulations are conducted on a domain of $10 \times 10 \times 2.5$ km³, centered in the escarpment. The
 129 spatial resolution consists of 10 m increments in the horizontal directions and the vertical discretization
 130 has values between 1.8 m at the ground and 80 m at the top of the domain. The terrain data was
 131 based on the digital height model from the Baden-Württemberg Authorities for Spatial Information
 132 and Rural Development (LGL) with a spatial resolution of 5 m. In addition, the digitized landscape
 133 model from LGL was utilized to describe the land cover on the Earth's surface. Three classes of land
 134 uses were retained for this study: urban, ground, and forest (Figure 1b). In this paper, a deciduous
 135 forest with a height of 20 m is considered for the forest patch. The urban and the ground classes were
 136 assigned values of 0.50 m and 0.02 m for the aerodynamic roughness length.
 137 The mesoscale flow is simulated using WRF with five nested domains. WRF uses the European Centre
 138 for Medium-Range Weather Forecasts analysis data as initial and boundary conditions. The innermost
 139 nest has a horizontal grid size of 150 m, a vertical grid size of 15 m close to the ground and is run in
 140 a large eddy simulation mode. A one-way nesting method was used for the coupling of WRF and
 141 OpenFOAM: the innermost nest provides boundary conditions to the microscale model. Border data
 142 include the velocity components, pressure and temperature at 1 minute intervals. The WRF model
 143 provides also the heat flux at the ground. No special temporal and spatial interpolation has been
 144 applied as the mesoscale model is considered fine enough near the ground.

145 3. Test site and measurements

146 3.1. Test site

147 The field measurements were made at the WINSSENT test site, built on the Swabian Alb in
 148 Southern Germany. The main feature of the site is a sloping escarpment up to 200 m in height with
 149 respect to the valley (see Figure 1a). The escarpment is characterized by a very steep slope of around
 150 30° from the Northwest and a more gradual slope at around 15° further west. A dense vegetation with
 151 a tree height between 15 m and 25 m is covering the escarpment. To the west of the escarpment, the
 152 ground is essentially flat and under agricultural use. The windrose (Figure 1c) measured on a height of
 153 86 m at the test site shows winds blowing predominantly from the west, and therefore perpendicular
 154 to the escarpment, most of the year.

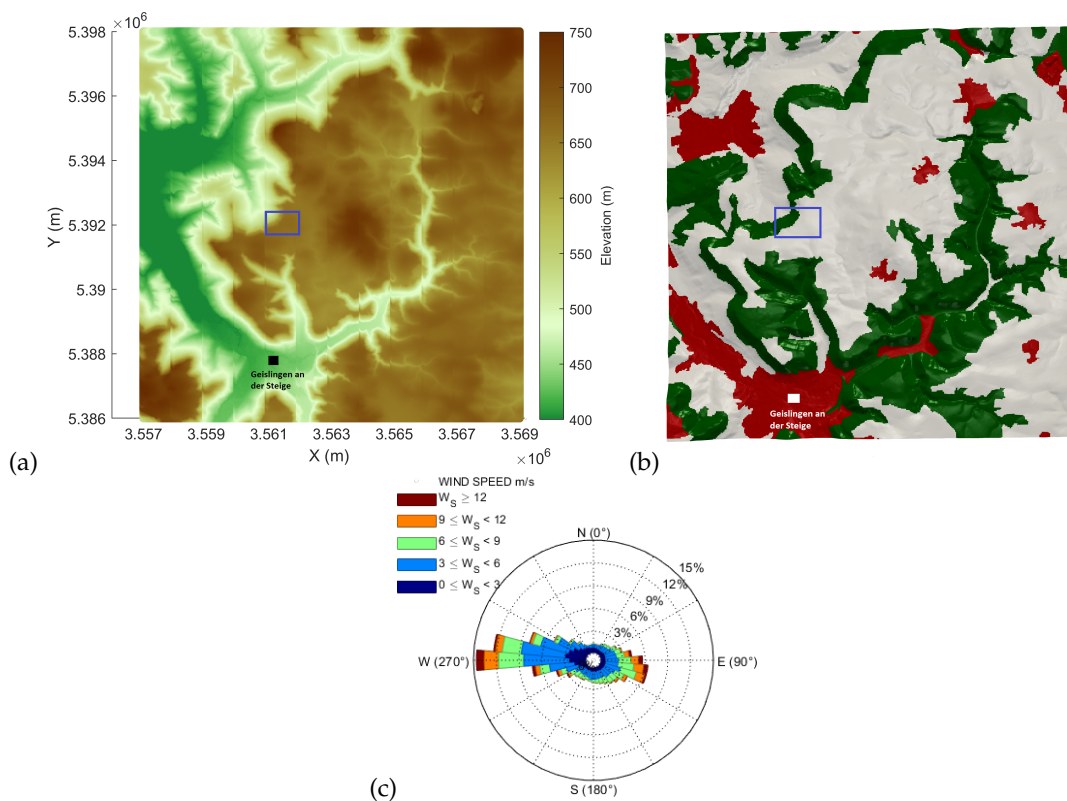


Figure 1. (a) Orography with the blue box marking the test site (Gauß-Krueger coordinates). (b) The different land uses applied in the simulations: red for urban, grey for ground and green for forest. (c) Wind rose from 86 m at the test site tower for the period of mid 2018–2019.

155 3.2. Measurements

156 Measurements took place on 21 and 22 September 2018. Cup anemometers sampling at 20 Hz
 157 are mounted on the tower (48.6652° latitude, 9.8347° longitude) along with hygrothermographs, wind
 158 vanes and barometers at various heights between 3 and 100 m (Table 1). At that time, the sonic
 159 anemometers were not yet installed and therefore only the cup anemometer results are presented
 160 in this article. To minimise flow distortion due to the tower for the main wind directions, most
 161 instruments are mounted on booms pointing in south-north direction (Figure 2a). An EC station is
 162 installed 50 m west of the tower. The raw data were recorded at 20 Hz. However, the 10-minutes
 163 statistics (as prescribed by the international standard IEC 61400-12-1) are used in this study unless
 164 otherwise noted.

165 Additionally, in situ measurements are made using the multipurpose airborne sensor carrier (MASC
 166 [24,25,29]). The MASC is an instrumented unmanned aircraft system which can resolve turbulent wind
 167 and temperature fluctuations with a resolution of 30 Hz. The wind measurements are performed by
 168 measuring the flow speed and flow angles at the aircraft nose with a five-hole flow probe. In order to
 169 measure the three-dimensional flow field at the test site, a vertical grid of racetracks with legs going
 170 back and forth over the test site was performed between 10:55 and 12:30 UTC and between 12:55
 171 and 14:17 UTC for the first and second day, respectively. This experimental configuration allows for
 172 the changes in the flow field to be mapped in the region of the escarpment. An example of straight
 173 portions of the flight path selected for the analysis is shown in Figure 2b. Each racetrack consisted of
 174 several horizontal straight flight legs, in and against the flow direction. At least three legs (straight
 175 and level flight sections of about 1 km length) for each altitude were performed. Table 1 provides a
 176 detailed overview of the instruments used.

Table 1. Overview of instruments.

Instrument, Mark	Location: height above ground level (agl.)
Cup anemometer, Thies	10, 45, 59, 72, 86, 100
Hygrothermograph, Thies	3, 23, 45, 72, 96
Barometric Pressure Transducer, Setra	3, 96
Wind Vane, Thies	34.5, 59, 86
EC station	2
MASC	20, 30, 40, 50, 60, 70, 80, 120,130, 160, 190, 200



Figure 2. (a) View of the tower taken from east-southeast. To the west the tower is a dense canopy. This picture shows that the lowest anemometer (10 m) and the EC-station are directly downslope of the forest. (b) The flight patterns performed over the two days in September 2018. The colors along the legs indicate the measured horizontal wind speed. The red triangle marks the position of the meteorological mast and the yellow one is the EC-station. The white triangles are the future location of the wind turbines.

177 4. Results and Discussion

178 In this section, the simulation results are presented and compared with the tower and flight
 179 measurements. The focus in this study is put on the period of the UAS measurement campaigns.

180 4.1. Comparison of wind and turbulences quantities with the tower and EC measurements

181 The simulation results are compared with measurements from cup anemometers and wind vanes
 182 installed on the mast. Time series of the 10- minute averaged horizontal velocity and wind direction
 183 are shown in Figure 3 and 4, respectively. The left panel of the following figures shows the results
 184 for the first day (21th September 2018), while the right one shows results for the second day (22nd
 185 September 2018). The approximate times of the flights are indicated with a grey box in these figures for
 186 reference. On the 21th September the wind speed measurements ranged from 7 m s^{-1} to 11 m s^{-1} at

187 86 m a.g.l, while calmer wind conditions dominate the second day, with velocities between 4 m s^{-1} and
 188 7 m s^{-1} . The wind speed is in general well simulated, except for the upper level on the 21th September
 189 at 11:20 and 13:20 UTC and the first half an hour for the 22nd September, where larger differences are
 190 observed. The simulated wind direction at upper levels is in accordance with the measured results.
 191 On the 22nd September, the wind direction near the ground shows high deviations. Indeed, values for
 192 wind direction at the EC-station show high variability even in the model, indicating a region of high
 193 turbulence and intermittent structures. The main flow is coming from west as shown by the relative
 194 constant value of 270° at 86 m a.g.l, whereas near the ground, the flow is more southerly orientated.
 195 This is clearly visible for the second day, with values reaching 200° at 14:10 UTC.
 196 It can be seen in Figure 3 and 4 that during the period of the flight campaign (marked with a grey box),
 197 the wind direction is remaining nearly constant between 240° and 275° for the first day and 265° and
 198 285° for the second one. Only the wind speed shows a drop from 11 m s^{-1} to 7 m s^{-1} during the last 30
 199 minutes for the first date. Except for the wind speed at 11:20 and 13:20 UTC on the 21th September, the
 200 plots indicate a wind speed well simulated during the flight campaigns with values for mean absolute
 201 error at 100 m a.g.l of 2.00 m s^{-1} and 0.74 m s^{-1} for the first and second day, respectively.

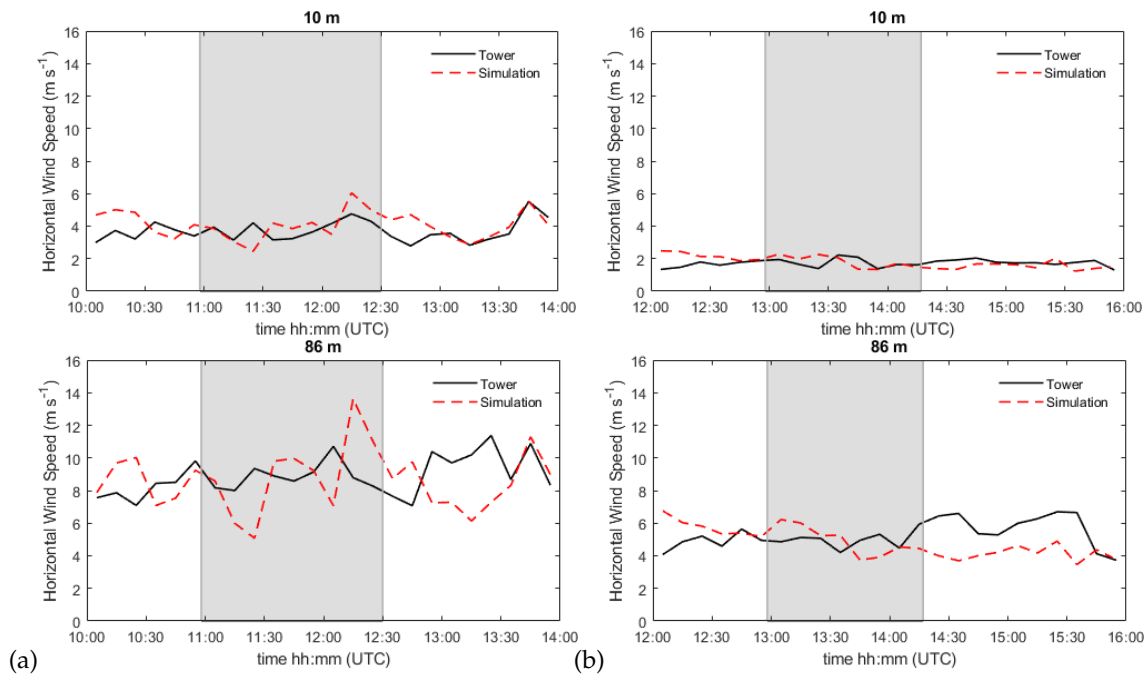


Figure 3. Time series of 10-minute averages of horizontal wind speed at 10 m and 86 m on the 21th (a) and 22nd (b) September. Shown are the time series for the simulation (red) and the tower observations (black). The grey box marks the time flight period.

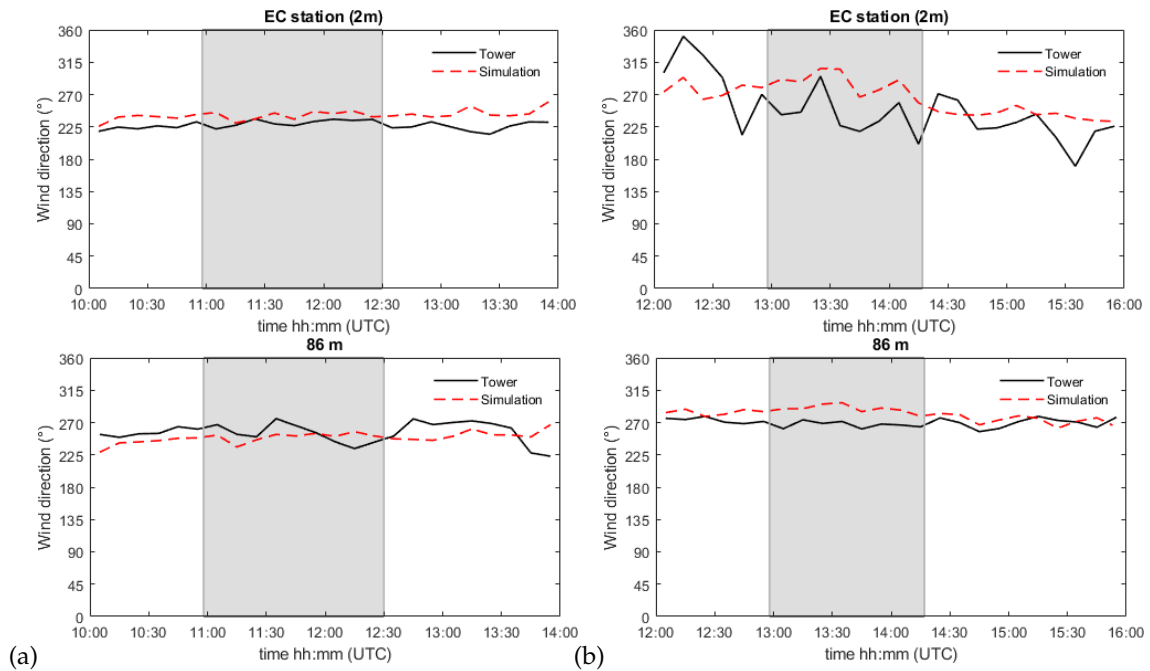


Figure 4. Time series of 10-minute averages of wind direction at 2 m and 86 m a.g.l. on the 21th (a) and 22nd (b) September. See also Figure 3.

202 Turbulence is evaluated in terms of horizontal turbulence intensity (TI) given by the standard
 203 deviation of the horizontal wind speed normalized with the mean wind speed. Figure 5 compares the
 204 10-min average simulated turbulence intensity against the measured data at 10 m and 86 m a.g.l. The
 205 higher turbulence intensities are observed at the lower heights, i.e. at 10 m, with values above 40 %. For
 206 the 22nd September, the TI values are even higher and can be explained by the definition of TI, which
 207 becomes large for small wind speeds. Several experimental [40,41] and numerical [42] studies have
 208 revealed that the maximum turbulent energy is produced in the upper half of the forest and carried
 209 into the region behind the forest [43,44]. For a westerly flow as in the present work, the 10 m sensor is
 210 located about 60 m downstream of the forested escarpment and explain the high turbulence intensity
 211 values in comparison to the higher sensor at 86 m. The model simulates reasonably well TI at the upper
 212 level and fails at catching the high TI values in the lower heights. The vegetative sink introduced by
 213 the canopy model in the turbulence equations may be responsible and leads to an underestimate of the
 214 turbulent fluctuations.

215 Figures 6 shows 10-min averaged wind speed profiles at the tower position. The blue circles are data
 216 from the cup anemometers and the dashed lines the simulated wind speed. Error bars, corresponding
 217 to one standard deviation, are inserted for the anemometers measurements. Above 10 m, the standard
 218 deviations (errorbars) are decreasing with height and reveal a greater variability at 45 m a.g.l. except
 219 for some specific times. The wind speed increases progressively with increasing height, with a visible
 220 wind speed reduction in the lower part of the profiles, i.e. at 10 m. On the first day, the wind speed at
 221 the lower cup anemometer are between 36 and 56 % of the one at 100 m. The wind speed reduction is
 222 higher on the second day with ratio values ranging between 28 and 35%. Overall, the simulated and
 223 observed wind speed agree well in profile shape, except for some specific times, but the wind speed
 224 reduction is underestimated in comparison to measurements.

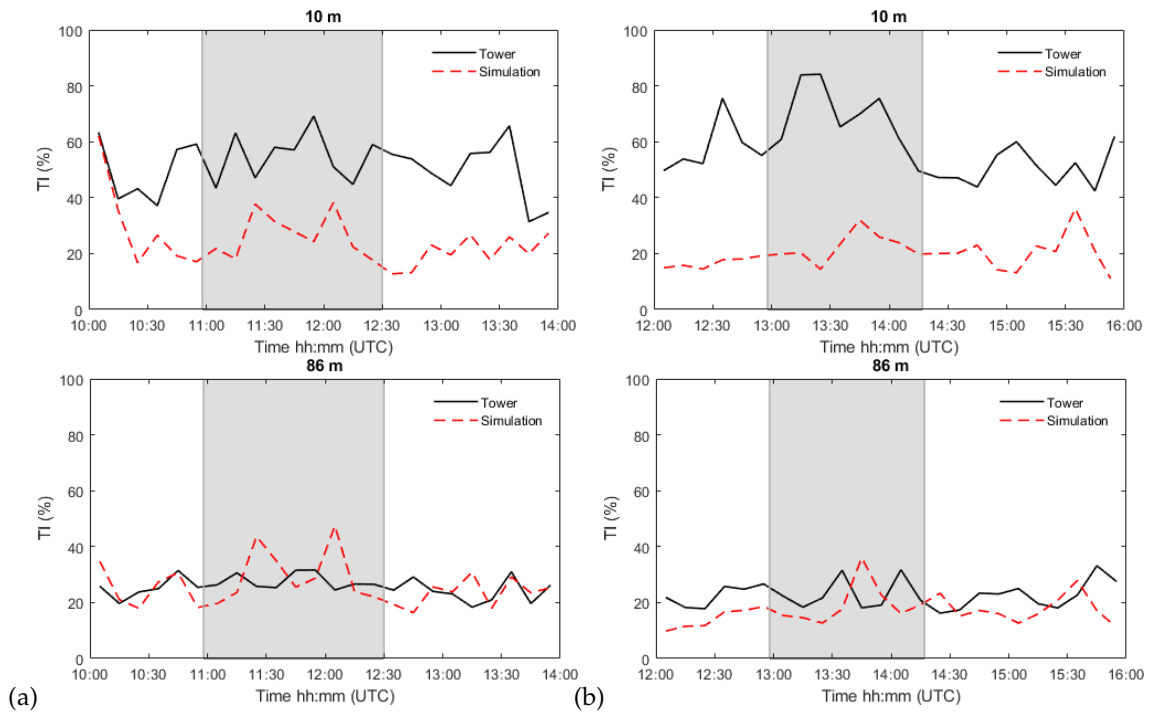


Figure 5. Time series of 10-minute averages of turbulence intensity at 10 m and 86 m on the 21th (a) and 22nd (b) September. See also Figure 3.

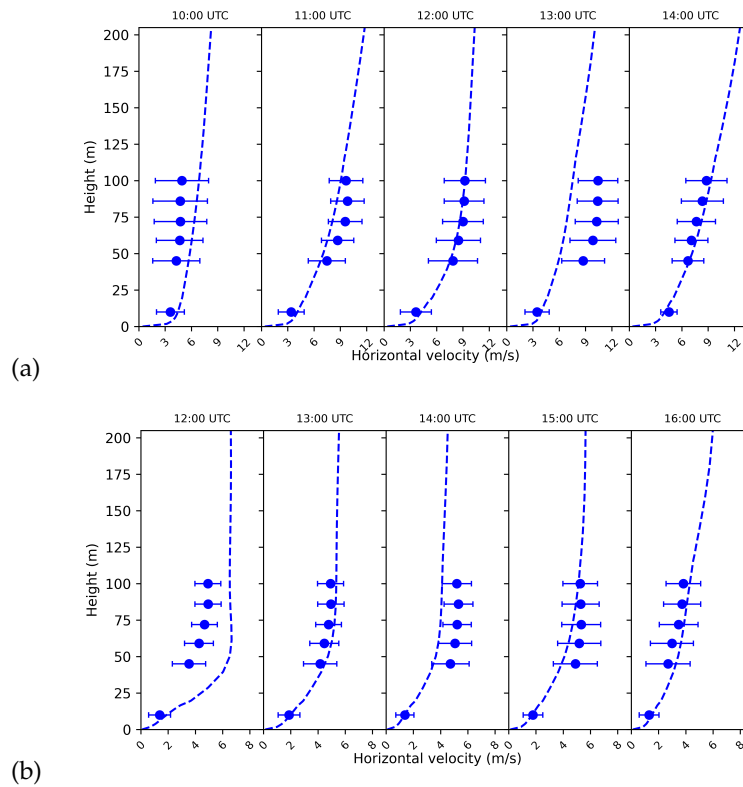


Figure 6. 10-min horizontal wind speed profiles for each hour at the tower on the 21th (a) and 22nd (b) September. Cup anemometer data are indicated with a blue circle and the simulation with the blue dashed lines.

225 4.2. Comparison with the UAS measurements

226 The flight path consists of horizontal measurements legs made over and downstream of the
 227 escarpment, beginning at 20 m up to 200 m a.g.l as shown in Figure 2. About 95 and 82 minutes were
 228 necessary to perform the complete flight path on the 21th and 22nd of September 2018, respectively.
 229 Probes were placed in the CFD model at the leg positions and data are extracted for every simulation
 230 time steps. For a direct comparison of the simulation results and the UAS measurements, the probes
 231 were selected in order to fit the flight time. The airborne wind measurements are then averaged over
 232 subsections of 20 m in length along each leg. Figure 7 illustrates the steepness of the terrain with a
 233 slope of around 20°. It also shows the position of the modelled forest in green and in blue the legs
 234 flown on both days. Except for the three upper altitudes, the pattern are almost similar between the
 235 two flight dates as shown in Figure 7a and b.

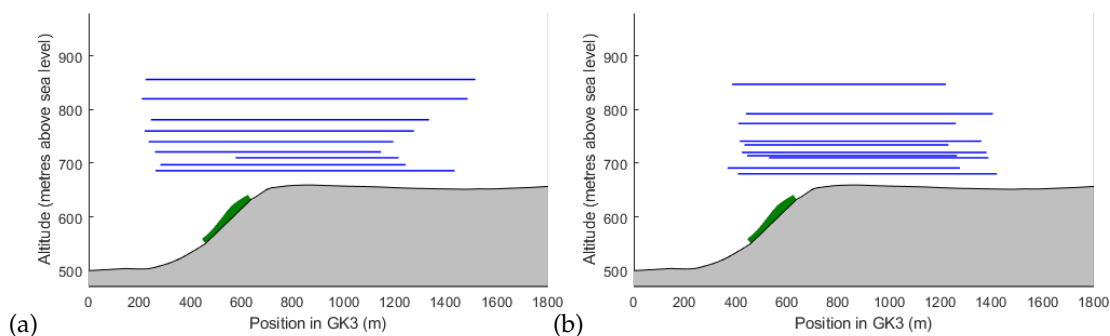


Figure 7. Visualisation of the modelled ground. The blue lines correspond to the legs performed by the MASC on the 21th (a) and 22nd (b) September. The green block represents the modelled forest.

236 4.2.1. Wind speed, wind direction and inclination angles

237 Figure 8 shows the horizontal wind speed at five different flight legs. For the 21th of September,
 238 levels at 20, 50, 80, 120 and 200 m a.g.l were selected, while 20, 50, 70, 130 and 190 m a.g.l were
 239 chosen for the second day. Error bars, corresponding to the standard deviation, are inserted for the
 240 UAS measurements. The standard deviations are binned over a window length of 20 m as well. The
 241 geometry of the ground and the position of the forested patch are added for better visualization. The
 242 scale for the velocity was deliberately changed for both days in order to give a better visualisation of
 243 the flow along the UAS paths. The measured velocities show a similar structure for both days: directly
 244 after the slope, the velocities are higher due to a local updraft generated by the orography. Generally,
 245 the simulated wind speed match very well the UAS measurements, with a slight overprediction at
 246 upper levels for the first day, as already observed in the time series in Figure 3.

247 The measured and simulated wind direction are presented in Figure 9. The profiles at higher altitudes
 248 are relatively flat. The wind direction values are increasing with decreasing height. For the 21st
 249 September, the wind veer shows a difference up to 60° between 20 and 200 m. On the second day, the
 250 wind veer is smaller but still visible with values reaching 30°. The model performs well at upper levels,
 251 except for the first day where the wind direction changes with height is underestimated. Considering
 252 the wind direction changes is important for the wind industry, as the occurrence of large wind veer
 253 can result in lower turbine performance [45].

254 Inclination angles are important for each turbine site: wind turbines have to be certified by the
 255 standards such as IEC 61400-1, where inflow angles are usually required to be within $\pm 8^\circ$ [46]. The
 256 future turbine locations should comply with this requirement to ensure that the turbines will withstand
 257 the wear and tear during their expected life time. The modelled and measured inflow angles compared
 258 to each other are presented in Figure 10. Sudden changes in the inclination angle are numerically
 259 and experimentally noticed over the escarpment and are due to a local phenomenon induced by local
 260 features of the terrain. Positive flow angles of up to 15°, numerically, and 20°, experimentally, are

261 reached. The position of this maximum reveals a flow dominated by upward movements and is
262 located over or straight after the escarpment. The flow remains disrupted even at upper levels (190 m
263 and 200 m a.g.l), where inclination angle becomes smaller but still differs from zero. It is noticeable
264 that for the second day, a negative angle can experimentally and numerically be seen in the last thirds
265 of the flight path, indicating a flow not yet recovered.

266 As a surprise, the inclination angle is negative (i.e. a vertical wind component from above) at the
267 beginning of the escarpment, even in the model, revealing an incoming flow that is already disturbed.
268 For a westerly wind, the air passes over a small hill, located around 1.5 km west to the test site (Figure
269 1a) and a recirculation can be expected in the valley, leading to negative inclinations at the end of
270 the valley and still at the beginning of the escarpment. The inclination angles then return to positive
271 values at the upper edge of the escarpment as could be expected by an orographically influenced flow
272 that follows the terrain. To check this hypothesis, the simulated vertical wind speeds in a cross-section
273 along the legs for both days are shown in Figure 11. The simulated values are averaged over the
274 complete flight campaign, i.e 95 and 82 minutes. On the 21th September, a large recirculation zone
275 enclosed between the hill and the escarpment can be seen and corroborates our hypothesis.

276 The variability of the horizontal wind speed and inclination angle, indicated by the standard deviations,
277 represent a measure of the turbulence intensity. Their values are larger at low altitudes in comparison
278 to higher levels due to increased turbulence near the ground. Looking at the two lowest levels, it is
279 even noticeable that the variability is greater right after the escarpment. This is in accordance with
280 the observation from the meteorological mast in Figure 5. Despite the large differences in the wind
281 condition (high and low wind speeds) for both days, the flow structure seems to be quite similar.

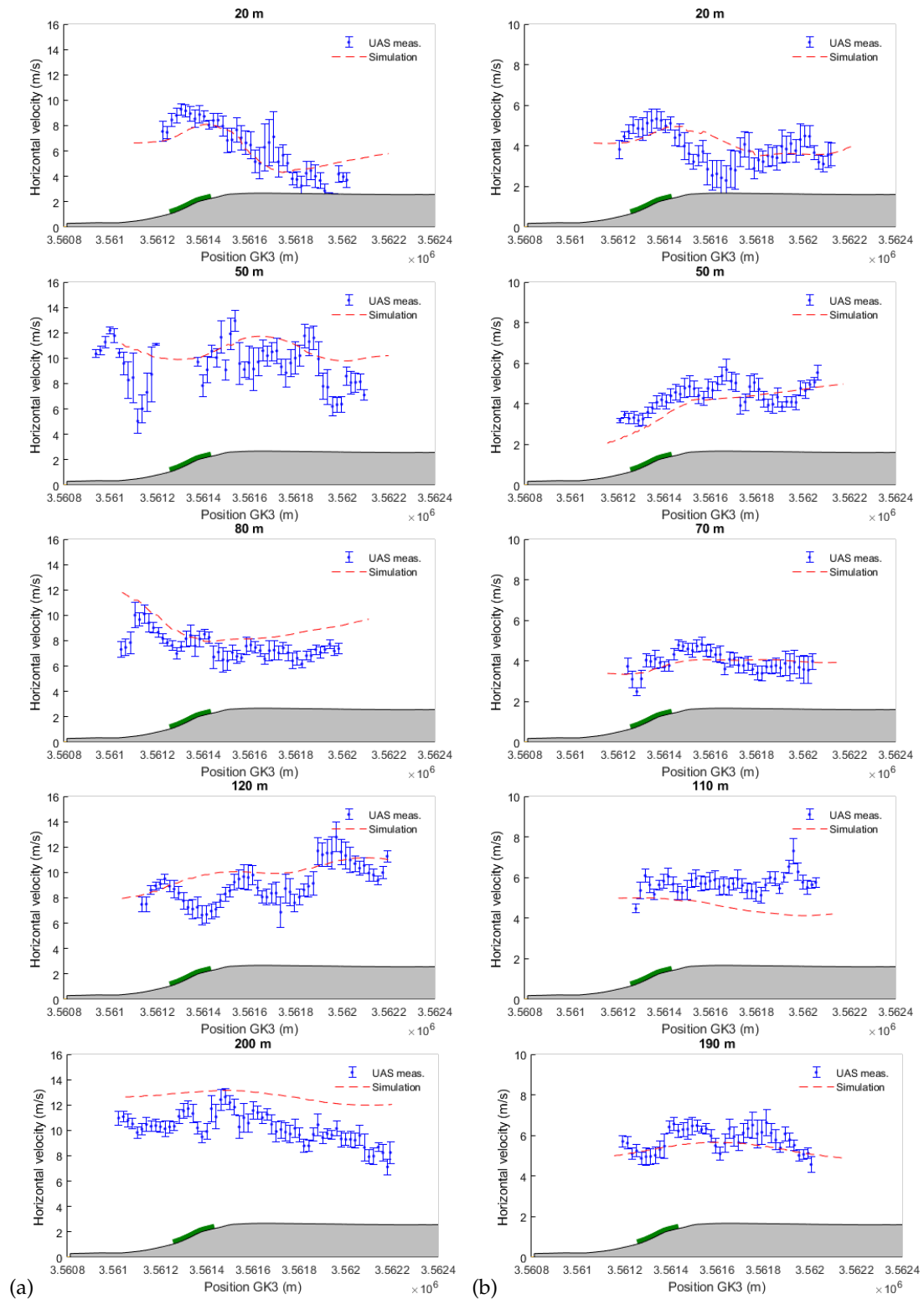


Figure 8. Horizontal velocity on the 21th (a) and 22nd (b) September at different altitudes along the UAS' flight path. The blue dots are the UAS measurements and the red one the simulation results. Error bars, corresponding to one standard deviation, are inserted for the MASC measurements. The green block represents the modelled forest.

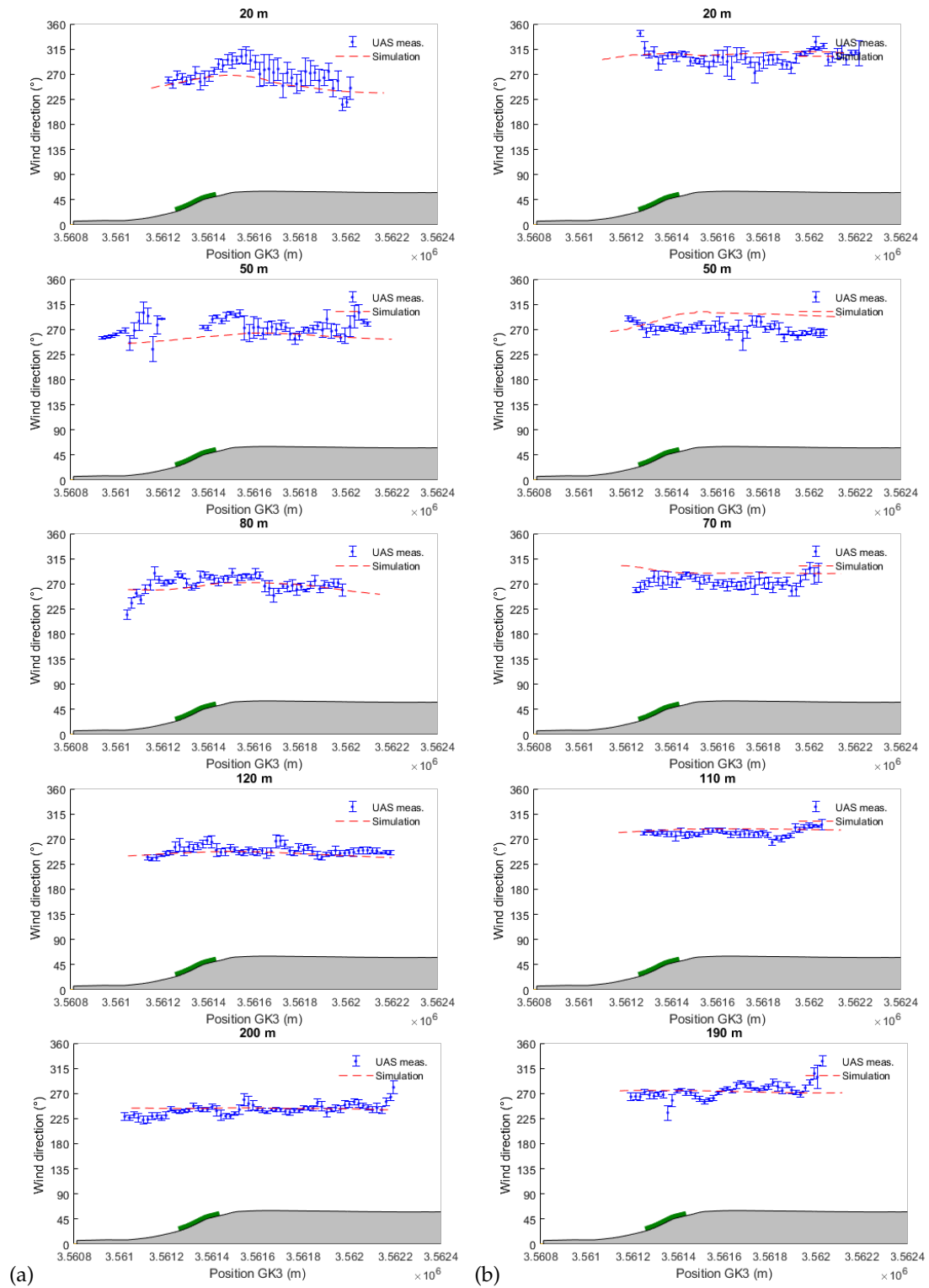


Figure 9. Wind direction on the 21th (a) and 22nd (b) September at different altitudes along the UAS' flight path. See also Figure 8.

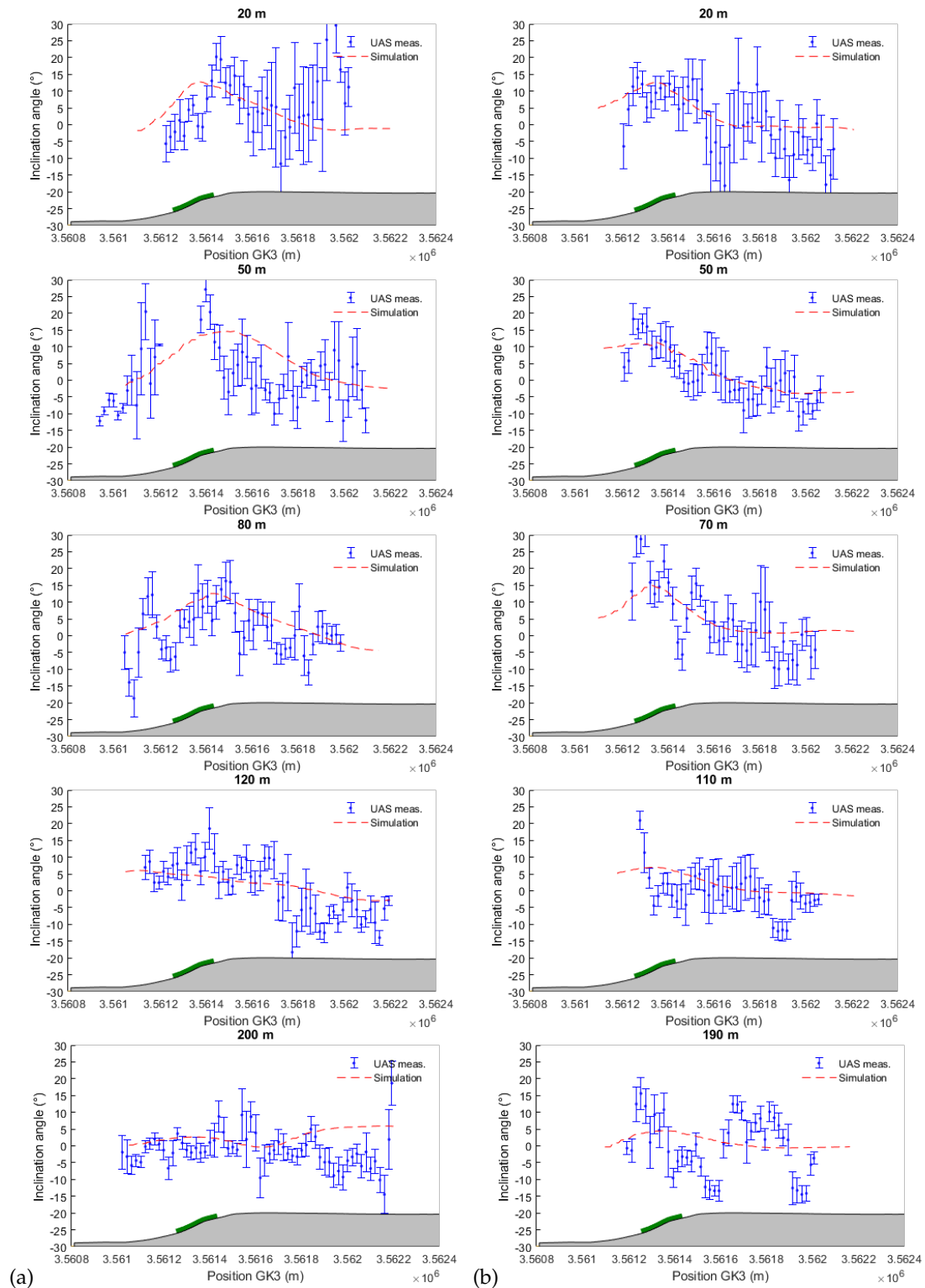


Figure 10. Inclination angles on the 21th (a) and 22nd (b) September at different altitudes along the UAS' flight path. See also Figure 8.

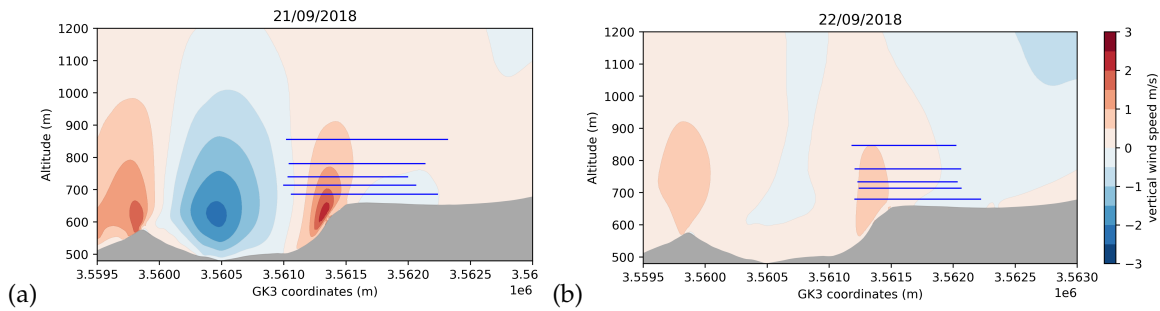


Figure 11. Cross-section of vertical wind speed averaged over the complete flight campaign on the 21th (a) and 22nd (b) September. The blue lines correspond to the legs plotted in Figure 8 and 10 performed by the MASC.

4.2.2. Stability considerations

The stability can be characterized, e.g. using the potential temperature or the Richardson number. The assessment of atmospheric stability using ground stations and towers is difficult in complex terrain as the flow can be characterized by phenomenon such as updraft, downdraft or canopy flow. A UAS can sample the atmosphere at higher altitudes in comparison to ground-based instrumentation, and can be a tool for atmospheric stability measurement. In our study, the potential temperature and the bulk Richardson number are used to assess the stability behaviour at the test site. The bulk Richardson number Ri_B [47], which can be computed from the wind and temperature measurement at two heights, is defined as:

$$Ri_B = \frac{g}{T_a} \frac{(\theta_u - \theta_l)(z_u - z_l)}{(U_u - U_l)^2} \quad (7)$$

where T_a is the average air temperature of the layer, θ_u and θ_l are the potential temperature at the upper z_u and lower level z_l , respectively. U is the horizontal wind speed and $g = 9.81 \text{ m s}^{-2}$ is the gravitational acceleration. There is still debate about critical Richardson Ri_c values, but typically $Ri_c = 0.25$.

The diurnal pattern of potential temperature over the entire two days by the met mast is presented in Figure 12. It can be observed that at the flight time periods (indicated by a grey box) for the first day, the mast recorded vertical potential temperature gradients near zero, corresponding to near neutral atmospheric conditions. On the second day, a slightly unstable atmosphere can be observed. The sudden drop in the temperature at 15:00 on the 21th September due to a cold front has led to lower temperatures (around 10 K lower) on the 22nd September. In Figure 13, the bulk Richardson number at the mast is calculated using the mean wind speed and temperature data (10-min means), between 45 m and 100 m a.g.l. During the periods of interest (grey box), the near neutral state on the 21th September ($Ri_B \approx 0$) and the unstable state on the 22nd September ($Ri_B \approx -0.8$) is clearly visible. Unstable conditions increase the turbulence intensity and explain the higher TI values observed on the second day (Figure 5).

The potential temperature profiles from the meteorological mast, the MASC and the simulation are compared in Figure 14. The MASC measurements are separated in three regions: one over the escarpment, the second part is centered around the meteorological mast and the last region is further downstream. The simulation results are averaged over the complete flight campaign periods. The potential temperature at all positions decreases with height in the lower 50 m and 100 m for the first and second day, respectively. Above the escarpment, the simulation shows a potential temperature approaching neutral stratification at heights above 40 m a.g.l. The flight pattern is not following the terrain and therefore the lowest measurement at this position is at 50 m a.g.l. In the future, a flight strategy following the terrain should be implemented. In the middle region, the meteorological mast

316 values (green dots) show a superadiabatic layer next to the ground, with a stronger temperature
 317 decrease with altitude on the second day. On that day, gradient values of 1.5 K at the lowest 100
 318 m are reached. The MASC is measuring a gradient of 0.5 K between 20 and 50 m a.g.l. A stronger
 319 temperature gradient could have been measured if the MASC flew at very low altitudes (under 20 m
 320 a.g.l.). The agreement between the different systems (MASC and meteorological tower) is however
 321 good, given the systematic differences in the measurement techniques, as well as in the vertical and
 322 temporal resolutions. The simulation underestimates the strong gradient near the ground. This may
 323 be the result of a low vertical resolution near the ground but also the surface heat fluxes from the
 324 mesoscale model, which are underestimated around mid-day, i.e during the measurement campaigns.

325
 326 The bulk Richardson number based on a 20 m averaging windows is computed over the legs to
 327 assess the impact of the escarpment, with its forest, in enhancing critical conditions for shear instability.
 328 For the computations, three levels were chosen: a low level near the ground, a medium one and the
 329 highest flown altitudes. Figure 15 shows the distribution of Richardson's number over the test site.
 330 The drop in the bulk Richardson numbers right after the escarpment next to the ground (see Ri_B values
 331 between 20 and 120 m and between 20 and 110 m) for both day provide evidence for the criticality of
 332 the flow to shear instability and thus the generation of the turbulence. Thermodynamic instability near
 333 the ground associated with a turbulent wind flow leads to negative Ri_B values. The bulk Richardson
 334 values are then stabilizing around 300 m behind the escarpment. On the 21th September, it can be
 335 noticed that the bulk Richardson values computed at the upper levels (between 120 and 200 m) are
 336 equal to zero as the mechanical turbulence increases. The boundary layer approaches neutral stability,
 337 where potential temperature gradients are almost equal to zero, while for the second day, the surface
 338 layer is clearly in an unstable state with weak winds near the ground. This effect doesn't dissipate
 339 with height, with Richardson values keeping negative at higher levels. The computed bulk Richardson
 340 values from the MASC are in accordance with the simulated values for the first day. From 15b one
 341 may see that the values over the escarpment are positive, which is due to a negative wind shear and
 342 resulting in a positive bulk Richardson values. The simulation shows on this day an atmosphere been
 343 dynamically stable where it is, in fact still unstable.

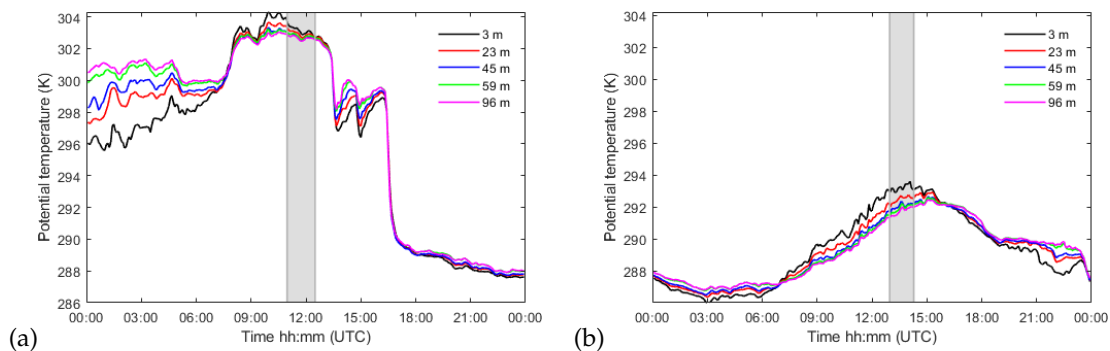


Figure 12. Time series of 10-minute averages of potential temperature on the 21th (a) and on the 22nd (b) September. The dashed, grey box marks the time flight periods.

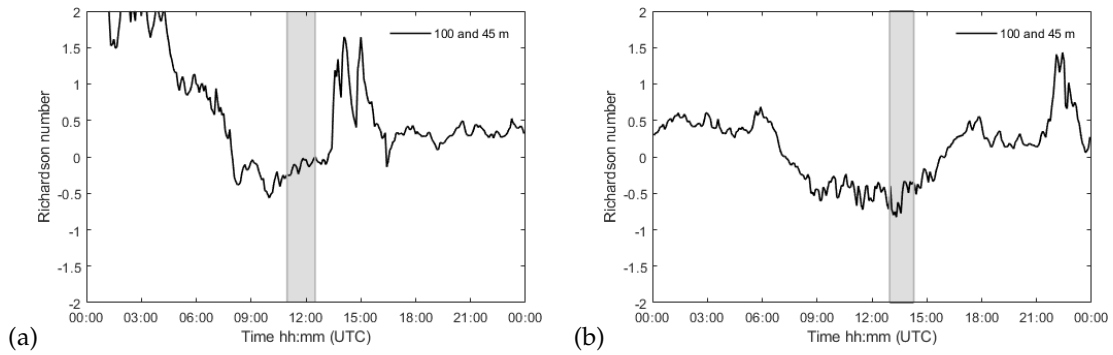


Figure 13. Time series of 10-minute averages of the Richardson number on September 21 (a) and 22 (b). The dashed, grey box marks the time flight periods.

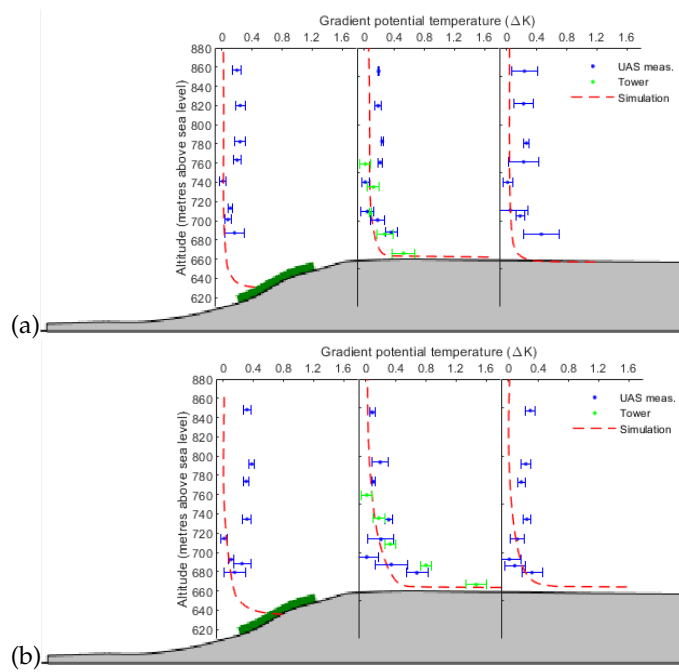


Figure 14. Vertical profiles of potential temperature differences from the MASC, the meteorological mast and the simulation over, behind and further downstream the escarpment on the 21th (a) and 22nd (b) September.

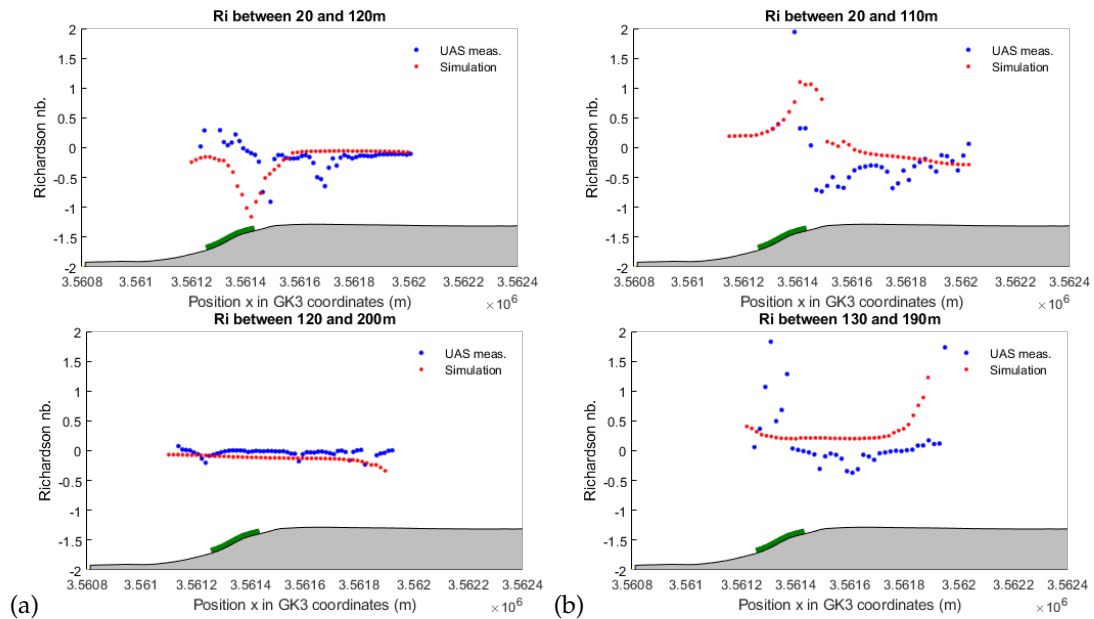


Figure 15. Richardson number computed from the UAS measurements on September 21 (a) and 22 (b) at different altitudes along the UAS' flight path using 20 m horizontal intervals. The green block represents the modelled forest.

344 To summarize the results, it was found :

- 345 • Both days have a similar flow structure with a wind direction perpendicular to the escarpment.
346 The only differences are the wind speed levels: strong and calm wind condition for the first
347 and second day, respectively. The simulated wind speed and wind direction are in accordance
348 with the tower measurements, except for some specific times on the first day. During the flight
349 campaigns, values for mean absolute error of 2.00 m s^{-1} and 0.74 m s^{-1} are found for the first
350 and second day, respectively. The meteorological mast, positioned 60 m behind the forest, clearly
351 shows the impact of the forest with a wind speed in the lower levels (10 m a.g.l) reduced by 50%.
352 The wind speed profiles for the first day are nearly logarithmic, while the second day shows a
353 more typical wind profiles for unstable conditions.
- 354 • The turbulence is evaluated in terms of horizontal turbulence intensity. The model simulates
355 reasonably well at the upper levels but large discrepancies are observed in lower altitudes
356 compared to the tower measurements. This may be directly linked to the canopy model. Possible
357 future improvements require a deeper investigation on the plant canopy and the turbulence
358 model.
- 359 • The UAS measurements are used for the model validation. In order to avoid any temporal
360 averaging, a real time strategy is applied, where the model follows spatially and temporally the
361 aircraft. An accelerated flow is numerically and experimentally found over the escarpment. The
362 model slightly over-predicts the wind speeds at higher levels for the first day but still match very
363 well the UAS measurements. The flow structure remains the same, despite a range of different
364 velocities.
- 365 • A wind veer has been observed experimentally and numerically observed. The wind direction
366 changes are higher for the 21st September.
- 367 • Inflow angles can be measured on site with sonic anemometers, but these on-site measurements
368 are limited to the mast locations on which the anemometers are installed, and significant difference
369 may exist between the inflow angle at the mast location(s) and the inflow angle at the turbine
370 locations. The MASC overcomes this problem. Upward movements over and straight after
371 the escarpment are observed. The inclination angles at an altitude of about 200 m are smaller
372 but still not equal to 0° , indicating a flow still influenced by the orography and topography.

373 Inclination angles of 5° and 2° , at the future turbine location, are found for the first and second day,
374 respectively. The test-site has been intentionally placed at a location that offers high inclination
375 angles.

376 • The stability of the atmosphere can be described based on tower measurements but the UAS
377 offers the opportunity to sample at higher elevations. The calculated and simulated potential
378 temperature profiles are in accordance, with a near neutral ABL on the first day. The second day,
379 dominated by a more convective surface layer at the test-site is not well simulated. Indeed, the
380 superadiabatic layer next to the ground is numerically underestimated. The temperature values
381 at the ground in the OpenFOAM model are obtained by reading the surface heat fluxes from the
382 WRF model and the low resolution (150 m) may be the reason of this underestimation. In future
383 works, it will be interesting to nudge the CFD model with the EC measurements for the ground
384 temperatures. The Richardson values show a systematic drop behind the escarpment for layers
385 near the ground and reveals thermodynamic instabilities.

386 5. Conclusions

387 In the present study the flow over the WINSENT test-site was numerically and experimentally
388 investigated for two days. Standard measuring systems such as a meteorological mast or an EC station,
389 but also an unmanned aircraft system are used for the numerical validation. The CFD model, driven
390 by the WRF data, relies on an unsteady RANS model with a canopy model for the forested areas. A
391 simple one-way coupling approach shows good agreement with tower and EC measurements for the
392 wind speed and wind direction. However no acceptable accuracy for the turbulent intensity could
393 be reached at the lower levels, where high wind shears are occurring, and therefore, need to be more
394 investigated.

395 The dataset provided by the flight measurement campaign demonstrates how an UAS system can
396 be helpful for the ABL investigation by providing a high spatial resolution of the airflow near the
397 escarpment. Numerical validation is performed by following the position of the MASC during the
398 flight campaign, which takes more than an hour. In this way, the variation of the flow is caught and no
399 time averaging is needed. A comparison of the horizontal wind speed, wind direction and inclination
400 angle was able to determine the accuracy of our method. Generally, the simulated wind speed, direction
401 and inclination angle match well with the MASC measurements. The stability characterization shows
402 that the model is predicting well for the first day but need improvement for the second day, dominated
403 by more unstable conditions. The UAS is still an exotic tool for wind resource assessment. This study
404 provides confidence in using UASs as a meteorological diagnostic tool or use it for data assimilation in
405 models. A recently published study shows preliminary results from a WRF model, using assimilation
406 of UAS data collected during the LAPSE-RATE Experiment [48]. The applied method shows improved
407 prediction of wind speed and direction and is encouraging for future UAS data assimilation research.
408 A good level of accuracy is achievable by considering a CFD model, driven by a WRF model, at
409 relatively low computational costs compared to LES or DES. The method presented in this paper will
410 be extended by coupling the OpenFOAM model to a DDES solver [33], where the future wind turbines
411 will explicitly be included. In future, intensive observation periods with additional equipment, such as
412 Lidars, and under stronger thermal stratifications will be performed.

413 **Author Contributions:** A. E performed the simulations and analysed the measurement data. D. L. conducted the
414 mesoscale simulations necessary for the boundary conditions. H. K. contributed to the design of the model. A.P.,
415 K. B. and J. B. designed and conducted the flight experiments. All authors read, reviewed and provided input for
416 the manuscript.

417 **Funding:** This publication was made possible through the collaboration in the WindForS wind energy research
418 cluster. The authors acknowledge the German Federal Ministry for Economic Affairs and Energy for funding
419 the WINSENT project (No 0324129) and the Baden-Württemberg Ministry of Science, Research and Culture for
420 funding the programme Open Access Publishing.

421 **Acknowledgments:** The authors acknowledge the State of Baden-Württemberg through bwHPC for providing
422 computational resources.

423 **Conflicts of Interest:** The authors declare no conflict of interest.

424 References

- 425 1. Council of the European Union. Proposal for a REGULATION OF THE EUROPEAN PARLIAMENT AND
426 OF THE COUNCIL establishing the framework for achieving climate neutrality and amending Regulation
427 (EU) 2018/1999 (European Climate Law), 2020.
- 428 2. Fraile, D.; Komusanay, I. Wind Energy in Europe: Outlook to 2023. Technical report, WIND Europe, 2019.
- 429 3. Jackson, P.S.; Hunt, J.C.R. Turbulent wind flow over a low hill. *Quarterly Journal of the Royal Meteorological*
430 *Society* **1975**, *101*, 929–955. doi:10.1002/qj.49710143015.
- 431 4. Foken, T. 50 Years of the Monin–Obukhov Similarity Theory. *Boundary-Layer Meteorology* **2006**, *119*, 431–447.
432 doi:10.1007/s10546-006-9048-6.
- 433 5. Haupt, S.E.; Kosovic, B.; Shaw, W.; Berg, L.K.; Churchfield, M.; Cline, J.; Draxl, C.; Ennis, B.; Koo, E.;
434 Kotamarthi, R.; Mazzaro, L.; Mirocha, J.; Moriarty, P.; Muñoz-Esparza, D.; Quon, E.; Rai, R.K.; Robinson,
435 M.; Sever, G. On Bridging A Modeling Scale Gap: Mesoscale to Microscale Coupling for Wind Energy.
436 *Bulletin of the American Meteorological Society* **2019**, *100*, 2533–2550. doi:10.1175/BAMS-D-18-0033.1.
- 437 6. Dudhia, J. A history of mesoscale model development. *Asia-Pacific Journal of Atmospheric Sciences* **2014**,
438 *50*, 121–131. doi:10.1007/s13143-014-0031-8.
- 439 7. Jiménez, P.A.; Dudhia, J. Improving the Representation of Resolved and Unresolved Topographic Effects
440 on Surface Wind in the WRF Model. *Journal of Applied Meteorology and Climatology* **2011**, *51*, 300–316.
441 doi:10.1175/JAMC-D-11-084.1.
- 442 8. Flores-Maradiaga, A.; Benoit, R.; Masson, C. Enhanced modelling of the stratified atmospheric boundary
443 layer over steep terrain for wind resource assessment. *Journal of Physics: Conference Series* **2019**, *1222*, 012005.
444 doi:10.1088/1742-6596/1222/1/012005.
- 445 9. Tewari, M.; Kusaka, H.; Chen, F.; Coirier, W.J.; Kim, S.; Wyszogrodzki, A.A.; Warner, T.T. Impact of coupling
446 a microscale computational fluid dynamics model with a mesoscale model on urban scale contaminant
447 transport and dispersion. *Atmospheric Research* **2010**, *96*, 656–664. doi:10.1016/j.atmosres.2010.01.006.
- 448 10. Kwak, K.H.; Baik, J.J.; Ryu, Y.H.; Lee, S.H. Urban air quality simulation in a high-rise building area
449 using a CFD model coupled with mesoscale meteorological and chemistry-transport models. *Atmospheric*
450 *Environment* **2015**, *100*, 167–177. doi:10.1016/j.atmosenv.2014.10.059.
- 451 11. Duraisamy, V.J.; Dupont, E.; Carissimo, B. Downscaling wind energy resource from mesoscale to microscale
452 model and data assimilating field measurements. *Journal of Physics: Conference Series* **2014**, *555*, 012031.
453 doi:10.1088/1742-6596/555/1/012031.
- 454 12. Klaas, T.; Pauscher, L.; Callies, D. LiDAR-mast deviations in complex terrain and their simulation using
455 CFD. *Meteorologische Zeitschrift* **2015**, *24*, 591–603. doi:10.1127/metz/2015/0637.
- 456 13. Santos, P.; Mann, J.; Vasiljevic, N.; Courtney, M.; Sanz Rodrigo, J.; Cantero, E.; Borbón, F.;
457 Martínez-Villagrasa, D.; Martí, B.; Cuxart, J. The Alaiz Experiment (ALEX17): wind field and turbulent
458 fluxes in a large-scale and complex topography with synoptic forcing **2019**. Publisher: Technical University
459 of Denmark, doi:10.11583/DTU.c.4508597.v1.
- 460 14. Fernando, H.J.S.; Mann, J.; Palma, J.M.L.M.; Lundquist, J.K.; Barthelmie, R.J.; Belo-Pereira, M.; Brown,
461 W.O.J.; Chow, F.K.; Gerz, T.; Hocut, C.M.; Klein, P.M.; Leo, L.S.; Matos, J.C.; Oncley, S.P.; Pryor, S.C.;
462 Bariteau, L.; Bell, T.M.; Bordini, N.; Carney, M.B.; Courtney, M.S.; Creegan, E.D.; Dimitrova, R.; Gomes, S.;
463 Hagen, M.; Hyde, J.O.; Kigle, S.; Krishnamurthy, R.; Lopes, J.C.; Mazzaro, L.; Neher, J.M.T.; Menke, R.;
464 Murphy, P.; Oswald, L.; Otarola-Bustos, S.; Pattantyus, A.K.; Rodrigues, C.V.; Schady, A.; Sirin, N.; Spuler,
465 S.; Svensson, E.; Tomaszewski, J.; Turner, D.D.; van Veen, L.; Vasiljević, N.; Vassallo, D.; Voss, S.; Wildmann,
466 N.; Wang, Y. The Perdigão: Peering into Microscale Details of Mountain Winds. *Bulletin of the American*
467 *Meteorological Society* **2019**, *100*, 799–819. doi:10.1175/BAMS-D-17-0227.1.
- 468 15. Shaw, W.J.; Berg, L.K.; Cline, J.; Draxl, C.; Djalalova, I.; Gritmit, E.P.; Lundquist, J.K.; Marquis, M.;
469 McCaa, J.; Olson, J.B.; Sivaraman, C.; Sharp, J.; Wilczak, J.M. The Second Wind Forecast Improvement
470 Project (WFIP2): General Overview. *Bulletin of the American Meteorological Society* **2019**, *100*, 1687–1699.
471 doi:10.1175/BAMS-D-18-0036.1.

- 472 16. Clifton, A.; Clive, P.; Gottschall, J.; Schlipf, D.; Simley, E.; Simmons, L.; Stein, D.; Trabucchi, D.; Vasiljevic,
473 N.; Würth, I. IEA Wind Task 32: Wind Lidar Identifying and Mitigating Barriers to the Adoption of Wind
474 Lidar. *Remote Sensing* **2018**, *10*, 406. doi:10.3390/rs10030406.
- 475 17. Pauscher, L.; Vasiljevic, N.; Callies, D.; Lea, G.; Mann, J.; Klaas, T.; Hieronimus, J.; Gottschall, J.; Schwesig,
476 A.; Kühn, M.; Courtney, M. An Inter-Comparison Study of Multi- and DBS Lidar Measurements in
477 Complex Terrain. *Remote Sensing* **2016**, *8*, 782. doi:10.3390/rs8090782.
- 478 18. Altstädter, B.; Platis, A.; Wehner, B.; Scholtz, A.; Wildmann, N.; Hermann, M.; Käthner, R.; Baars, H.;
479 Bange, J.; Lampert, A. ALADINA – an unmanned research aircraft for observing vertical and horizontal
480 distributions of ultrafine particles within the atmospheric boundary layer. *Atmospheric Measurement*
481 *Techniques* **2015**, *8*, 1627–1639. doi:10.5194/amt-8-1627-2015.
- 482 19. Platis, A.; Altstädter, B.; Wehner, B.; Wildmann, N.; Lampert, A.; Hermann, M.; Birmili, W.; Bange, J. An
483 Observational Case Study on the Influence of Atmospheric Boundary-Layer Dynamics on New Particle
484 Formation. *Boundary-Layer Meteorology* **2016**, *158*, 67–92. doi:10.1007/s10546-015-0084-y.
- 485 20. Cione, J.J.; Kalina, E.A.; Uhlhorn, E.W.; Farber, A.M.; Damiano, B. Coyote unmanned aircraft
486 system observations in Hurricane Edouard (2014). *Earth and Space Science* **2016**, *3*, 370–380.
487 doi:10.1002/2016EA000187.
- 488 21. Wildmann, N.; Rau, G.A.; Bange, J. Observations of the Early Morning Boundary-Layer Transition with
489 Small Remotely-Piloted Aircraft. *Boundary-Layer Meteorology* **2015**, *157*. doi:10.1007/s10546-015-0059-z.
- 490 22. Balsley, B.B.; Lawrence, D.A.; Woodman, R.F.; Fritts, D.C. Fine-Scale Characteristics of Temperature, Wind,
491 and Turbulence in the Lower Atmosphere (0–1,300 m) Over the South Peruvian Coast. *Boundary-Layer*
492 *Meteorology* **2013**, *147*, 165–178. doi:10.1007/s10546-012-9774-x.
- 493 23. Kral, S.T.; Reuder, J.; Vihma, T.; Suomi, I.; O'Connor, E.; Kouznetsov, R.; Wrenger, B.; Rautenberg, A.;
494 Urbancic, G.; Jonassen, M.O.; Båserud, L.; Maronga, B.; Mayer, S.; Lorenz, T.; Holtslag, A.A.M.; Steeneveld,
495 G.J.; Seidl, A.; Müller, M.; Lindenberg, C.; Langohr, C.; Voss, H.; Bange, J.; Hundhausen, M.; Hilsheimer,
496 P.; Schygulla, M. Innovative Strategies for Observations in the Arctic Atmospheric Boundary Layer
497 (ISOBAR)—The Hailuoto 2017 Campaign. *Atmosphere* **2018**, *9*, 268. doi:10.3390/atmos9070268.
- 498 24. Wildmann, N.; Bernard, S.; Bange, J. Measuring the local wind field at an escarpment using small
499 remotely-piloted aircraft. *Renewable Energy* **2017**, *103*, 613–619. doi:10.1016/j.renene.2016.10.073.
- 500 25. Mauz, M.; Rautenberg, A.; Platis, A.; Cormier, M.; Bange, J. First identification and quantification of
501 detached-tip vortices behind a wind energy converter using fixed-wing unmanned aircraft system. *Wind*
502 *Energy Science* **2019**, *4*, 451–463. doi:10.5194/wes-4-451-2019.
- 503 26. WindForS. WINSent: Developing a wind energy test facility in complex terrain. www.windfors.de.
- 504 27. Weihing, P.; Schulz, C.; Lutz, T.; Krämer, E. Comparison of the Actuator Line Model with Fully Resolved
505 Simulations in Complex Environmental Conditions. *Journal of Physics: Conference Series* **2017**, *854*, 012049.
506 doi:10.1088/1742-6596/854/1/012049.
- 507 28. Letzgus, P.; Lutz, T.; Krämer, E. Detached Eddy Simulations of the local Atmospheric Flow Field within
508 a Forested Wind Energy Test Site located in Complex Terrain. *Journal of Physics: Conference Series* **2018**,
509 *1037*, 072043. doi:10.1088/1742-6596/1037/7/072043.
- 510 29. Rautenberg, A.; Schön, M.; zum Berge, K.; Mauz, M.; Manz, P.; Platis, A.; van Kesteren, B.; Suomi, I.; Kral,
511 S.T.; Bange, J. The Multi-Purpose Airborne Sensor Carrier MASC-3 for Wind and Turbulence Measurements
512 in the Atmospheric Boundary Layer. *Sensors* **2019**, *19*, 2292. doi:10.3390/s19102292.
- 513 30. Hofsäb, M.; Clifton, A.; Cheng, P.W. Reducing the Uncertainty of Lidar Measurements in Complex Terrain
514 Using a Linear Model Approach. *Remote Sensing* **2018**, *10*, 1465. doi:10.3390/rs10091465.
- 515 31. Skamarock, W.C.; Klemp, J.B.; Dudhia, J.; Gill, D.O.; Barker, D.M.; Duda, M.G.; Huang, X.Y.; Wang, W.;
516 Powers, J.G. A Description of the Advanced Research WRF Version 3. p. 125.
- 517 32. Weller, H.G.; Tabor, G.; Jasak, H.; Fureby, C. A tensorial approach to computational continuum mechanics
518 using object-oriented techniques. *Computers in Physics* **1998**, *12*, 620. doi:10.1063/1.168744.
- 519 33. Kroll, N.; Eisfeld, B.; Bleecke, H.M. FLOWer. In *Notes on Numerical Fluid Mechanics*; Vieweg Verlag
520 Braunschweig, 1999; Vol. Volume 71, pp. 58–68.
- 521 34. Knaus, H.; Rautenberg, A.; Bange, J. Model comparison of two different non-hydrostatic formulations
522 for the Navier-Stokes equations simulating wind flow in complex terrain. *Journal of Wind Engineering and*
523 *Industrial Aerodynamics* **2017**, *169*, 290–307. doi:10.1016/j.jweia.2017.07.017.

- 524 35. El Bahlouli, A.; Rautenberg, A.; Schön, M.; zum Berge, K.; Bange, J.; Knaus, H. Comparison of CFD
525 Simulation to UAS Measurements for Wind Flows in Complex Terrain: Application to the WINSSENT Test
526 Site. *Energies* **2019**, *12*, 1992. doi:10.3390/en12101992.
- 527 36. Doms, G.; Baldauf, M. A Description of the Nonhydrostatic Regional COSMO-Model **2018**. p. 167.
- 528 37. Dudhia, J. A Nonhydrostatic Version of the Penn State–NCAR Mesoscale Model: Validation Tests and
529 Simulation of an Atlantic Cyclone and Cold Front. *Monthly Weather Review* **1993**, *121*, 1493–1513. Publisher:
530 American Meteorological Society, doi:10.1175/1520-0493(1993)121<1493:ANVOTP>2.0.CO;2.
- 531 38. Sogachev, A.; Kelly, M.; Leclerc, M.Y. Consistent Two-Equation Closure Modelling for Atmospheric
532 Research: Buoyancy and Vegetation Implementations. *Boundary-Layer Meteorology* **2012**, *145*, 307–327.
533 doi:10.1007/s10546-012-9726-5.
- 534 39. Katul, G.G.; Mahrt, L.; Poggi, D.; Sanz, C. ONE- and TWO-Equation Models for Canopy Turbulence.
535 *Boundary-Layer Meteorology* **2004**, *113*, 81–109. doi:10.1023/B:BOUN.0000037333.48760.e5.
- 536 40. Cionco, R.M. Intensity of turbulence within canopies with simple and complex roughness elements.
537 *Boundary-Layer Meteorology* **1972**, *2*, 453–465. doi:10.1007/BF00821548.
- 538 41. Shaw, R.H.; Den Hartog, G.; Neumann, H.H. Influence of foliar density and thermal stability on profiles
539 of Reynolds stress and turbulence intensity in a deciduous forest. *Boundary-Layer Meteorology* **1988**,
540 *45*, 391–409. doi:10.1007/BF00124010.
- 541 42. Shaw, R.H.; Schumann, U. Large-eddy simulation of turbulent flow above and within a forest.
542 *Boundary-Layer Meteorology* **1992**, *61*, 47–64. doi:10.1007/BF02033994.
- 543 43. Liu, J.; Chen, J.M.; Black, T.A.; Novak, M.D. $E - \epsilon$ modelling of turbulent air flow downwind of a model
544 forest edge. *Boundary-Layer Meteorology* **1996**, *77*, 21–44. doi:10.1007/BF00121857.
- 545 44. Aubrun, S.; Leitl, B. Development of an improved physical modelling of a forest area in a wind tunnel.
546 *Atmospheric Environment* **2004**, *38*, 2797–2801. doi:10.1016/j.atmosenv.2004.02.035.
- 547 45. Sanchez Gomez, M.; Lundquist, J.K. The Effects of Wind Veer During the Morning and Evening Transitions.
548 *Journal of Physics: Conference Series* **2020**, *1452*, 012075. doi:10.1088/1742-6596/1452/1/012075.
- 549 46. DIN EN IEC 61400-1 VDE 0127-1:2019-12 - Standards - VDE Publishing House; VDE VERLAG GMBH, 2019.
- 550 47. Stull, R.B. An Introduction to Boundary Layer Meteorology; Springer Netherlands, 1988; pp. 1–27.
551 doi:10.1007/978-94-009-3027-8_1.
- 552 48. de Boer, G.; Diehl, C.; Jacob, J.; Houston, A.; Smith, S.W.; Chilson, P.; Schmale, D.G.; Intrieri, J.; Pinto, J.;
553 Elston, J.; Brus, D.; Kemppinen, O.; Clark, A.; Lawrence, D.; Bailey, S.C.C.; Sama, M.P.; Frazier, A.; Crick,
554 C.; Natalie, V.; Pillar-Little, E.; Klein, P.; Waugh, S.; Lundquist, J.K.; Barbieri, L.; Kral, S.T.; Jensen, A.A.;
555 Dixon, C.; Borenstein, S.; Hesselius, D.; Human, K.; Hall, P.; Argrow, B.; Thornberry, T.; Wright, R.; Kelly,
556 J.T. Development of Community, Capabilities, and Understanding through Unmanned Aircraft-Based
557 Atmospheric Research: The LAPSE-RATE Campaign. *Bulletin of the American Meteorological Society* **2020**,
558 *101*, E684–E699. doi:10.1175/BAMS-D-19-0050.1.